Diss. ETH No. 24530

Improve industrial cone-beam computed tomography by integrating prior information

A dissertation submitted to attain the degree of
DOCTOR OF SCIENCES of ETH ZURICH
Dr. sc. ETH Zurich

presented by

YU LIU
MSc ETH

BORN ON 04.05.1988
CITIZEN OF PEOPLE'S REPUBLIC OF CHINA

accepted on the recommendation of

Prof. Dr. Konrad Wegener, examiner
Prof. Dr. Alex Dommann, co-examiner
Dr. Antonia Neels, co-examiner

2017

Abstract

Cone-beam X-ray transmission computed tomography (CT) is a cross-sectional imaging technique with diverse applications in medical diagnosis, industrial inspection and material research. Industrial CT calculates a 3 dimensional representation of an object from a fast and non-destructive measurement. This has enabled possibilities in product quality control and dimensioning in product design.

However, due to the variations in sizes and materials of industrial samples, the conventional measurement and calculation processes lead to representations with artifacts. The artifacts lower the spatial resolution of the CT measurements and misrepresent the structure of the sample under test.

This dissertation explores the possibilities to improve industrial cone-beam CT by employing arbitrary trajectory and prior information during the data acquisition and calculation processes. The first contribution is the automatic calibration of the CT setup utilizing a new calibration target. The calibration models the CT imaging subsystem as a projective camera and extract the geometry from projection images. This calibration process isolates the reconstruction artifacts from the calibration. The second contribution comes from the com-

bination of arbitrary trajectory and iterative reconstruction. Lower noise and less pronounced artifacts are accomplished by this approach. The third contribution comprises two data fusion models to integrate optical scanning data in CT reconstruction. The novelty of the models lies in the capability to fuse either complete or partial optical data acquired off-site with CT data. The improvement from the data fusion includes reducing the amount artifact and restoring missing features in limited-angle CT scans. Both have been validated by experiments.

Zusammenfassung

Röntgen-Computertomographie (CT) in Kegelstrahlgeometrie ist ein bildgebendes Verfahren mit vielfältigen Anwendungsgebieten in der medizinischen Diagnostik, in der industriellen Inspektion und in der Materialforschung. Die industrielle CT stellt eine schnelle und zerstörungsfreie Messtechnik dar, welche eine drei-dimensionale Darstellung eines Objekts ermöglicht. Dadurch erschliessen sich Möglichkeiten in der Qualitätsprüfung von Produkten sowie der Vermessung von Dimensionen in der Produktgestaltung.

Aufgrund der Schwankungen in den Grössen und Materialien industrieller Proben, führen herkömmliche Messungen und Berechnungen zu Objektdarstellungen mit Artefakten. Diese Artefakte verringern das räumliche Auflösungsvermögen der CT Messungen und führen zu einer falschen Darstellung der Struktur des zu untersuchenden Objekts.

In dieser Dissertation werden Möglichkeiten zur Verbesserung industrieller Kegelstrahl CT untersucht. Die Verbesserungstechniken basieren auf willkürlichen Abtast-Bahnen im Messprozess sowie in der Verwendung von Vorabinformationen in den Berechnungen. Der erste Beitrag ist eine automatische Kalibrierung des CT Aufbaus durch ein neues Kalibrations-Objekt. Die Kalibration

modelliert das bildverarbeitende Teilsystem des CTs in Form einer projizierenden Kamera und extrahiert die Geometrie aus den projizierten Bildern. Die Kalibrierung grenzt die Rekonstruktionsartefakte aus der Kalibrierung ab. Der zweite Beitrag stammt aus der Verbindung der willkürlichen Messbahnen mit einer iterativen Rekonstruktion. Durch diesen Ansatz können niedrigere Störsignale und weniger ausgeprägte Artefakte erreicht werden. Der dritte Beitrag dieser Arbeit umfasst zwei Datenfusions-Modelle zur Integration von optischen Messdaten in die CT Rekonstruktion. Diese Modelle bieten das Potential entweder komplette oder partielle optische Daten, welche extern entstanden sind, mit den CT Daten zu vereinigen. Die Verbesserung durch das Datenfusionsmodell zeigt sich in einer Verringerung der Artefakte, sowie in einer Wiederherstellung von fehlenden Merkmalen in Messungen mit beschränktem Winkelraum. Beide Verbesserungen konnten in Experimenten bestätigt werden.

Contents

Acknowledgments

This dissertation would not have been possible without the help from many people and the close collaboration with my project partners. This project is mainly funded by an SNF grant entitled Improving Limited Angle X-ray computed Tomography by Optical data integration (ILATO) with the grant number: 200021L_141311/2.

Foremost, I graciously thank my supervisor, Prof. Dr. Konrad Wegener, head of the *Institute of Machines Tools and Manufacturing*, for offering continuous guidance and sharing his passion in scientific research. I am also deeply grateful to Dr. Antonia Neels, head of the *Center for X-ray Analytics*, for co-supervising my doctoral study and revising this dissertation. Her deep domain knowledge in X-ray analytics and her rich experience in scientific research have helped and inspired me throughout my study. I would like to express my gratitude to Prof. Dr. Alex Dommann, head of the *Department of Materials Meet Life*, for his close mentoring during my study. His invaluable comments on my research have always been concise and enlightening.

Moreover, I would like to thank Dr. Urs Sennhauser, former head of the *Laboratory of Reliability Science and Technology*, for sharing his scientific

insights into computed tomography. I would like to thank Dr. Philipp Schütz for introducing me to the basic concepts of computed tomography and for his continuous support over the last four years.

Furthermore, many thanks go to my colleagues at Empa. Alexander Flisch has been extremely supportive in my research and during the writing of this dissertation. His excellent interpersonal skills have made him an extraordinary manager and helped to create a supportive and productive office atmosphere. I would like to thank Jürgen Hofmann for his help in CT reconstruction. I would like to thank Dr. Rolf Kaufmann, Dr. Rolf Brönnimann, Dr. Mathieu Plamondon, Dr. Erwin Hack, Stefan Hartmann and Carina Stritt for their technical contributions.

Special thanks go to my project partners from Heidelberg University. Dr. Andreas Bayer has been working closely with me since the beginning of the project. Many ideas have originated from our bi-weekly on-line meetings. I would like to thank Dr. Susanne Krömker and Dr. Hubert Mara for sharing their knowledge in topology.

I would also like to thank my family and friends for their supports and care throughout this project. They have been the source of my motivation and the sometimes much-needed lovely distractions.

Glossary

$3D$	3 dimensional.
$\underline{\underline{A}}$	The system matrix of a CT system.
$\underline{\underline{A}}^{+}$	The psudo-inverse of the system matrix.
ADC	Analogue to digital converter.
$ADMM$	Alternating direction method of multipliers.
$ALARA$	As Low As Reasonably Achievable.
ART	Algebraic reconstruction technique.
A_Z	Atomic weight.
b_i	Basis function.
c_a	The first coefficient of a plane equation.
c_b	The second coefficient of a plane equation.
c_c	The third coefficient of a plane equation.
CAD	Computer aided design.
CLC	Circle-line-circle.
CMM	Coordinate measurement machine.
CNC	Computer numerical control.
CT	Computed tomography.

$\underline{d}$	A vector containing the coordinates of a point in a reference frame. Vectors are underlined in this dissertation.
DLT	Direct linear transformation.
DOF	Degrees of freedom.
$Empa$	Swiss Federal Laboratories for Materials Science and Technology.
FDK	Feldkamp-Davis-Kress algorithm.
FFT	Fast Fourier transformation.
f_s	Sampling frequency.
h	Planck constant.
$\underline{I}$	Intensity images from all angles.
I_0	Beam intensity before attenuation.
$\underline{I}_0$	Flat field image.
ICP	Iterative closest point.
IEC	International electrotechnical commission.
$\underline{\underline{I}}_n$	A n by n identity matrix.
I_{tr}	Transmitted intensity.
$\underline{I}^{\theta}$	Intensity distribution image from angle θ.
I_i^{θ}	Intensity at pixel i from angle θ.
$LINAC$	Linear accelerator.
l_{pitch}	Pitch size of neighbor elements.
l_{sdd}	Source to detector distance.
l_{sid}	Source to isocenter distance.
$\underline{\underline{M}}_{ext}$	The extrinsic matrix of one camera system.
$\underline{\underline{M}}_{int}$	The intrinsic matrix of one camera system.

MC	Marching cube.
$\underline{\underline{M}}_{T1}$	Offset transformation applied to the detector.
$\underline{\underline{M}}_{T2}$	Scaling transformation matrix.
$\underline{\underline{M}}_{T3}$	Offset transformation applied to the source.
$\underline{\underline{M}}_{T4}$	In-plane rotation matrix.
$\underline{\underline{M}}_{T5}$	Out-of-plane rotation matrix.
MTF	Modulation transfer function.
$MVEE$	Minimal volume enclosing ellipsoid.
$\underline{n}_A$	The normal vector perpendicular to the infinitesimal area.
$\underline{n}_d$	A normal vector pointing from a point.
$\underline{n}_s$	The ray direction.
N_v	Number of voxels in the reconstructed volume.
$\underline{n}_x$	The normal vector of the x axis.
$\underline{n}_y$	The normal vector of the y axis.
$\underline{n}_z$	The normal vector of the z axis.
$\underline{P}$	An arbitrary point in the world coordinate system.
$\underline{p}$	Integral of attenuation coefficients for all pixels.
$\mathcal{P}$	Forward projector symbol.
$\mathcal{P}^*$	Backward projector symbol.
$\underline{P}_{tr}$	Coordinate after transformation.
$\underline{P}_{tr,\theta}$	The coordinate of a point after rotation.
$\mathcal{R}$	Radon transform.
$\underline{\underline{R}}_{wc}$	Rotation matrix in the world coordinate system.
$RanCEAF$	Random convex-edge affine features.

$rect$	Rectangular function.
RF	Radio frequency.
$\underline{S}$	The location vector of the source in the world coordinate system.
$\mathcal{S}(R^n)$	Schwartz space on R^n.
$SART$	Simultaneous algebraic reconstruction technique.
S_p	The active area of a detector element.
$SSIM$	Structural similarity index.
$SSIM_s$	The structural component of a structural similarity index.
SVD	Singular Value Decomposition.
$\underline{\underline{T}}_g$	General transformation matrix.
$\underline{\underline{T}}_r$	Rotation matrix. Rotate around the system rotation axis.
$\underline{T}_{wc}$	Translation vector in the world coordinate system.
$\underline{u}$	The unit vector in the detector coordinate system.
u_b	Uncertainty of the systematic deviation.
u_{cal}	Calibration uncertainty.
u_{off}	Horizontal offset of the detector.
u_p	Uncertainty from repeated measurements.
u_w	Uncertainty from manufacturing.
$\underline{v}$	The unit vector in the detector coordinate system.

v_{off}	Vertical offset of the detector.
$w.r.t.$	With respect to.
x_{soff}	Horizontal offset of the source.
y_{soff}	Vertical offset of the source.
Z	Atomic number.
θ_{in}	In-plane rotation angle.
θ_{out}	Out-of-plane rotation angle.
ν	Frequency of a photon.
$\underline{\mu}$	A set of linear attenuation coefficients.
μ_a	Absorption coefficient.
μ_s	Scatter coefficient.
μ_u	Total attenuation coefficient.

Chapter 1

Introduction

Back in 1890s, X-rays were discovered and systematically studied by Wilhelm Conrad Röntgen for the first time. The capability of studying the internals of an object raised the interest of the research community resulting in a large number of research projects on this topic. The technology in generating and detecting X-rays also evolved fast to meet the demand from both research and industry. Computed tomography is one of the most important applications enabled by the discovery of X-rays and the development of X-ray technology. By acquiring radiographies around an object, a representation of the internals of an object can be calculated.

Due to the non-invasive character of computed tomography (CT), it quickly became a popular medical imaging method. The research in medical CT focuses on identifying small contrast in attenuation images within a short acquisition time while keeping a low radiation dose, following the infamous As Low As Reasonably Achievable ($ALARA$) principle. In recent years, more advanced

signal processing methods have been utilized in the medical CT reconstruction resulting in higher detectability with lower dose.

Outside the medical imaging field, CT is also used as a 3D imaging tool in industry and research. Unlike medical CT, the designs of industrial CT systems are optimized to achieve either larger field of view to accommodate larger samples or optimized to achieve higher spatial resolution to resolve micro structures. One appealing feature of CT as an imaging tool is that the measurement is non-destructive, which drives down the analytical costs and enables repeated measurements of one sample after it undergoes other tests.

However, for a given industrial CT system, a generic scanning procedure and genetic processing algorithm may result in artifacts. In a generic scanning procedure, the sample rotates in the CT setup while a detector records the radiographies of the sample. A schematic of a CT setup in the reference frame of the sample is illustrated in fig. 1.1(a). The process to compute a $3D$ representation of the sample from these radiographies is referred as CT reconstruction. The result of the reconstruction from the radiographies acquired using a generic scanning procedure contains *cone-beam artifacts*, which leads to reduced spatial resolution as illustrated in fig. 1.1(b). When measuring large samples, a complete rotation is not possible due to the possible collisions between the sample and the CT system. With only a subset of the complete radiographies, the result suffers from severe limited-angle artifacts as illustrated in fig. 1.1(b).

In this dissertation, the possibility to incorporate 3D optical surface scan (fig. 1.1(c)) in a CT measurement process is explored. The first idea is to replace the generic scanning procedure with an adaptive procedure according to the visible size of the sample. The second idea is to fuse the optical data with

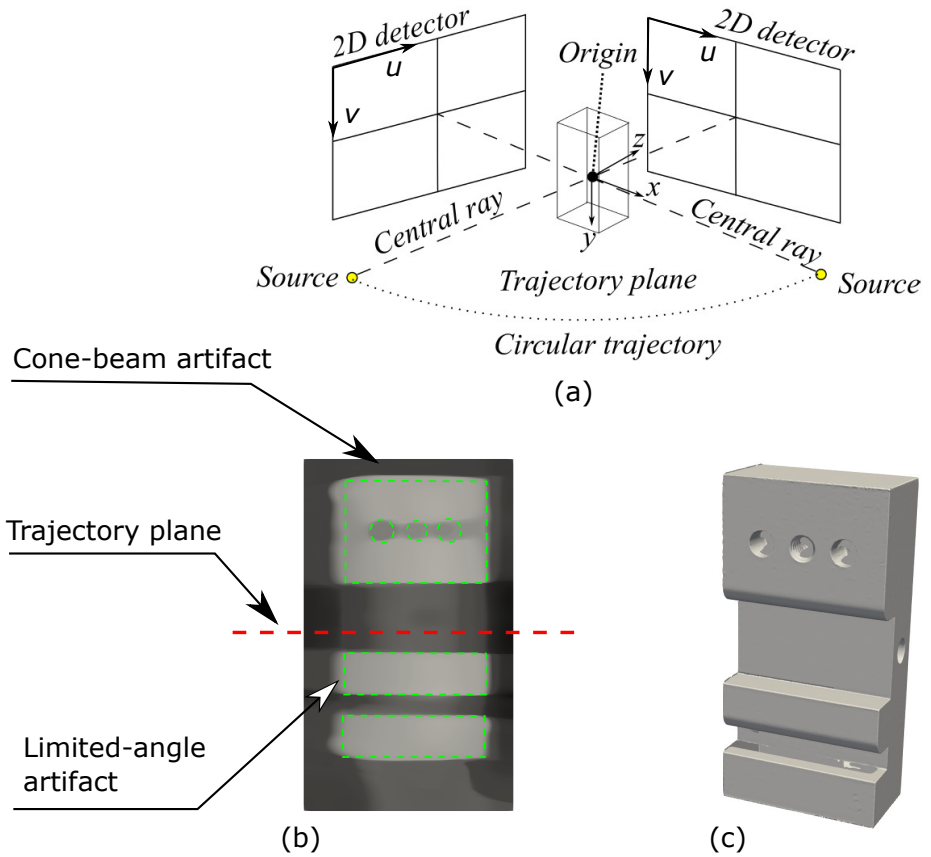

Figure 1.1: The schematic of a simple CT system illustrated in the reference frame of the object is shown in (a). (b) illustrates the cone-beam artifact and the limited-angle artifact utilizing a cross section taken from a limit-angle CT scan result of a sample. The green dashed lines marks the edges in the ground truth image. The discrepancy between edges from the gray value image and the ground truth are the results of the artifacts. The same sample is scanned with a 3D optical scanner and the resulting mesh is rendered and displayed in (c).

the limited-angle CT data in the reconstruction. Therefore, the objective of this dissertation is to utilize the optical data as prior information and to develop a numerical framework to enable the data fusion of volumetric and surface 3D models to mitigate CT artifacts.

Chapter 2 gives an overview of the measurement techniques utilized in this dissertation, i.e. X-ray tomography, optical surface scan, tactile measurement. The physical processes in measurement techniques are elucidated to explain the fundamental differences and connections among the techniques. For CT, the introduction discusses the production of X-ray photons, the interaction between X-ray photons and matter, the detection of X-ray photons and the geometry of a CT system. The definitions of 2 dimensional and 3 dimensional images and their discrete representation will be given in this section to assist further discussion. For optical surface scans, the structured light scanning method is introduced. The working principle and the resulting surface representation will be illustrated. Lastly in this chapter, tactile measurement employed by tactile coordinate measurement machines is introduced. The advantages over the other techniques and its limitations are reviewed here.

Chapter 3 discusses the introduction to tomography reconstruction algorithms. The introduction will start from 2D Radon transformation and direct inversion algorithm using simplified geometry which helps to understand the basic concepts in the reconstruction. It continues to the widely used analytical 3D reconstruction algorithm and the flexible iterative reconstruction algorithms.

Chapter 4 presents the state-of-the-art in incorporating prior information in a CT investigation. This chapter starts with an overview of the prior information that has been employed in other research projects and the advantages from the

integration of the prior information. Some of the techniques and theories used in this dissertation are reviewed in this chapter. At the end of this chapter, the goal of the research is elucidated with respect to the state-of-the-art.

Chapter 5 starts with the analysis of the calibration of the CT system. A calibration target is assembled and an algorithm is developed to automatically extract the correct geometry. The calibrated geometry is then used in a correction algorithm to achieve a reconstruction free from geometry misalignment. At the end of this chapter, a non-circular trajectory is applied to the scan if the geometry of the sample is known *a priori* and a reconstruction scheme to reconstruct the image from arbitrary trajectory is implemented.

Chapter 6 details the algorithm employed to align the optical data and CT volume as well as two models developed to fuse optical data and CT data. The first data fusion model assumes that the complete optical data is available and the result is demonstrated in a simulation study. To enable the integration of partial optical data, a second data fusion model is developed where the assumption of complete optical data is no longer needed. The model is analyzed in a simulation study and validated by experiments.

Chapter 2

Overview of acquisition systems

Three acquisition systems are used in this dissertation to acquire different physical signals from the object under investigation. The X-ray CT system acquires the attenuation coefficients of the object by means of measuring the transmission of X-ray photons. The surface information of an object is acquired by a 3D optical scanner. The optical scanning method used in this dissertation is based on projecting structured light onto the surface of the object. Other than the two non-contact methods, a mechanical tactile system is also used to locate the surface of the object. In this chapter, a review of the acquisition systems is presented with a focus on the difference in the physical meanings of the signals, the advantages and the disadvantages of the systems.

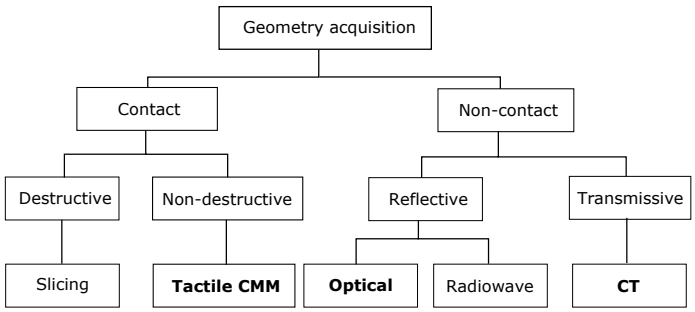

Figure 2.1: Classification of geometry acquisition systems. In this dissertation, optical surface scan and CT scan as non-contact testing methods are used. The data acquired from both systems will be fused to improve the representation of the geometry of the sample under investigation. The tactile CMM results are used during system calibration and used as a ground truth measurement during the evaluation of the fusion result.

2.1 X-ray CT acquisition system

A typical industrial X-ray CT system has three main components, *i.e.* the X-ray source, the sample stage and the detector . One way to represent an industrial X-ray CT system is to decompose such a system into a stationary subsystem and a moving subsystem. Contrary to the medical CT system, the stationary system in an industrial CT is the imaging system, which is composed of the X-ray source and the X-ray detector, and the moving system is the sample manipulation system, which moves the sample *w.r.t.* the imaging system.

The imaging subsystem measures the transmission image of any object placed in the field of view. The perspective of the projection is a function of the geometric parameters of the imaging subsystem. The manipulation system moves the object in the imaging subsystem to change the perspective of the projections. The manipulation is dictated by the trajectory settings which

typically involve translations and rotations.

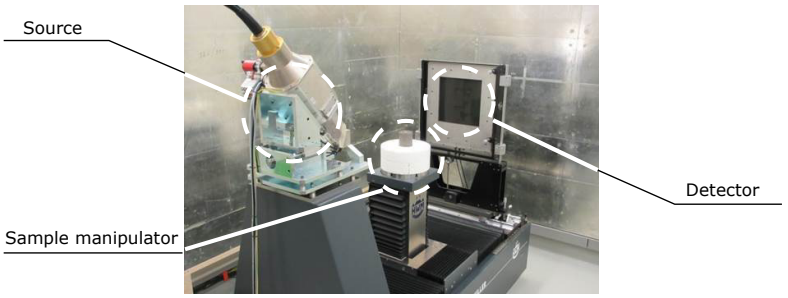

Figure 2.2: A photo of a typical industrial CT system. There are three main components, *i.e.* the X-ray source, the X-ray detector and the sample manipulator. During a CT scan, the source is stationary with respect to (*w.r.t.*) the detector. Therefore, the source and detector are treated as the imaging subsystem in this thesis. Although, the sample manipulator moves the sample to change the projection perspective during a scan, in this thesis, the discussion adopt the reference system of the sample and assume the imaging system is moving according a *trajectory*.

2.1.1 X-ray sources

In industry and research, there are three commonly used X-ray sources. The X-ray generation mechanisms for them are briefly reviewed below.

- Synchrotron radiation

  At a synchrotron facility, the electrons are accelerated close to the speed of light. The electrons are guided into either a bending magnet or an undulator, where the electrons are forced to change their trajectory which results in emitting electromagnetic radiation as elucidated by Stampanoni *et. al.* [66].

- X-ray tube

An X-ray tube is a vacuum tube with a filament emitting electrons on one end. After the electrons leave the filament, they are accelerated by a static electric field towards the other end of the vacuum tube, where the electrons hit a target. X-ray photons are generated during the bombardment process. The photons generated from this process can be classified into two types. When fast moving electrons are decelerated by the nuclei of the target material, X-ray photons are generated. The radiation generated from this process is referred as bremsstrahlung as explained by Cervantes *et. al.* [18]. During the process, some electrons from the inner shell of the atoms assembling the target material are ejected. When an outer shell electron falls to the inner shell, the energy difference is emitted as a photon. The radiation from the process is called characteristic radiation as it carries certain characteristics of the target material.

- Linear accelerator

  The Linear accelerator ($LINAC$) has a lot in common with the X-ray tube regarding the X-ray production mechanism. High speed electrons bombard the target material to generate X-ray photons. The main difference lies in the acceleration process. In a LINAC, the electrons are accelerated by the traveling wave or standing wave in the waveguide generated by RF power as explained by Huang *et. al.*[38].

2.1.2 Beam geometry

A *ray* in the context of this dissertation is defined as a portion of a line starting from the point $\underline{d}$ where the X-ray photon is emitted and pointing to the direction of travel $\underline{n}_d$. A cluster of rays form a beam. A *parallel beam* is a

cluster of parallel rays which point to the same direction, while a *divergent beam* is a cluster of rays which originate from the same starting point. A particular divergent beam often used in industrial CT is a *cone beam* which is a divergent beam collimated to form a cone shape beam in space.

2.1.3 Beam quality

The quality of the X-ray source has a direct impact on the result of the imaging system. The following aspects are considered as important factors contributing to beam quality.

- Beam intensity and flux

  The *flux* and *intensity* of an X-ray beam in parallel and cone beam geometry can be defined as vector fields. For a point $\underline{d}$ on a surface, as illustrated in fig. 2.3, the intensity can be defined with the help of a small disk centered at $\underline{d}$ with an area A and a normal vector $\underline{n}_A$. The $\underline{n}_A$ is chosen to allow the maximum number of photons traveling through A in a given time. The intensity as shown in eq. (2.1) is measured in s^{-1} and the flux can be derived from the intensity and is measured in $s^{-1}m^{-2}$.

$$\underline{I}(A, \underline{d}) = \underline{n}_d \frac{dN}{dt}(A, \underline{n}_A, \underline{d}) \tag{2.1}$$

$$\underline{j}(\underline{d}) = \frac{\partial \underline{I}}{\partial A}(\underline{d}) \tag{2.2}$$

- Focal spot size

  A cone beam has a single point emitting X-rays. In practice, the X-rays

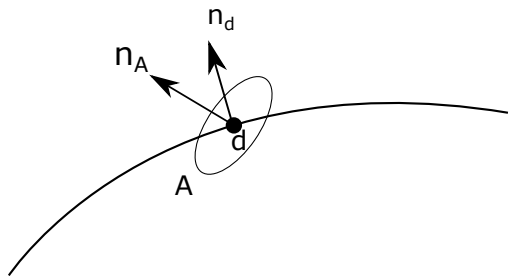

Figure 2.3: Illustration of the axillary surface A used in the definition of flux. d is a point on a surface, with $\underline{n}_d$ being the normal vector at this point. $\underline{n}_A$ is the normal vector of a disk A. $\underline{n}_d$ is selected to maximize the number of particles traveling through A.

are generated in the area where the electrons are focused. The area is defined as the focal spot of the X-ray source.

- Energy spectrum

  The generation of the Bremsstrahlung is a random process. The resulting X-ray photons have different energies. The spectrum of the generated X-ray photons can be filtered by metal films to produce a narrower spectrum at a cost of reduced beam intensity.

- Beam uniformity

  One specific problem for an X-ray tube is that the intensity of X-rays leaving the target depends on their angle to the target surface. This leads to an uneven distribution of flux within the beam. This is often referred to as the heal effect [16]. Assuming a sphere centered at the X-ray source, the amplitude of the flux on the surface of the sphere varies.

Tradeoffs

During the interaction of the electron and the target material, most of the kinetic energy of the fast moving electron is converted to heat. Due to the limited rate of heat transfer, the total amount of heat that can be dissipated in a unit area is limited. Therefore, with increased power, the focal spot size will increase. At the same time, higher flux of electrons will cause the electrons to repel each other due to their electric field. This poses a challenge to the focusing of the electrons, which may lead to the further expansion of the focal spot size. Filtering the X-ray photons will narrow the bandwidth of the spectrum, but it will further reduce the intensity. By designing the filter geometry [49], the non-uniform beam profile can be mitigated.

2.1.4 X-ray photon mass interaction

X-ray imaging relies on the interaction between X-ray photons and matter. When the X-ray photons are traversing through an object, they may be absorbed or scattered by the material. Therefore, the intensity of the beam will decrease after traversing through matter. The attenuation of the beam intensity carries the information of the object under investigation, which leads to the contrast in the resulting X-ray images.

Beer-Lambert Law

For a narrow monochromatic beam, the attenuation can be modeled as:

$$I_{tr} = I_0 e^{-\int_L \mu_u(\underline{x}) d\underline{x}}, \tag{2.3}$$

where

$$\mu_u(\underline{x}) = \mu_s(\underline{x}) + \mu_a(\underline{x}) \tag{2.4}$$

The total attenuation coefficient $\mu_u(\underline{x})$ is a sum of scatter coefficient $\mu_s(\underline{x})$

and absorption coefficient $\mu_a(\underline{x})$, for which an empirical relation is [16]:

$$\mu_a = \frac{k\rho Z^4}{A_Z(h\nu)^3}, \tag{2.5}$$

where k is a constant, Z is the atomic number of the material, A_Z is the atomic weight of the material and $h\nu$ is the photon energy.

2.1.5 X-ray detection

The intensity of the beam is measured with an X-ray detector. The X-ray photons are converted into visible light first and the intensity of the visible light is measured with photo diodes. The electrons generated at the photo diodes with the help of the photoelectric effects are collected at the detector. The voltage is then digitized by an analog to digital converter and used as a measure of the X-ray beam intensity.

2.1.6 CT acquisition

A CT acquisition system is composed of an X-ray source, an X-ray detector and a sample manipulator. The relative positions of the source and detector define the acquisition geometry and the location and orientation of the object is defined by the scanning trajectory. In this chapter, all the notations used to describe the geometry and the trajectory are introduced. Circular trajectory with parallel beam and arbitrary trajectory with cone beam will be described in detail.

The geometry defines the transformation of any point in the world coordinate system to a point in the detector coordinate system. To construct the transformation matrix, a set of geometric parameters is defined. For parallel

geometry, the parameters are defined in fig. 2.4.

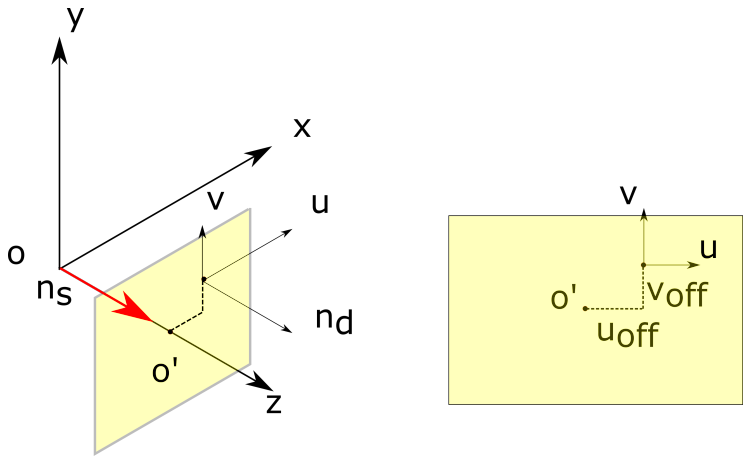

Figure 2.4: Parameters of a parallel beam geometry. n_s is the direction of rays in the parallel beam. n_d is the normal vector of the detector. o' is the projection of the origin of the world coordinate system. (u_{off}, v_{off}) defines the offset from the geometry center of the detector to o'.

The ray direction $\underline{n}_s$ is defined with respect to the world coordinate system. The normal vector of the detector plane is $\underline{n}_d$.

In the geometry with parallel beam (fig. 2.4), the ray direction in the beam is $\underline{n}_s$. The projection of the origin of the world coordinate xyz is $\underline{o}'$. Two orthogonal unit vectors, $\underline{u}$ and $\underline{v}$, form the basis of the in-plane coordinate system. Therefore, $\underline{n}_d = \underline{u} \times \underline{v}$. $\underline{u}$ and $\underline{v}$ indicate the orientation of the detector elements. The orientation is characterized by the in-plane rotation angle, θ_{in}, and out-of-plane, θ_{out}, rotation angle. The in-plane angle is defined *w.r.t.* the x axis and the out-of-plane angle is defined *w.r.t.* the z axis following the right hand rule. The origin of the detector coordinate system is defined by the offset along $\underline{u}$ and $\underline{v}$ from o'. The offset is defined as (u_{off}, v_{off}).

In an ideal case, the in-plane angle and out-of-plane angle are zero and o' is placed at the geometric center of the detector, i.e. $\underline{u} = \underline{n}_x$, $\underline{v} = \underline{n}_y$ and $\underline{n}_d = \underline{n}_z$.

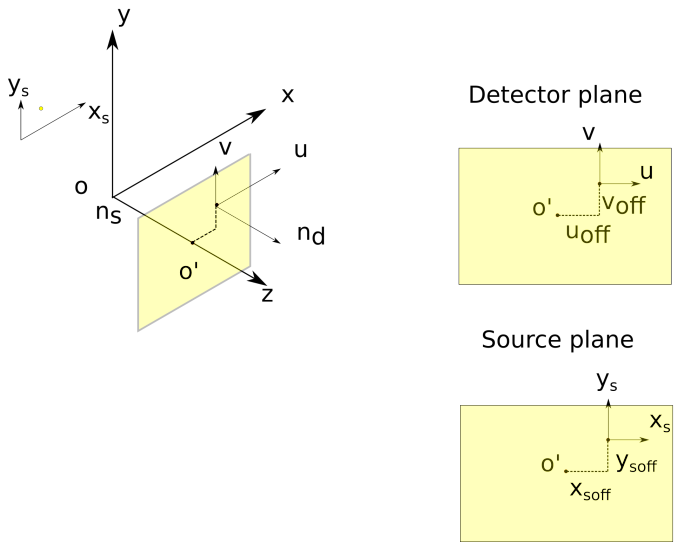

Figure 2.5: Parameters of a cone-beam geometry. n_s in the cone-beam setting is defined as the direction of the principle ray of the cone beam, *i.e.* the ray perpendicular to the detector, while the out-of-plane rotation and the source offset are zero. (x_{soff}, y_{soff}) are the offset of the source in the source plane, *i.e.* plane perpendicular to n_s, *w.r.t* the origin of the source plane.

The cone-beam geometry parameters are defined in fig. 2.5. In a cone-beam geometry, the relative position of the source $\underline{S}$ and the detector is defined. To demonstrate the geometry, the source and the detector are placed in the world coordinate system, such that the projection of $\underline{S}$ overlaps with the origin of the detector coordinate system $\underline{o}'$ while the in-plane and out-of-plane angles are set to zero. The plane containing $\underline{S}$ and being parallel to the detector plane are defined as the source plane. The distance between $\underline{o}'$ and the source plane is the

source detector distance (l_{sdd}) and the distance between $\underline{o}$ and the source plane is the source isocenter distance (l_{sid}). The *sid* and the *sdd* are marked in a simplified schematic as illustrated in fig. 2.6. The position of the source within the source plane can be characterized by the source offset (x_{soff} , y_{soff}).

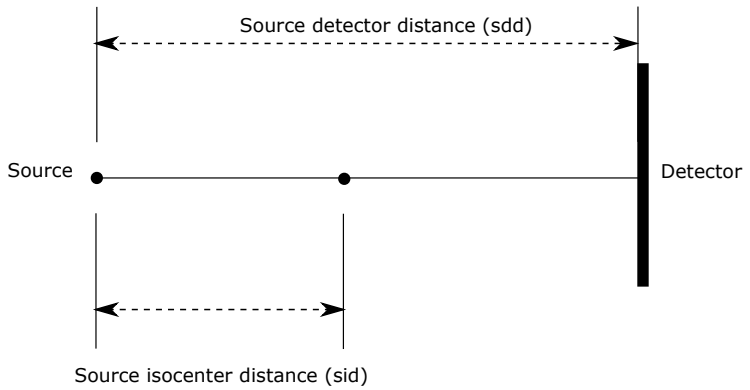

Figure 2.6: A simplified geometry of a CT setup from a side view.

The objective of defining the geometry is to mathematically map any point in the world coordinate system to the detector coordinate system. With the above definition, for any point $\underline{P}$, using the above parameters, its projection in the plane coordinate system can be calculated.

The coordinates are represented in homogeneous coordinates, similarly to what Szeliski *et. al.*[67] employed, to calculate the coordinate $\underline{P}_{tr}$ after the projection.

$$\underline{P}_{tr} = \begin{pmatrix} P_u \\ P_v \\ 1 \end{pmatrix} = \underline{\underline{T}}_g \cdot \begin{pmatrix} P_x \\ P_y \\ P_z \\ 1 \end{pmatrix} = \underline{\underline{T}}_g \cdot \underline{P} \tag{2.6}$$

where

$$\underline{\underline{T}}_g = \overbrace{\begin{pmatrix} 1 & 0 & x_{off} - u_{off} \\ 0 & 1 & y_{off} - v_{off} \\ 0 & 0 & 1 \end{pmatrix}}^{\underline{\underline{M}}_{T1}} \overbrace{\begin{pmatrix} -l_{ssd} & 0 & 0 & 0 \\ 0 & -l_{ssd} & 0 & 0 \\ 0 & 0 & 1 & -l_{sid} \end{pmatrix}}^{\underline{\underline{M}}_{T2}} \overbrace{\begin{pmatrix} 1 & 0 & 0 & -x_{off} \\ 0 & 1 & 0 & -y_{off} \\ 0 & 0 & 1 & 0 \\ 0 & 0 & 0 & 1 \end{pmatrix}}^{\underline{\underline{M}}_{T3}}$$
$$\times \underbrace{\begin{pmatrix} \cos(-\theta_{in}) & -\sin(-\theta_{in}) & 0 & 0 \\ \sin(-\theta_{in}) & \cos(-\theta_{in}) & 0 & 0 \\ 0 & 0 & 1 & 0 \\ 0 & 0 & 0 & 1 \end{pmatrix}}_{\underline{\underline{M}}_{T4}} \underbrace{\begin{pmatrix} 1 & 0 & 0 & 0 \\ 0 & \cos(-\theta_{out}) & -\sin(-\theta_{out}) & 0 \\ 0 & \sin(-\theta_{out}) & \cos(-\theta_{out}) & 0 \\ 0 & 0 & 0 & 1 \end{pmatrix}}_{\underline{\underline{M}}_{T5}} \tag{2.7}$$

Specifically, in $\underline{\underline{T}}_g$, the $\underline{\underline{M}}_{T5}$ applies the out-of-plane rotation; the $\underline{\underline{M}}_{T4}$ applies the in-plane rotation; the $\underline{\underline{M}}_{T3}$ applies the source offset; the $\underline{\underline{M}}_{T2}$ applies

the scaling; the $\underline{\underline{M}}_{T1}$ applies the relative offset of the detector.

The *trajectory* in the context of this dissertation is the trajectory of the X-ray source *w.r.t.* the object during the acquisition. The same definition is used in the OpenRTK toolkit [59] which adopted the geometry definition from the international standard IEC 61217. Most CT scanners can perform a circular trajectory, where the scanning system with a fixed geometry rotates around one fixed rotation axis. If the rotation axis is defined as a line parallel to $(0, 1, 0)^T$ and going through the origin of the world coordinate, the transformed coordinate $\underline{P}_{tr,\theta}$ at any scanning angle θ can be calculated by multiplying the rotation matrix $\underline{\underline{T}}_r$:

$$\underline{P}_{tr,\theta} = \underline{\underline{T}}_g \cdot \underline{\underline{T}}_r \cdot \underline{P} = \underline{\underline{T}}_g \cdot \begin{pmatrix} \cos(-\theta) & 0 & \sin(-\theta) & 0 \\ 0 & 1 & 0 & 0 \\ -\sin(-\theta) & 0 & \cos(-\theta) & 0 \\ 0 & 0 & 0 & 1 \end{pmatrix} \cdot \underline{P} \tag{2.8}$$

The transformation matrix from the geometry and trajectory has 9 degrees of freedom implying the coordinate of the source point, the coordinate of the origin of the detector plane and the orientation of the detector coordinate system. The complete transformation matrix is capable of describing any arbitrary scanning geometry and trajectory.

A few trajectories that are used in this dissertation are used to demonstrate the definition of the geometry.

Ideal geometry and circular trajectory: An ideal geometry in the context of this dissertation implies the source and detector offsets as well as the in-plane and out-of-plane angles are zero. A circular trajectory under such ideal geometry can be represented as:

$$\underline{\underline{T}} = \underline{\underline{I}}_3 \cdot \begin{pmatrix} -l_{ssd} & 0 & 0 & 0 \\ 0 & -l_{ssd} & 0 & 0 \\ 0 & 0 & 1 & -l_{sid} \end{pmatrix} \cdot \underline{\underline{I}}_4 \cdot \begin{pmatrix} \cos(-\theta) & 0 & \sin(-\theta) & 0 \\ 0 & 1 & 0 & 0 \\ -\sin(-\theta) & 0 & \cos(-\theta) & 0 \\ 0 & 0 & 0 & 1 \end{pmatrix}, \quad (2.9)$$

where $\underline{\underline{I}}_n$ denotes an identity matrix of size $n \times n$.

Ideal geometry with spiral trajectory With an ideal alignment in the imaging subsystem and the perfect alignment of the rotation axis, a spiral trajectory needs an extra parameter to describe the spacing after one full evolution, $r_s[rad^{-1}]$.

$$\begin{aligned} \underline{\underline{T}} = \underline{\underline{I}}_3 \cdot \begin{pmatrix} -l_{ssd} & 0 & 0 & 0 \\ 0 & -l_{ssd} & 0 & 0 \\ 0 & 0 & 1 & -l_{sid} \end{pmatrix} \cdot \begin{pmatrix} 1 & 0 & 0 & 0 \\ 0 & 1 & 0 & \theta \times r_s \\ 0 & 0 & 1 & 0 \\ 0 & 0 & 0 & 1 \end{pmatrix} \\ \cdot \underline{\underline{I}}_4 \cdot \begin{pmatrix} \cos(-\theta) & 0 & \sin(-\theta) & 0 \\ 0 & 1 & 0 & 0 \\ -\sin(-\theta) & 0 & \cos(-\theta) & 0 \\ 0 & 0 & 0 & 1 \end{pmatrix} \end{aligned} \quad (2.10)$$

2.1.7 Data representation

As the contrast of CT comes from the attenuation coefficient, the result of CT is a spatial distribution of attenuation coefficient in the field of view of the acquisition system. The spatial distribution of attenuation coefficients is denoted as the object function, which is a real valued function defined on

$\mathbb{R}^3$, $f : \mathbb{R}^3 \mapsto \mathbb{R}$. To parametrize the object function, the object function is represented using the finite series expansion [17].

$$f(\underline{x}) = \sum_{i=1}^{N_v} \mu_i b_i(\underline{x}), \tag{2.11}$$

where $b_i(\underline{x})$ is a set of linear independent basis functions and the μ_i are the coefficients. The most common choice of the basis functions is the voxel functions, that is

$$b_i(\underline{x}) = rect(\frac{x_1 - \hat{x_{i1}}}{\Delta x_1})rect(\frac{x_2 - \hat{x_{i2}}}{\Delta x_2})rect(\frac{x_3 - \hat{x_{i3}}}{\Delta x_3}), \tag{2.12}$$

where $(\hat{x_{i1}}, \hat{x_{i2}}, \hat{x_{i3}})$ is the coordinate of the center of the ith voxel and the $(\Delta x_1, \Delta x_2, \Delta x_3)$ denotes the voxel size in each direction.

The beam intensity function on the detector plane is a real valued function defined on the detector plane, $I^\theta : \mathbb{R}^2 \mapsto \mathbb{R}$. The intensity function is sampled by the detector, therefore it is automatically represented using a set of pixel basis functions. The parameters in this basis is measured according to the spatial sampling process and the quantification process:

- Spatial sampling

  The sampling of the beam intensity is achieved with a flat-panel detector where the detector elements are aligned in a rectangular grid. The pitch of the detector elements sets the spatial frequency of the sampling process. Assuming the pitch sizes in both directions are the same, the sampling frequency of the intensity distribution in each direction of the flat panel detector is $f_s = 1/l_{pitch}[mm^{-1}]$. Due to the finite size of the detector elements, the sampled value is an average over the span of the active area

of the detector element. Assuming $\underline{p}_i$ is the coordinate of the center of the ith element in the detector coordinate system, the intensity sampled by the ith detector element at a projection angle θ is represented as I_i^θ

$$I_i^\theta = \iint_{S_p} I^\theta(\underline{p}_i)\, dS, \tag{2.13}$$

where S_p is the active area of the ith detector element.

- Quantification

  After the sampling process, I_i^θ is mapped to a finite set of discrete values limited to the output of the analogue to digital converter (ADC). To fully utilize the dynamic range of the ADC, the ratio between the maximum intensity and minimum intensity should be close to the maximum discrete value and the noise floor should be kept low by choosing proper exposure settings. During a CT scan, the exposure settings of the acquisition system are constant in order to keep the acquisition consistent across all projections. Therefore, the exposure setting has to be calculated based on the smallest attenuation from all projections, resulting in under-utilization of the dynamic range in certain projections. This will reduce the intensity resolution in industrial CT when the sample is planar.

The resulting discrete representation of the intensity distribution image from angle θ can be denoted as $\underline{I}^\theta$. I_i^θ denotes a specific pixel value in the discrete representation. If the projection angles are arranged in some order, the complete stack of images can be denoted as $\underline{I}$ and the value of a single pixel value as I_i. Similarly, the beam intensity without any attenuation is denoted as $\underline{I}_0$ which is also referred as the flat field image.

Without considering the polychromatic nature of the X-rays and the scattering of the X-ray photons in the sample, the Beer Lambert law eq. (2.3) is applied to calculate the integral of the attenuation coefficient $\underline{p}$ along the path of the beam from the sampled beam intensity,

$$\underline{p} = \{-\ln(\frac{I_i}{I_{0i}}) \mid I_i \in \underline{I}, I_{0i} \in \underline{I}_0\} \tag{2.14}$$

Accordingly, the CT reconstruction problem can be represented as the estimation of the coefficients $\underline{\mu}$ under a set of basis functions $b_i(\underline{x})$ from the measurement of the intensity images $\underline{I}$.

2.1.8 Limitations

CT measurements come with their limitations. The quality of the CT result is limited in spatial resolution and intensity resolution. The CT result is also prone to artifacts.

- Spatial resolution of a single projection

  The performance of a typical imaging system can be estimated by the modulation transfer function (MTF) [48]. The main factors contributing to the limited response of the MTF include the focal spot size, the pixel size of the detector and the pixel cross talk. In addition, the scattering of X-ray photons also lowers the spatial resolution of the imaging system.

- Intensity resolution of a single projection

  The discrete representation of the intensity image has limited resolution in the magnitude of the intensity [12]. With insufficient intensity resolution, the acquisition will not be able to pick up low contrast features and may

contain banding artifacts. With a limited dynamic range of the ADC, it is very challenging to preserve all details for samples with large variation in thickness.

- Limitation from the geometry

  The accuracy of CT relies on the accuracy of the acquisition system. The reconstruction process takes the geometric parameters as input parameters. Any error in the geometric parameters will be propagated to the reconstruction results. Typical artifacts arising from inaccurate geometry include wrong voxel size and blurred image boundary.

2.2 Optical scanning

Optical surface acquisition is another non-contact acquisition method. The signal from the acquisition is the optical reflectivity property of the sample. The optical surface scanning methods can be classified into active and passive scanning methods [10] depending on whether controlled structured light was used. An optical acquisition system with a light source projecting a structured pattern to the sample is an active acquisition system. Such scanners are called structured light scanners and scanners without using structured light are stereoscopic scanners.

2.2.1 Principles

Both stereoscopic scanners and structured light scanners utilize triangulation to sense the position of a point in the camera coordinate system.

Stereoscopic scanner

In a simplified model, a stereoscopic scanner is composed of two camera systems as illustrated in fig. 2.7. To measure the position of a point in the world coordinate system where O_w is the origin, each camera captures an image of the point and record its coordinate in the pixel array. The relation between the coordinates of the point in the world coordinate system and its image can be expressed with the help of the projection matrix in homogeneous coordinates as:

$$\begin{pmatrix} u \\ v \\ 1 \end{pmatrix} = \underline{\underline{M}}_{int} \cdot \underline{\underline{M}}_{ext} \cdot \begin{pmatrix} U \\ V \\ W \\ 1 \end{pmatrix} \tag{2.15}$$

and

$$\begin{pmatrix} u' \\ v' \\ 1 \end{pmatrix} = \underline{\underline{M'}}_{int} \cdot \underline{\underline{M'}}_{ext} \cdot \begin{pmatrix} U \\ V \\ W \\ 1 \end{pmatrix} \tag{2.16}$$

where $\underline{\underline{M}}_{ext}$ and $\underline{\underline{M'}}_{int}$ are the intrisic matrices [35] of the cameras and $\underline{\underline{M}}_{ext}$ and $\underline{\underline{M'}}_{ext}$ are the extrinsic matrices defining the spacial relations of the object and the cameras.

If the following conditions are met, the coordinate in the world coordinate system can be calculated.

- Calibrated cameras

  The cameras are calibrated such that the intrinsic projection matrices are

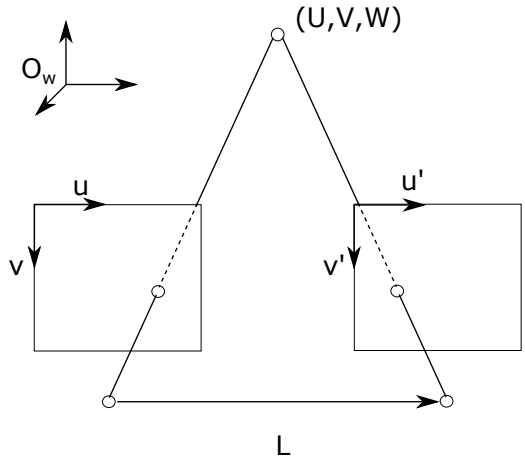

Figure 2.7: Illustration of a simple stereo camera system. In this simplified model, there are two pin hole cameras and their relative position is known. The point with an unknown position represented by $(U, V, W)^T$ can be extracted if both cameras are calibrated and are able to capture the point.

known. In addition, the relative position of the two cameras is known such that a linear relation between the extrinsic matrices of the two cameras is known.

- Point correspondence

  The point of interest on the object is correctly identified on the image from the camera.

Structured light scanner

In a structured light scanner, one of the camera systems in the stereoscopic scanner is replaced with a projector. The acquisition principle remains the same. The difference lies in the point correspondence process. Instead of matching images acquired from both cameras, the only camera acquires the known pattern projected from the projector to accomplish the correspondence task.

2.2.2 Limitations

The limitations of the optical surface scan comes from the calibration of the system and the point correspondence as well as from the stitching of results from different scans. The calibration of the system must be performed each time after the configuration of the setup is modified. During the measurement, the change in system temperature will lead to a drift of the calibration due to the thermal expansion. The point correspondence is achieved by identifying image features in stereoscopic scanners and by identifying the pattern reflected by the surface of the sample in structured light scanners.

The structured light scanner is used as the main instrument in this dissertation for optical surface acquisition. To construct the correspondence,

the pattern projected on the surface of the sample has to be visible to the camera in the system. This leads to the following limitations:

- Material property of the sample

  If the material of the sample is transparent to the light used by the scanner (laser or visible light) or if the material is translucent, the projected pattern will not form any image with enough contrast for the camera to detect.

- The texture of the surface of the sample.

  Glossy surface will lead to spectacular reflections on the surfaces which will saturate the sensor of the camera. As a result, such surfaces will not be detected.

- The color of the surface.

  If the projected structured light is absorbed by the surface material, no contrast will be detected by the camera. This also results in the surface not being detected.

- The topology of the surface.

  Narrow cavities and deep trenches on the surface will block either the projection or the view of the camera preventing the correspondence.

Accuracy limits

Quantitative analysis of optical surface scanning setups is very challenging because of the many instrument parameters [29]. Qualitatively, the accuracy of the measurement mainly comes from two aspects, i.e. the error within a single acquisition and the error from stitching the acquisitions from different directions.

The spatial resolution of the projection pattern and the spatial resolution of the camera are the main limiting factors of high spatial accuracy.

2.2.3 Data representation

Every point that has been successfully detected and triangulated will be recorded. All detected points from the scans will result in a point cloud. To preserve the surface information, the connectivity among the points is added. The resulting data structure is the mesh representation of the surface. In this dissertation, a mesh from the surface scan is refered as $\mathcal{M}_{opt}$.

2.3 CMM scanning

The tactile coordinate measurement is the standard in the manufacturing industry. The procedure has been standardized to produce traceable results. This task can be performed by a dedicated coordinate measurement machine (CMM) or a CNC machine with modification.

2.3.1 Principle

A tactile CMM relies on the tactile feedback from probing the sample surface. The position and the geometry of the probe are recorded when a feedback is registered. The measurement results are used to fit the parameters of primitives. The following primitives are measured:

- Surface

  A surface is represented as a point on the surface and a normal vector.

- Cylinder

  A cylinder is parameterized as a point and a vector pointing along the axis of the cylinder and the length of the radius.

- sphere

  A sphere is parameterized as a point in the center and a radius from the center to the surface.

2.3.2 Limitations

The limitations of CMM measurements are the following:

- Speed

  The measurement is a serial process and involves mechanical movement for each point. This leads to a very low throughput. Within any reasonable measurement time, only a limited number of surface points can be measured.

- Material of the sample

  Due to the limited sensitivity of the force sensor, the tactile CMM cannot measure samples with soft surfaces.

- Free form surface

  With the basic configuration used in this dissertation, only the measurements of primitives are possible. The continuous measurement of a free form surface is challenging and it needs a sampling plan estimated from the original design.

- Resolution

  The CMM offers high accuracy measurement, but it lacks the ability to resolve fine structures. As the probe has a finite size, the smallest feature is limited by the size of the probe.

- Reach

  The limited reach of the probe poses an upper limit to the largest depth of a measurement. Deep and narrow trenches cannot be measured with CMM.

2.3.3 Data representation

In this dissertation, the parameters from the measurements of the primitives are listed in tables.

Chapter 3

Tomographic reconstruction

Tomographic reconstruction is the process to calculate the representation of the object from the measurements. Using the notation from section 2.1, the reconstruction of CT is the process of estimating the coefficients $\underline{\mu}$ under a set of basis functions $b_i(\underline{x})$ from the measurement of the intensity images $\underline{I}$. This chapter starts with the Radon transformation which represents a function using integrals on hyperplanes. As the attenuation of the beam intensity by the sample is directly related to the integral of the linear attenuation coefficient along the path of the ray, the radon representation builds a connection between the attenuation coefficient and the measured beam intensity. Similar to the Radon transformation in some way, the cone beam transformation is more important to industrial CT applications because parallel beams are almost exclusively used at synchrotron facilities.

3.1 Radon transform

The attenuation of the beam intensity is a function of the integral of the attenuation coefficients along the path of the beam. To assist the analysis of the reconstruction problem, the Radon transform [42] is defined. Assuming $f \in \mathcal{S}(R^n)$, where $\mathcal{S}(R^n)$ is a Schwartz space on $\mathcal{S}(R^n)$, for a vector $\underline{\theta}$ on the unit sphere S^{n-1} and a signed scalar value $s \in R$, the Radon transform $\mathcal{R}$ can be defined:

Definition 3.1 (Radon transformation)**.**

$$\mathcal{R}f(\underline{\theta}, s) := \int_{\underline{x}\cdot\underline{\theta}=s} f(\underline{x})\mathrm{d}\underline{x}, \tag{3.1}$$

where s is the distance between the origin and the hyperplane perpendicular to $\underline{\theta}$. An illustration of the Radon transformation in 2D is shown in fig. 3.1.

An operator along a predefined orientation is defined as:

$$\mathcal{R}_{\underline{\theta}}f(s) := \mathcal{R}f(\underline{\theta}, s). \tag{3.2}$$

The X-ray transform is the integral along a line going through point $\underline{x}$ with direction $\underline{\theta}$

Definition 3.2 (X-ray transform)**.**

$$\mathcal{P}f(\underline{\theta}, \underline{x}) := \int_{-\infty}^{+\infty} f(\underline{x} + t\underline{\theta})\mathrm{d}t. \tag{3.3}$$

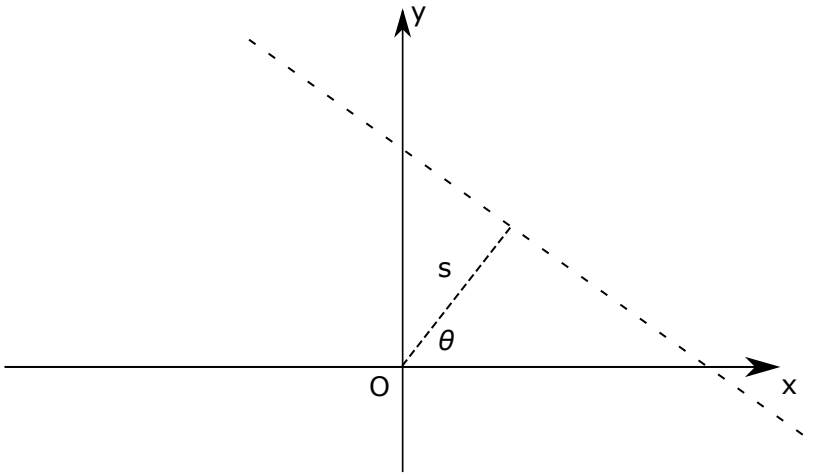

Figure 3.1: An illustration of the Radon transformation in 2D.

The Radon transform can be expressed as an integral of the X-ray transform:

$$\mathcal{R}f(\underline{\omega}, s) = \int\limits_{\underline{x}\in\underline{\theta}^{\perp}, \underline{x}\cdot\underline{\omega}=s} \mathcal{P}f(\underline{\theta}, \underline{x})\mathrm{d}\underline{x}, \tag{3.4}$$

where $\underline{\theta} \in S^{n-1}$ and $\omega \perp \theta$.

Similarly, the X-ray transform from a predefined direction is defined as $\mathcal{P}_{\underline{\theta}}$. $\mathcal{P}$ is referred as a *forward projection* operator and its dual operator, $\mathcal{P}^*$, is referred as a *backward projection*.

Definition 3.3 (X-ray back projection transform)**.**

$$\underline{\mathcal{P}}^* f(x) = \int\limits_{S^{n-1}} f(\underline{\theta}, E_\theta x)\mathrm{d}\theta, \tag{3.5}$$

where $E_\theta x$ is the orthogonal projection on $\underline{\theta}^{\perp}$.

The Divergent beam transform is an integral along a half line starting from a point:

Definition 3.4 (Divergent beam transform)**.**

$$\mathcal{D}f(\underline{a},\underline{\theta}) := \int_0^{+\infty} f(\underline{a}+t\underline{\theta})\mathrm{d}t, \tag{3.6}$$

where $\underline{a}$ is the starting point of the half line.

The position parameter can be absorbed into the operator to simplify the notation as:

$$\mathcal{D}_a f(\underline{\theta}) := \int_0^{+\infty} f(\underline{a}+t\underline{\theta})\mathrm{d}t, \tag{3.7}$$

The cone beam back projection for any given ray starting point is defined as:

Definition 3.5 (Divergent beam back projection)**.**

$$\mathcal{D}^*_{\underline{a}} f(\underline{x}) := f(\underline{a},\underline{\theta}_{ax}), \tag{3.8}$$

where $\underline{\theta}_{ax} \in S^{n-1}$ is parallel to the vector pointing from $\underline{a}$ to $\underline{x}$.

3.2 Fourier slice theorem

One important addition to the Radon transform is the Fourier slice theorem.

Definition 3.6 (Fourier slice theorem)**.** For $f \in \mathcal{S}(R^n)$,

$$\mathscr{F}(\mathcal{R}_\theta f(\sigma)) = (2\pi)^{(n-1)/2}\mathscr{F}(f(\sigma\theta)), \tag{3.9}$$

where $\sigma \in \mathcal{R}$ and $\mathscr{F}$ denotes the Fourier transform of a function.

The Fourier slice theorem bridges the Radon transform of a function and the function itself via Fourier space. Combined with eq. (3.4), the Fourier representation of the function can be calculated from the X-ray transform of the function. This leads to the reconstruction algorithms.

3.3 Fourier based reconstruction

The direct calculation of the inverse Fourier transform from the Fourier transform of the projections is referred as the direct Fourier reconstruction. Since 3D CT scan is the focus of this dissertation, the following discussion will be limited to 3D.

Definition 3.7 (Direct Fourier reconstruction)**.** For $f \in \mathcal{S}(R^3)$,

$$f(\underline{x}) = (2\pi)^{-3/2} \int_{R^3} e^{i\underline{x}\cdot\underline{\xi}}\mathscr{F}(f(\underline{\xi}))\mathrm{d}\underline{\xi}, \tag{3.10}$$

The direct Fourier reconstruction is an analytical solution assuming the Fourier representation to be continuous. However, due to the discrete nature of the sampling process, only a subset of the Fourier coefficients are available and they are arranged in a polar grid. To utilize the fast Fourier transformation (FFT), the corresponding coefficients in a rectangular grid in the Fourier space are interpolated. The error introduced in the interpolation process limits the practical application of this reconstruction method.

The simplicity of the direct Fourier transform lies in the fact that there is a conversion between the Radon data and Parallel projection data as shown in eq. (3.4). However, such a conversion does not exist between Radon data and divergent beam projection data. In industrial CT, a cone beam, which is a divergent beam in 3D, is used instead of parallel beam. Since there is no direct conversion from cone-beam data to Radon data, the reconstruction has to be adapted. Grangeat [34] discovered a method to calculate the derivatives of the Radon transform from the cone beam transform. Based on the derivative of the Radon transform, the function can be reconstructed from the cone beam transform.

The Grangeat method requires complete Radon data, which means all the coefficients in the Radon transform need to be available. The data completeness in the Radon space implies the cone beam transform to be measured at any possible source position, using the notation from eq. (3.6), $\underline{a}/\|\underline{a}\| \in S^2$. However, in practice, the data completeness cannot be guaranteed. The source positions in real world scans form a curve in space, which only covers a subset of S^2. The curve is referred as the *source trajectory*. If the source trajectory is in a plane and forms a complete circle, such a trajectory is referred as a *circular trajectory*. A scan following a circular trajectory is easy to perform in real world applications, although the incomplete data acquired during such a scan prevent an exact reconstruction of the function.

3.4 Filtered backprojection reconstruction

The data acquired with a setup consisting of a cone beam source and a flat panel detector cannot cover the entire Radon space if only a circular trajectory

is performed during the acquisition. All measurable Radon coefficients with a circular trajectory are distributed in a torus shaped region if the detector is assumed to be infinitely large. The region outside the torus is referred as the shadow space [16]. If the necessary Radon coefficients to reconstruct the function at a certain location fall in the shadow space, the function at the specific location cannot be exactly reconstructed.

If the trajectory is denoted as $\underline{a}(\lambda)$, with $\lambda \in R^1$ as a parameter, Tuy [68] has concluded that the exact function value at $\underline{x}$ can be exactly reconstructed with the presence of noise only if $\underline{a}(\lambda)$ fulfills the following conditions:

Definition 3.8 (Tuy's conditions)**.** For any $\underline{\theta} \in S^2$, there exists λ, such that

$$(\underline{a}(\lambda) - \underline{x}) \cdot \underline{\theta} = 0, \tag{3.11}$$

$$\underline{a}'(\lambda) \cdot \underline{\theta} \neq 0. \tag{3.12}$$

Tuy's conditions require each plane that goes through $\underline{x}$ intersects the trajectory transversally to exactly reconstruct the value at $\underline{x}$ with stability against noise.The Tuy's conditions are applied to the circular trajectory. Any point that is not in the plane containing the circular trajectory does not meet the Tuy's conditions, i.e. any plane containing $\underline{x}$ that is parallel to the circular trajectory plane at the same time does not intersect the circular trajectory. Therefore, a stable reconstruction of the exact values is not possible anywhere other than in the trajectory plane.

Feldkamp, et. al [30] developed an algorithm to reconstruct an approximation of the function from projection data acquired from a cone beam source and a flat panel detector setup performing a circular trajectory.

Definition 3.9 (FDK reconstruction)**.** Assuming $p_{\theta v}(u, v)$ is the projection from θ on the virtual detector going through the isocenter.

The projection value is weighted geometrically:

$$p_{\theta vw}(u, v) = p_{\theta v}(u, v) \frac{l_{sid}}{\sqrt{l_{sid}^2 + u^2 + v^2}}, \tag{3.13}$$

Apply a high pass filter $g(u)$ along the axis parallel to the trajectory plane:

$$h_\theta(u, v) = p_{\theta vw}(u, v) * g(u), \tag{3.14}$$

Back project to image domain. For any position (x, y, x),

$$f(x, y, z) = \int_0^{+2\pi} \frac{l_{sid}^2}{(l_{sid} - xsin(\theta) + zcos(\theta))^2} h_\theta(u, v) \mathrm{d}\theta \tag{3.15}$$

The exact attenuation coefficients from the trajectory plane can be reconstructed correctly while the attenuation coefficients outside the trajectory plane are prone to *cone beam artifact* as shown in fig. 3.2. The surfaces parallel to the trajectory plane are blurred resulting in a reduced spatial resolution in the direction of the rotation axis. For scans using a small cone angle, the FDK algorithm offers a good reconstruction result.

3.5 Algebraic reconstruction

Other than solving the reconstruction problem by computing the inverse Radon transform of a function, the reconstruction problem from a different perspective can be approached from a different perspective.

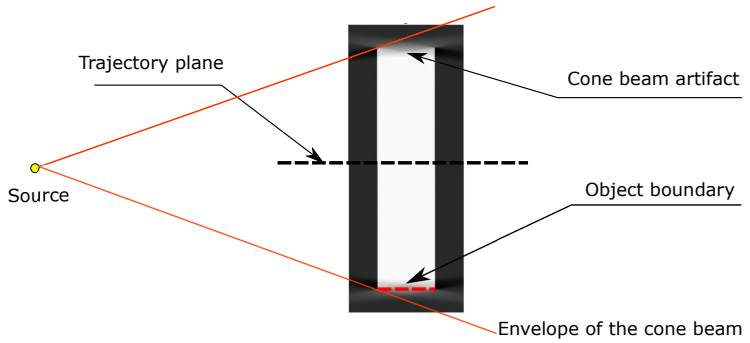

Figure 3.2: The cross section of a reconstructed cuboid perpendicular to the trajectory plane. The blurred boundary is referred as the cone-beam artifact. The trajectory plane is the plane where all source positions lie in. The cause of the cone-beam artifact is insufficient data from the acquisition. A schematic of the source and the envelope of the cone beam are added to the figure to illustrate the angle between the X-ray beam and the boundary.

3.5.1 Direct algebraic reconstruction

Assuming the rectangular grid is used as the representation of the function to be reconstructed, the total attenuation along a narrow beam can be calculated as the following:

$$p_i = \sum_{j=1}^{N} a_{ij}\mu_j, \tag{3.16}$$

where $i = 1, ..., M$ is the index of the projection and $j = 1, ..., N$ is the index of the attenuation coefficients in the representation.

If all the measurements are arranged together,the following compact form can be used:

$$\underline{p} = \underline{\underline{A}} \cdot \underline{\mu}, \tag{3.17}$$

If $\underline{\underline{A}}$ is explicitly known, the above linear system can be solved by calculating

$$\underline{\tilde{\mu}} = \underline{\underline{A}}^{+} \cdot \underline{p}, \tag{3.18}$$

where $\underline{\underline{A}}^{+}$ is the Moore Penrose Pseudo-inverse [28], which can be calculated by SVD [63]. However, a high resolution industrial CT scan will produce a measurement $\underline{p}$ with a size of $M = 1440 \times 4000 \times 4000 = 2.304 \times 10^{10}$. To reconstruct a grid consisting of $N = 4000 \times 4000 \times 4000 = 6.4 \times 10^{10}$ unknowns, $\underline{\underline{A}}$ will have more than 10^{21} elements. Although $\underline{\underline{A}}$ is sparse, the computation of the SVD cannot be finished in a reasonable time. In addition, typically the reconstruction problem is ill-posed [43], i.e. some singular values from the SVD calculations are small. The Pseudo inverse will amplify very small changes in the projections data leading to a very unstable reconstruction.

3.5.2 Iterative reconstruction

To solve the linear system in eq. (3.17), iterative methods are more feasible considering the size of the problems. The algebraic reconstruction technique (ART) employs the Kaczmarz's method [41] solving eq. (3.17) by projecting intermediate iteration results onto the solution set of a single row in $\underline{\underline{A}}$. The sequence of the iterations will converge to a solution to eq. (3.17).

At the beginning of the iteration, the volume to be reconstructed is set to $\underline{0}$. A random narrow beam is then chosen to project the volume to a point in the projection. The difference is then back-projected to the volume. The iteration stops once the stopping criteria are met. The ART algorithm is summarized in Algorithm 1.

In Algorithm 1, the index i is selected randomly from all possible detector

Algorithm 1 Algebraic reconstruction technique

1: **procedure** ART
2: $\underline{\mu}^{(0)} = \underline{0}$,
3: $\underline{p}^{(n)} = \underline{\underline{A}} \cdot \underline{\mu}^{(n)}$
4: $\underline{\mu}^{(n)} = \underline{\mu}^{(n-1)} - \frac{a_i \cdot \underline{f}^{(n-1)} - p_i}{\underline{a_i} \cdot \underline{(a_i)}^T} \underline{(a_i)}^T$
5: **end procedure**

locations. The algebraic reconstruction methods are flexible to the acquisition geometry and are less prone to noise in the projection images. Compared to the FDK algorithm, the algebraic methods can achieve better image quality at a reduced amount of projections. At the same time, the capability to incorporate other constraints and prior information make it an increasingly popular reconstruction method.

Chapter 4

State of the art

The previous chapters have introduced the CT acquisition process and the basic principals of the CT reconstruction algorithms. The FDK algorithm has been used as the standard reconstruction algorithm in many commercial CT systems [55] but it has its intrinsic limitations such as the blurring in the direction of the rotation axis [72] and the restriction on the acquisition of the projections. The ART algorithm is not limited to the acquisition but, within a given measurement, the result from the this algorithm converges to the least square solution [40], which is an approximation of the exact solution. Without any additional information, iterative reconstructions like ART cannot further improve the reconstruction quality. Fortunately, the flexibility to incoorperate prior information is one of the advantages of iterative reconstructions over the conventional FDK algorithm. Most of the research on the topic of incoperating prior information are trying to achieve one or more of the following objectives:

- reduce noise

- mitigate artifacts
- reduce the number of required projections

This chapter presents an overview of the different prior information that has been utilized to improve the CT reconstructions and the implementations of new algorithms incorporating prior data.

4.1 Prior information employed in CT

As CT is a technology to sense the spatial distribution of attenuation coefficients, any knowledge about this distribution prior to the acquisition is considered as prior information. The prior information comes from the understanding of the image properties or an additional measurement of the same object utilizing the same or different measurement modalities.

4.1.1 Image property

The distribution of attenuation coefficients of the object and the projections are represented as functions defined in 3D and 2D space as shown in subsection 2.1.7. When the object function and the projection functions are represented as images, the prior understanding of the image properties can be exploited during the reconstruction process. The statistical properties and the compressibility of the images have been studied in many projects.

Statistics

Poisson noise model. The generation of the X-ray photons and the interaction of the X-ray photons with matter as well as the detection of X-ray photons is a cascaded Poisson process if the electronic noise at the detector

readout is not considered [16]. $\hat{I}_i$ denotes a random variable and I_i denotes a realization of $\hat{I}_i$. $\hat{I}_i$ follows a Poisson distribution with an expectation of $I_{0i}e^{-(\underline{\underline{A}}\cdot\underline{\mu})_a}$, i.e.

$$I_i \sim Poisson(I_{0i}e^{-[\underline{\underline{A}}\cdot\underline{\mu}]_i}), \tag{4.1}$$

where $[.]_i$ denotes the ith element of the vector.

To model the complete process including the readout system, a Gaussian term can be added to the noise model [65, 44] to simulate the noise from the readout circuit.

$$I_i \sim Poisson(I_{0i}e^{-[\underline{\underline{A}}\cdot\underline{\mu}]_a}) + \mathcal{N}(0,\, \sigma^2), \tag{4.2}$$

where the σ is measured experimentally with the radiation turned off.

Gaussian noise model. A more practical and simpler model is to assume a Gaussian noise after applying the Beer-Lambert Law eq. (2.3), i.e.

$$p_i = [\underline{\underline{A}} \cdot \underline{\mu}]_i + n_i, \quad n_i \sim \mathcal{N}(0,\, \sigma_i^2), \tag{4.3}$$

Sparseness and compressibility

Using the notation from subsection 2.1.7, a signal $\underline{f}$ can be represented using a set of basis functions $\underline{b}$ and coefficients $\underline{\mu}$. If there are only $K, K \ll N_v$ non-zero coefficients, $\underline{f}$ is K *sparse* in basis $\underline{b}$.

Most natural images are not sparse. Due to the existence of noise, the representation of natural images is not sparse in almost all basis functions. However, under certain representations, the image are compressible.

The coefficients $\underline{\mu}$ in a certain set of basis functions $\underline{b}$ can be sorted in a

decreasing order:

$$\hat{\mu}_1, ..., \hat{\mu}_K, ..., \hat{\mu}_{N_v} \tag{4.4}$$

If the sorted coefficients follow a power law decay and there are only a few large coefficients, the image is *compressible*. A more rigorous definition can be found in [19].

The compressibility of images is often used as prior information in iterative reconstruction algorithms to regularize the solutions.

Self similarity

The self similarity at different positions within one image was employed in the non-local means denoising filter [15, 14]. The non-local means filter is a patch-based filter. The non-local mean filter can be expressed as:

$$\mu_{j,NLM} = \frac{\sum\limits_{k \in S_j} w_{jk}(\underline{\mu})\mu_k}{\sum\limits_{k \in S_j} w_{jk}(\underline{\mu})}, \tag{4.5}$$

where $w_{jk}(\underline{\mu})$ is the similarity function and S_j is the search region.

4.1.2 Prior images

Measurements taken from the object under investigation prior to the CT measurements are used as prior information. As the measurement may be taken from a different modality, the use of prior images is often a multisensor data fusion problem. The objective of data fusion tasks is to achieve a synergistic effect.

Depending on the attributes measured by the modalities, the prior images can be categorized into two groups.

- CT scans

  Previous CT scans of the same object at the same or different resolution can be used to improve the CT reconstruction as a prior image . In the case of a CT scan, the value in the image carries the same physical meaning and often in the same representation. This allows a direct integration of the prior data.

- Other sensors

  Optical surface scan, ultrasonic measurement and magnetic resonance imaging results are also used as prior information. However, the fusion of signals from different physical domains is not straightforward.

4.1.3 *CAD* file

The design file as a guideline for the manufacturing of a part can be used as prior data.

4.2 Incorporating prior information

With the given prior information listed above, there are many possible methods to incorporate them to improve the CT result. The approaches are classified into two categories depending on the moment the prior information enters the CT process. The CT process is composed of three major steps, i.e. the acquisition, the reconstruction and the analysis of the result as illustrated in fig. 4.1. The methods in the first category apply the prior information before the data acquisition process to improve the quality of the raw data. The methods in the second category focus on fusing the prior data into the final reconstruction.

Although the two categories will be discussed separately, the methods on both categories are often applied together as the acquisition and the reconstruction are coupled.

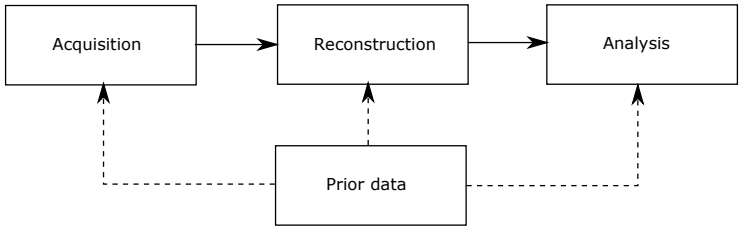

Figure 4.1: CT process diagram. A typical CT investigation includes three procedures: acquisition, reconstruction and analysis. In this thesis, prior data is utilized in all three procedures with a focus on the integration of prior data during the reconstruction.

4.2.1 Acquisition with prior information

Most commercial systems acquire images along a circular source trajectory at positions uniformly distributed along the circle. Based on the prior knowledge of the object, the conventional acquisition protocol is no longer the optimal. By studying the prior information of the object, non-standard acquisition protocols allow better reconstructions or reconstruction in comparable quality from a reduced number of projections.

In-plane trajectories

The circular trajectory is an in-plane trajectory as all sampling points lie in the same plane. Such design is easy for mechanical implementation and experiment planning. For 2D CT scans, an in-plane trajectory is sufficient to achieve accurate and stable reconstruction result according to eq. (3.11). In-plane trajectories other than a standard circular trajectory have been proposed

to enable different applications or to improve the reconstruction results [6, 25].

The first variant is a circular trajectory with selected projection angles. The data acquired from all angles contains a large amount of redundant information [56] and the information from different angles contributes to the result differently. By selecting only a subset of all possible angles, the object can be reconstructed at similar quality allowing cheaper and faster measurements. In [6], a similar trajectory has been applied to the simulation to achieve favorable results compared to a standard trajectory with the same number of projections while assuming the binary nature of the image is known *a priori*. Using the notation from eq. (2.9) in subsection 2.1.6, the transformation matrices for each projection can be represented as:

$$\{\underline{\underline{T}}(\theta), \underline{\underline{T}}(\theta + \Delta\theta), ..., \underline{\underline{T}}(\theta + (n-1)\Delta\theta)\}, \tag{4.6}$$

where n is the number of projection and $\Delta\theta$ is the angular increment used during the scan.

The circular trajectory with selected projection angles can be presented as:

$$\{\underline{\underline{T}}(\hat{\theta}_1), \underline{\underline{T}}(\hat{\theta}_2), ..., \underline{\underline{T}}(\hat{\theta}_n)\}, \tag{4.7}$$

where the sequence $\underline{\hat{\theta}}$ is the outcome of the selecting algorithm.

Another in-plane trajectory was proposed [25] where the spatial support of the object is used to allow dynamic zooming during the acquisition. In this approach, the convex hull of the object was extracted from the spatial support. The source to object distance is adjusted dynamically such that the project of the object fully utilizes the detector area. The authors claim a more accurate

result and increased resolution. The trajectory can be presented as:

$$\{\underline{\underline{T}}(\theta, l_{sid0}),\ \underline{\underline{T}}(\theta + \Delta\theta, l_{sid1}), ...,\ \underline{\underline{T}}(\theta + (n-1)\Delta\theta, l_{sid(n-1)})\}, \tag{4.8}$$

If the shape of the object is known *a priori* by optical surface scanning and a circular trajectory is impossible due to possible collisions between the object and the scanner, a limited-angle scanning trajectory needs to be applied. A limited-angle trajectory [31, 64, 21] covers less angles than a short-scan [57] needs. The range of the scanning angle during a *short-scan* is the sum of π and the cone opening angle. An in-plane limited-angle trajectory can be represented as:

$$\{\underline{\underline{T}}(\theta),\ \underline{\underline{T}}(\theta + \Delta\theta),\ ...,\ \underline{\underline{T}}(\theta + (k-1)\Delta\theta)\},\ k\Delta\theta < \theta_{parker}. \tag{4.9}$$

where θ_{parker} is the angular range in a short scan.

Arbitrary trajectory As proved in [68], an in-plane trajectory is insufficient to stably reconstruct the whole object accurately and the geometry of the equipment and the sample may prohibit certain scanning position. Arbitrary trajectories with measurement positions that are not in the same plane can be applied to samples if the boundary of the object is known prior to the measurement. The realization of arbitrary trajectory is often limited by the manipulation system of a CT setup. Such a manipulation system is demonstrated by Banjak *et. al.* [5], where the source and detector are mounted on robotic arm to enable CT scans of stationary objects. However, with limited reach of the robotic arms, an arc-line-arc scanning trajectory [71, 37] is used.

Using the notation of this dissertation, the trajectory can be represented as:

$$\{\underline{\underline{T}}(\theta,0,0),\ ...,\ \underline{\underline{T}}(\theta+(k-1)\Delta\theta,0,0),$$
$$\underline{\underline{T}}(\theta+(k-1)\Delta\theta,\Delta l,\Delta l),\ ...,\ \underline{\underline{T}}(\theta+(k-1)\Delta\theta,y_{off},v_{off}),$$
$$\underline{\underline{T}}(\theta+(k-2)\Delta\theta,y_{off},v_{off}),\ ...,\ \underline{\underline{T}}(\theta,y_{off},v_{off})\}, \quad (4.10)$$

where Δl is the step size in vertical translation.

Since the reconstruction of the full object is not needed for certain measurement, the design of the trajectory has been tailored towards the reconstruction of a region of interest or towards certain imaging tasks. Gang *et. al.* [32] has demonstrated a design rule for task-based trajectories by allowing one additional degree of freedom when scanning along a circular trajectory. Schrapp *et. al.* [62] has taken this idea and applied it to industrial CT systems.

Using the notation of this dissertation, a task-based trajectory can be symbolically represented as:

$$\{\underline{\underline{T}}\} = \arg\max_{\{\underline{\underline{T}}\}} f(W_t, M, \{\underline{\underline{T}}\}), \quad (4.11)$$

where W_t is the task function describing the imaging task, M is the quality metric used to evaluate the performance of the reconstruct at the imaging task and $\{\underline{\underline{T}}\}$ is the sequence of acquisition with its parameters.

4.2.2 Reconstruction with prior information

In this section, the focus is on the iterative reconstruction algorithms which are capable of incorporating prior information. Although certain variation of analytical algorithms allows the integration of prior data, the choices of

prior data is limited [75] and they are not as flexible because a complete reimplementation is needed if the parameter of the reconstruction problem changes. I will focus on the specific reconstruction algorithms employing prior information.

Reconstruction with arbitrary trajectory

As shown in Algorithm 1, the computation procedure does not put any constraints on the geometry. The system matrix A contains all the geometry information needed to describe the spatial relation between the object and the imaging system. Since all projection values on one projection image correspond to one single projection configuration it is more efficient using all pixels from one projection to update the object instead of using a single projection value. The simultaneous algebraic reconstruction technique ($SART$) [3] can be employed for this purpose.

Algorithm 2 Simultaneous algebraic reconstruction technique

1: **procedure** SART
2: $\underline{\mu}^{(0)} = \underline{0}$,
3: $\underline{p}^{(n)} = \underline{\underline{A}} \cdot \underline{\mu}^{(n)}$
4: $\underline{\mu}^{(n)} = \underline{\mu}^{(n-1)} - \frac{\sum_{p_i \in \underline{p_i}} \frac{\underline{a_i} \cdot \underline{\mu}^{(n-1)} - p_i}{\underline{a_i}} (\underline{a_i})^T}{\sum_{p_i \in \underline{p_i}} \underline{a_i}}$
5: **end procedure**

In Algorithm 2, $\underline{p_i}$ is a set containing all pixel values from one single projection.

Reconstruction using the noise model as prior information

In statistical reconstruction methods, the attenuation coefficients are modeled as a random variable. Although it is an abuse of symbols, $\underline{\mu}$ is used to represent the random variable and a realization of it is represented as $\underline{\hat{\mu}}$ to avoid

using a different symbol to represent the object. Similarly, the projection values are modeled as a vector of random variable $\underline{p}$ and a realization of it $\hat{\underline{p}}$. The $\underline{\mu}$ with the highest likelihood to produce the given measurement $\hat{\underline{p}}$ is the solution to the reconstruction problem. As the object is unknown and the measurement is corrupted by noise, the expectation maximization method is used to solve the problem. In the first step, the expectation of $\underline{p}$ is derived according to the system model and noise model as function of $\underline{\mu}$. In the maximization step, the most likely $\underline{\mu}$ is calculated, often in an iterative way.

According to the measurement model and the noise model eq. (4.1), the discrete likelihood of measuring $\hat{\underline{I}}$ given $\hat{\underline{\mu}}$ can be calculated as eq. (4.12) if the entries in $\underline{I}$ are considered statistical independent.

$$P_{\underline{I}}(\hat{\underline{I}} \mid \hat{\underline{\mu}}) = \prod_{i=1}^{M} \frac{(I_{0i} e^{-[\underline{\underline{A}} \cdot \hat{\underline{\mu}}]_i})^{\hat{I}_i}}{\hat{I}_i!} e^{-I_{0i} e^{-[\underline{\underline{A}} \cdot \hat{\underline{\mu}}]_i}} \tag{4.12}$$

After taking the logarithmic operation on both sides:

$$\ln P_{\underline{I}}(\hat{\underline{I}} \mid \hat{\underline{\mu}}) = \sum_{i=1}^{M} (\hat{I}_i \ln I_{0i} e^{-[\underline{\underline{A}} \cdot \hat{\underline{\mu}}]_i} - \ln \hat{I}_i! - I_{0i} e^{-[\underline{\underline{A}} \cdot \hat{\underline{\mu}}]_i}) \tag{4.13}$$

To maximize the likelihood, the derivative is calculated and set to 0:

$$\frac{\partial \ln P_{\underline{I}}(\hat{\underline{I}} \mid \hat{\underline{\mu}})}{\partial \hat{\mu}_j} = \sum_{i=1}^{M} (-\hat{I}_i a_{ij} + I_{0i} e^{-[\underline{\underline{A}} \cdot \hat{\underline{\mu}}]_i} a_{ij}) \tag{4.14}$$

Multiply $\hat{\mu}_j$ on both sides, the update scheme using a fixed-point iteration is show as the following:

$$\hat{\mu}_j^{(k+1)} = \hat{\mu}_j^{(k)} \frac{\sum_{i=1}^{M} I_{0i} e^{-[\underline{\underline{A}} \cdot \hat{\underline{\mu}}]_i} a_{ij}}{\sum_{i=1}^{M} \hat{I}_i a_{ij}} \tag{4.15}$$

where k and $k+1$ are iteration numbers.

Reconstruction with regularization

To reconstruct $\underline{\mu}$ from eq. (3.17) with a noise model as in eq. (4.3), another approach is to solve an unconstrained optimization problem of the form:

$$J(\underline{\mu}^*) = \|\underline{p} - \underline{\underline{A}} \cdot \underline{\mu}^*\|_2^2, \tag{4.16}$$

where $\|.\|_2$ denotes the $l2$ norm.

As the reconstruction problem is ill-posed, *i.e.* the solution is sensitive to input noise, the system is underdetermined [39] or the system is inconsistent [54], the solution to the above system is unstable [27]. The measurement process has a low-pass nature due to the limited frequency response from the acquisition system. As a result, the reconstruction contains high-pass filters which can easily amplify noise leading to a noisy or unstable reconstruction. Therefore, a regularization term derived from prior information is often added to the cost function $J(\underline{\mu})$.

$$J(\underline{\mu}) = \|\underline{p} - \underline{\underline{A}} \cdot \underline{\mu}\|_2^2 + \lambda R(\underline{\mu}), \tag{4.17}$$

where the $\|\underline{p} - \underline{\underline{A}} \cdot \underline{\mu}\|_2^2$ is referred as the *data fidelity* and $R(\underline{\mu})$ is the regularization term. λ controls the balance between the data fidelity and regularization.

Reconstruct with prior images

There have been many attempts to reconstruct with prior images. The noncooperation of previous CT data during reconstruction has been proved an effective method to reconstruction using only limited amount of new data. The prior image constrained compressive sensing [20] method has successfully utilized the prior image in the cost function and solved the problem in a

compressive sensing framework.

$$\min_{\underline{\mu}}(\alpha\|\Psi_1(\underline{\mu}-\underline{\mu}_a)\|_1+(1-\alpha)\|\Psi_2(\underline{\mu}_a)\|_1),\ s.t.\ \underline{\underline{A}}\cdot\underline{\mu}=\underline{p} \tag{4.18}$$

The $\underline{\mu}_a$ in eq. (4.18) is the prior image. The Ψ is some sparsifying operator and $\alpha \in (0,1)$ is used to control the contribution of the prior image. Because there is no algorithm to find the l_0 solution in a polynomial time, the l_1 norm is used as a heuristic to reach a solution close to the l_0 solution.

The reconstruction with prior images acuqired from other sensors, such as optical data, requires a different model since the data represents different physical meanings. Current research in fusing optical data with CT data assumes the optical representation and CT representation are pre-aligned and the optical representation is complete and contains no artifacts. In [61], the optical data is replaced by the CAD data and the method is applied on a limited-angle scan to reduce artifacts and to improve contrast. In [46], synthetic data is used to restrict the spatial support of the image, which is similar to a pre-aligned, defect-free optical scanning result.

4.3 Research gap

This chapter shows a list of prior information that has the potential to improve the CT results as well as the approaches to integrate them into the CT work flow. Most of the research focus on using the image properties and more accurate physical models as prior information to improve the reconstruction after the acquisition is done. Impressive results have been achieved to reduce the artifacts and improve image quality without increasing the amount of measurements. The

attempts to use prior images acquired from other sensors have hinted a promising research direction where the information gain from other sensors can be fused to the CT reconstruction to gain a synergy effect. Optical surface scanning has its unique advantage in achieving high resolution 3D representation with a large field of view at low costs. However, the potential of utilizing optical surface data in CT is not fully explored.

The optical surface scanning data can be used in the acquisition planning. A complete CT investigation comprises the acquisition, the reconstruction and the analysis. To achieve the best result, improvements should be applied to the whole work flow. During the acquisition process, the scanning trajectory can be planned if the surface geometry of the object is known. Instead of a standard circular trajectory, an arbitrary trajectory fulfilling Tuy's conditions eq. (3.11) can be applied to eliminate certain artifacts. In this dissertation, the optical surface scanning data is used as *a priori* in both acquisition and reconstruction to combine the improvements.

The practical implementation needs to align the optical data and CT data. In literature, most of the demonstrations are from synthetic data where the spatial relation between the surface data and CT data is known prior to the reconstruction. However, to allow the maximum flexibility, the acquisition of the optical result and CT result are done separately and measured in different coordinate systems. Before the alignment, each system should be calibrated such that both datasets are scaled equally. In this dissertation, the calibration is discussed and a new method is applied to assist the alignment of optical data and CT data.

The data fusion needs to tolerate the defects from the optical scanning. Due to the limitations of the optical acquisition system (subsection 2.2.2), the result

from an optical acquisition contains defects, such as gaps and holes. With such defects, most current data fusion model will fail. Therefore, in this dissertation, a new data fusion model is developed to fuse partial optical data with CT data.

The following chapters attempt to close the research gap by employing new calibration procedures, new alignment procedures and new data fusion models. Chapter 5 starts with the calibration of the CT imaging system and the acquisition procedure. The second part covers the discussion of the alignment of the CT and optical data. Chapter 6 presents two data fusion models capable of mitigating artifacts and can be practically implemented. The validations are done with simulation and experiments.

Chapter 5

CT system calibration and data acquisition

This chapter discusses the characterization of a CT system, including the imaging subsystem and the manipulation subsystem (fig. 2.2), as well as the possibility to use prior information during the acquisition process of CT. The characterization will be restricted to the geometry of the setup. A calibration target is assembled and a characterization procedure which isolates the calculation of geometry from artifacts of the CT reconstruction is developed. At the end of this chapter, the possibility to use a calibrated system to perform scans with arbitrary trajectories (defined in subsection 2.1.6) that fulfill the Tuy's conditions eq. (3.11) is discussed.

The imaging system is composed of an X-ray source and an X-ray detector, which acquires projection images of the object under investigation. The performance of the imaging system is a function of the quality of the beam,

the material attributes of the object under investigation and the characteristic of the detector. In an ideal imaging system, the transfer function at each stage of the imaging system is lossless, which results in a perfect projection image of the object under investigation. A perfect projection image is calculated based on an ideal projective imaging system with a point source. To model the projection process more accurately, a cascaded modeling of the whole imaging process has been published by Tward *et. al.*[69]. As explained in the cascaded model, the result of a real-world imaging system has limited spatial resolution, leading to soft edges in the image. In this chapter, the discussion focuses on the geometric aspects of the imaging system. The geometric relation between the source and detector is calibrated with the help of a customized calibration target to accurately project points in 3D space to the detector plane.

The manipulation system executes the designed trajectory along the direction in which the projection images are taken. The manipulation system often operates independently from the imaging system. Therefore, the spatial relation between the manipulation system and the imaging system needs to be known prior to the reconstruction. Manual calibration is time consuming and is prone to operator errors. One approach to correct the misalignment between the imaging system and the manipulation system is to iteratively correct the geometry guided by a cost function defined on the reconstructed image as demonstrated by Muders *et. al*[51]. As a reconstruction step is involved in the process, this approach is time-consuming. Another issue with this approach is that the reconstruction volume is different from the ground truth up to a scaling factor which is not acceptable for metrological applications. In this chapter, the spatial relation is automatically extracted from the projection images with the help of a calibration target. With the calibrated spatial relation between the

imaging system and the manipulation system, the voxel size can be correctly calculated.

As stated in eq. (3.11), even with a calibrated system and a perfect imaging system, it is insufficient to reconstruct an object without artifacts when using a circular trajectory. In this chapter, a circle-line-circle trajectory is applied to the CT scan based on a known 3D surface scan.

5.1 Imaging system calibration

In this section, a reference sample based calibration is implemented. The calibration is calculated from the projection images only. This approach is less prone to reconstruction artifacts and enjoys a faster overall computation.

5.1.1 Perspective transformation model

An ideal imaging system in a CT setup can be modeled as a perspective camera. An illustration of a perspective camera is shown in fig. 5.1. O_c is the origin of the coordinate system of the camera. In an X-ray system, the camera center is replaced by the X-ray source. In this chapter, X-ray source and camera are used interchangeably. The image plane is defined by the *focal length* f, that is the distance between O_c and the image plane, and the *principle point* P, where the vector connecting O_c and P is perpendicular to the image plane. The ray O_cP is denoted as the *principle ray* of the model. O_d is the origin on the image plane and a point on the image plane is assigned with coordinates (u, v). In a camera system, the image area has a finite span and the center of the image area is at C. The imaging system is placed in a world coordinate system defined by O_w, x_w, y_w, z_w.

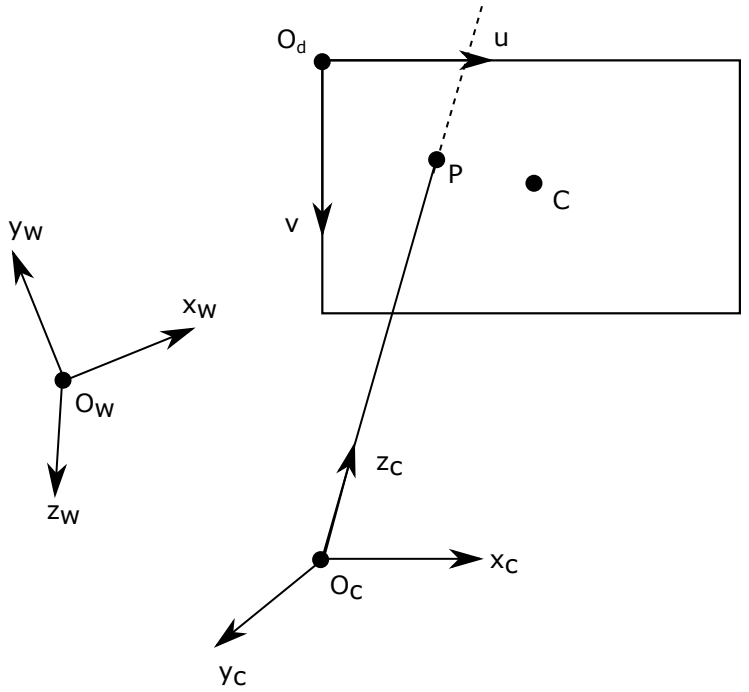

Figure 5.1: The schematic of a simplified perspective camera model. The three coordinate systems used in different reference frames are defined by 1) the origin O_w of the world coordinate system and the basis vectors x_w, y_w, z_w; 2) the origin O_c of the camera coordinate system and the basis vectors x_c, y_c, z_c; 3) the origin of the detector O_d and the basis vectors u, v. The world coordinates can be defined arbitrarily. In this chapter, the coordinate system used in the CMM measurement of the calibration target is used for this purpose.

In a perspective camera model without distortion, the projection of a point in the world coordinate system to the image coordinate system can be represented as:

$$\begin{pmatrix} u_0 \\ v_0 \\ 1 \end{pmatrix} = \underline{\underline{M}}_{int} \cdot \underline{\underline{M}}_{ext} \cdot \begin{pmatrix} x_{w0} \\ y_{w0} \\ z_{w0} \\ 1 \end{pmatrix}, \tag{5.1}$$

where

$$\underline{\underline{M}}_{int} = \begin{pmatrix} 1 & 0 & u_c \\ 0 & 1 & v_c \\ 0 & 0 & 1 \end{pmatrix} \begin{pmatrix} f_x & 0 & 0 \\ 0 & f_y & 0 \\ 0 & 0 & 1 \end{pmatrix} \begin{pmatrix} 1 & s/f_x & 0 \\ 0 & 1 & 0 \\ 0 & 0 & 1 \end{pmatrix} \tag{5.2}$$

and

$$\underline{\underline{M}}_{ext} = \left[\begin{array}{c|c} \underline{\underline{I}}_3 & \underline{T}_{wc} \end{array} \right] \left[\begin{array}{c|c} \underline{\underline{R}}_{wc} & \underline{0} \\ \hline 0 & 1 \end{array} \right]. \tag{5.3}$$

In the intrinsic matrix $\underline{\underline{M}}_{int}$, (u_c, v_c) is the coordinate of the center of the image area in the image coordinate system. f_x and f_y are the focal distances in horizontal and vertical direction. In case the pixels on the image plane have the same width and height, $f_x = f_y$. s is the skew factor to compensate the angle in the pixel arrangement on the image plane. Unlike the optical system for longer wavelength, the X-ray imaging system in an industrial transmission CT system does not contain any lens. Therefore, no lens correction needs to be applied to the X-ray imaging system. In this case, with a known intrinsic matrix, the X-ray imaging system is fully characterized.

The extrinsic matrix represents a rigid transformation defined by a rotation $\underline{\underline{R}}_{wc}$ and a translation $\underline{T}_{wc}$. Any point in the world coordinate system will be transformed into the coordinate system of the camera. Therefore, the extrinsic matrix is uniquely defined by the position of the camera in the world coordinate system.

The complete projection matrix $\underline{\underline{M}}_{int}\underline{\underline{M}}_{ext}$ has 11 degrees of freedom (DOFs). Assuming a perfectly manufactured detector with perpendicular arrangement of square pixels, the number of DOFs can be further reduced to 9. The projection matrix can be extracted if corresponding coordinates of points are available. Since each point will lead to two linear equations, at least 5 points are needed for this calculation.

5.1.2 Calibration sample design, fabrication and characterization

A planar checkerboard in black and white (as illustrated in fig. 5.2) is often used to calibrate a camera capturing visible light. The corners of the checkerboard can be located with sub-pixel accuracy as shown by Zhang *et. al.* [74]. However, as discussed in eq. (2.3), the contrast from an X-ray transmission imaging system comes from the line integral of the attenuation coefficient. According to eq. (2.5), a larger difference in thickness and a larger difference in atomic number will result in a better contrast. Another aspect is the extraction of the position of the corresponding image on the image plane. A checkerboard pattern with certain thickness will produce edges with smooth transition in gray values other than a sharp edge even without considering any other artifact. In addition, the edges will not be detectable when the *principle ray* is perpendicular to the

normal direction of the planar sample.

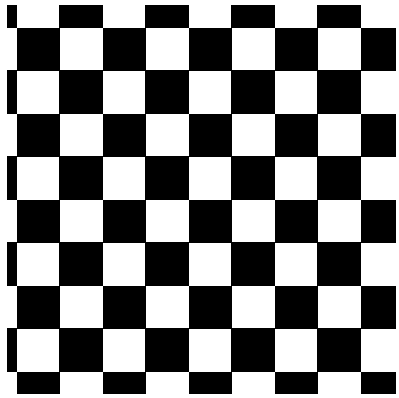

Figure 5.2: Checkerboard pattern used for optical camera calibration.

The design of a calibration target for an X-ray imaging system has the following concerns:

Ground truth measurement

As the CMM produces accurate and traceable results, the calibration sample needs to be CMM-friendly. According to the limitations of CMM subsection 2.3.2, the selection of the geometry of the features are reduced to the primitives. At the same time, the features need to be easily accessible by the tip of the CMM. Since the distance between the feature points are crucial to the calibration, the features have to be connected via a rigid body.

Material selection

The material choice for the feature structure and the supporting structure needs to enable high contrast in the X-ray image to improve the detectability of the features during calibration. According to eq. (2.5), the difference in atomic numbers should be as large as possible.

Number of detectable features

At least 5 correspondences are needed to calibrate the X-ray imaging system. Yet, due to the difficulty in the corresponding step during calibration, the number of features shouldn't be too high either.

As a result, a set of spheres arranged in a triple helix geometry are used as calibration targets as illustrated in fig. 5.3. The material of the spheres are Zirconia and the supporting structure is made of glass. The spheres are manufactured by *Saphirwerk*® and the nominal specifications are listed in tab. 5.1. The spheres are attached to a roughened conical flask as shown in fig. 5.4.The spheres are numbered from 1 to 12, according to vertical position and size of the sphere.

The assembled calibration target is measured with a CMM to produce a reference measurement. 9 points are measured by the CMM on each sphere to estimate the center and diameter of the sphere. The centers are recorded in the coordinate system of the CMM, which is located near the calibration target. The uncertainty from the CMM can be derived from the *Empa* standard operation procedure 01554.

The CMM result is listed in tab. 5.2. The center points are represented in the coordinate system of the CMM. As the exact coordinates will be used during

Diameter	Deviation	Roughness
40 mm	0.13 μm	0.014 μm
50 mm	0.13 μm	0.014 μm
60 mm	0.25 μm	0.020 μm

Table 5.1: The nominal specifications of the spheres from the manufacturer. The *Diameter* is the nominal diameter. The *Deviation* is the deviation from perfect sphere. The *Roughness* is the maximum allowed roughness.

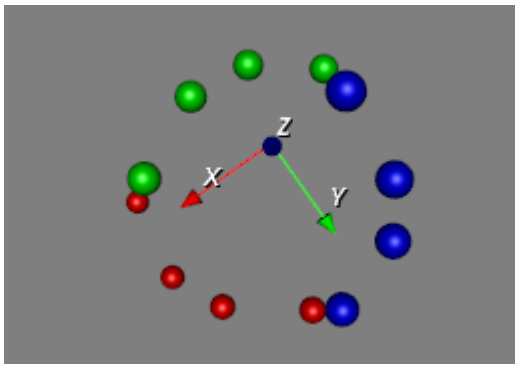

Figure 5.3: Rendering of the spherical features of the calibration target. The spheres are color coded according to their diameters. The sphere are arranged in a triple helix structure. Spheres of the same size are arranged in one helix. The arrangement in helix and the selection of spheres with different diameters reduce the chance of transits and facilitate the correspondence of the projection images with the spheres.

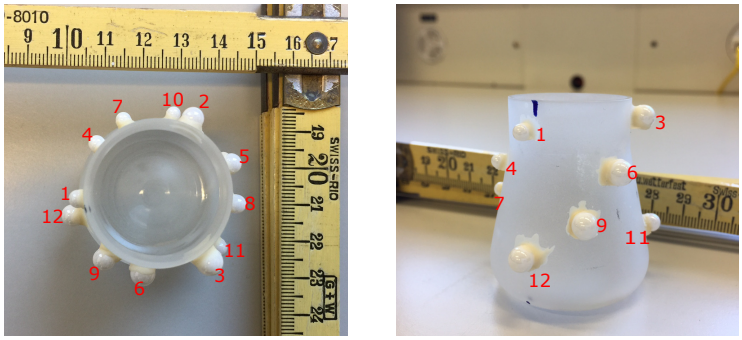

Figure 5.4: Photos of the calibration target from top and side view. The spheres are numbered from 1 to 12, according to the vertical position and size of the sphere.

the next steps in calibration, the same coordinate system will be referred to the object coordinate system.

5.1.3 Measurement

The calibration target is scanned in a CT system which has been calibrated in the factory. The scanning parameters are listed in tab. 5.3 and tab. 5.4. Before the scan, the calibration target is placed on the manipulator with the axis of the flask coarsely aligned to the axis of rotation. 1440 projection images are taken with an angular increment of 0.25 degrees.

5.1.4 Point extraction and correspondence

In this subsection, firstly, the exact coordinates in the detector coordinate system of the projections of the feature structures on the projection images are extracted and, secondly, the coordinates in the reference frame of the detector are corresponded to coordinates of the features in the reference system of the object.

Number	x [mm]	y [mm]	z [mm]	r [mm]	uncertainty [μm]
1	4.393	17.152	14.247	4.001	2.83
2	13.241	-12.400	14.433	5.002	2.83
3	-17.581	-5.840	16.189	6.001	2.83
4	15.718	9.921	4.546	3.996	2.83
5	1.119	-19.147	4.058	5.000	2.83
6	-16.976	9.169	5.268	5.998	2.83
7	20.663	2.050	-6.105	3.997	2.83
8	-9.245	-18.862	-5.411	4.996	2.83
9	-11.994	17.915	-5.272	5.995	2.83
10	19.066	-11.594	-14.128	4.002	2.83
11	-19.702	-11.744	-13.955	5.002	2.83
12	1.299	23.379	-13.869	6.001	2.83

Table 5.2: The coordinates of the spheres and the diameter of the spheres in the calibration target measured by a CMM.

Source settings	Value	Unit
Voltage	229	kV
Current	43	μA

Table 5.3: Source settings

Detector settings	Value	Unit
Horizontal dimension	1880	pixel
Vertical dimension	1496	pixel
Pixel pitch	0.127	mm

Table 5.4: Detector parameters

Segmentation

The raw image contains the projections of the feature structure and the supporting structure. Although the materials have been selected to have a large difference in the linear attenuation coefficient, the cumulated attenuation coefficient from the supporting material is sometimes comparable to the cumulated attenuation of the features Therefore, a simple gray value based segmentation is insufficient. The objective of the segmentation in this step is to roughly locate the feature structure and remove as much as possible other non-feature structures.

The following procedures create a mask (fig. 5.5(d)) of a subset containing the projections of the spheres. The projection image (fig. 5.5(a)) is firstly segmented using a simple threshold (fig. 5.5(b)). After the thresholding, both the projections of the feature structure and supporting structure are labeled. Secondly, morphological filters are applied to the thresholded image to remove the narrow stripes from the supporting material. Specifically, several iterations of erosion filters are applied to the image followed by dilation filters. The number of erosion filtering iterations depends on the widest part of the stripes. The stripes are removed completely after the erosion step (fig. 5.5(c)). The following dilation process restores the areas where the feature structures are. As the objective is just to roughly locate the features, several more iterations of dilation are applied to ensure no part of the features will be lost.

Circular Hough Transform

The coordinates of the centers of the spheres are measured by CMM. In this step, the projection of the centers needs to be extracted from the projection images to allow further calculations. In a cone-beam imaging system, the projection of a sphere on the detector is an ellipse unless the center of the sphere

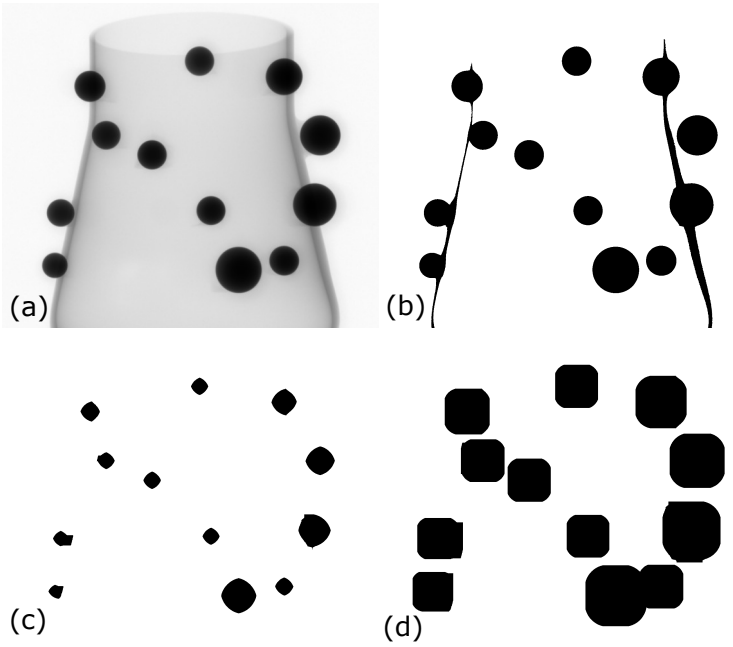

Figure 5.5: (a) shows one projection of the calibration target. The dark circles are the projection of the spheres made of Zirconia. The other structure in the projection image is the flask made of glass. (b) shows the result of thresholding. (c) shows the result after erosion. This operation removes the projections of the walls of the flask. (d) shows the result after dilation. The result can be used as a mask to select regions where further processing shall be applied.

is located on the principle axis of the imaging system. However, considering the small cone angle used in the imaging system, the resulting projections are ellipses with eccentricities close to 0. Therefore, the projections will be detected as circles and the centers of the circles will be taken as the projections of the centers of the spheres.

The detection of circles in the projection image is achieved by Circular Hough Transform as explained by Rizon *et. al.* [60]. In a Circular Hough Transform, an edge detection filter is applied to the image first to locate any edge that can be on a circle. For a given radius and given edge pixels, all pixels in the image that could be on a circle centered at the given edge pixels are targeted. This is followed by repeating the same procedure for all edge pixels and voting on the most likely pixels being the center of a circle with the given radius. To detect circles with different radii, the above procedures are repeated.

In this dissertation, the implementation from Matlab [47] is used to detect the center and the radius of the circles in the projection. As an example, the detected circles from fig. 5.5(a) are illustrated in fig. 5.7(a).

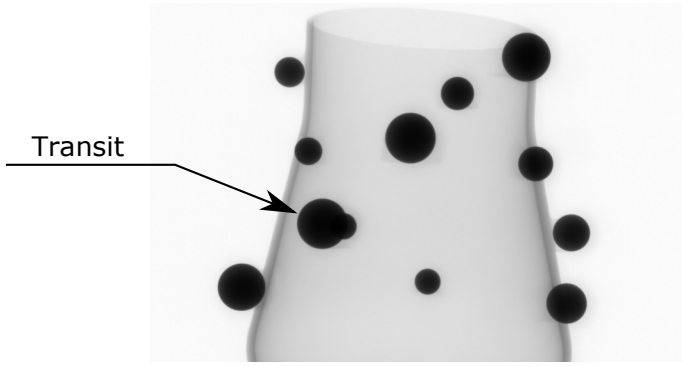

Figure 5.6: Projection of the calibration target with transit of two spheres.

Due to the nature of the transmission imaging system, the projection circles may transit each other in the projection image as shown in fig. 5.6. In case of sufficient transmission, the boundaries of both circles in transit can be extracted from the edge detector. However, the limited acquisition time and the low source voltage from the micro CT systems result in missing boundaries which makes the circle detection difficult. As a result, there might be circles missing.

Correspondence

The extracted circles from the Circular Hough Transform need to correspond to the spheres in the calibration target. To achieve the correspondence, the diameters and the vertical location of the spheres are firstly used. As the axis of the conical flask is coarsely aligned to the rotation axis and the calibration is placed close to the center of the detector, the circles on the projection image can be separated into groups according to their vertical location fig. 5.7(b). Within each group, the circles are identified according to their diameter fig. 5.7(c).

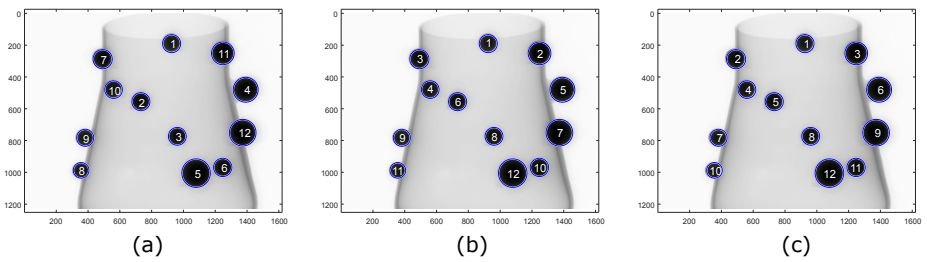

Figure 5.7: (a) shows the result from the circle detection program. (b) shows the result by sorting the circles according to their vertical coordinates in the reference frame of the detector. Afterwards, the circles are grouped according to the vertical coordinate intervals. (c) shows the result after sorting within each group.

However, since the spheres have difference magnifications due to their different distances to the source, the diameter of the circles is insufficient to

identify the spheres in the calibration target. To demonstrate this problem, the radius of the detected circles is plotted in the projection images in fig. 5.8(a). The radii of circles number 10, 11 and 12 are highlighted to illustrate the problem. The gray bar indicates the discarded projection where certain circles are not detected due to transits and therefore neglected from further analysis. The horizontal axis is the projection index which indicates the scanning angle in case of a circular trajectory.

To correspond the correct circle to the spheres on the calibration target, the coordinates of the centers of the circles are used as constraints. As the projections are acquired along a circular trajectory and all the spheres are in the field of view, the change of the center coordinates is small. Any jump in the coordinates as shown in fig. 5.8(a) or in fig. 5.9(a,b) indicates a mis-correspondence. The mis-correspndence are corrected using Algorithm 3.

Algorithm 3 Correspondence

1: **procedure** CORRESPONDENCE
2: Input: Radii, vertical coordinates, horizontal coordinates
3: Output: Correspondence between the detected circles and the spheres
4: Sort *w.r.t.* the vertical coordinate into 4 groups. g_1, g_2, g_3, g_4
5: Sort *w.r.t.* the radius within each group g_i
6: Discard measurements with missing circles
7: Locate jumps in either horizontal coordinate or vertical coordinate
8: Re-correspond utilizing the jumps in coordinates
9: **end procedure**

5.1.5 Extract intrinsic matrix

The direct linear transformation (DLT) method, initially developed by Abdel *et. al.*[2] is used to extract the intrinsic matrix. The DLT method utilizes the

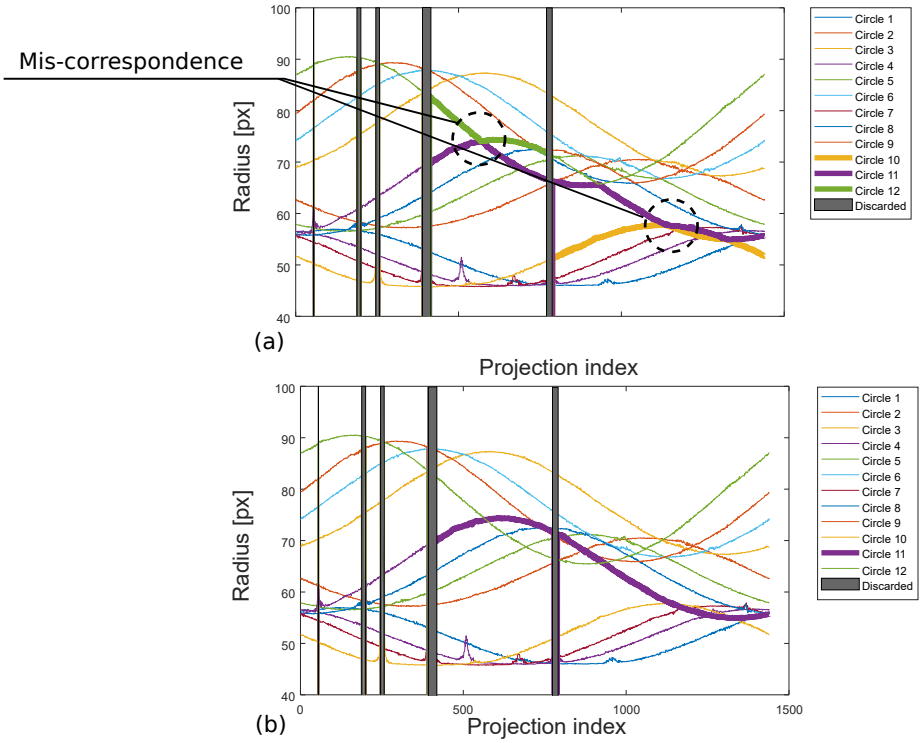

Figure 5.8: The traces are colored according to their correspondence. The radii of the circles are plotted against the projection index. Mis-correspondence occurs when two traces cross each other. The thickened traces show examples of a circle mis-corresponded twice. The radii of the circles are plotted again in (d) after correction of the mis-correspondence. Gray bars indicate discarded views. Projection index indicates the scanning angle in case of a circular trajectory.

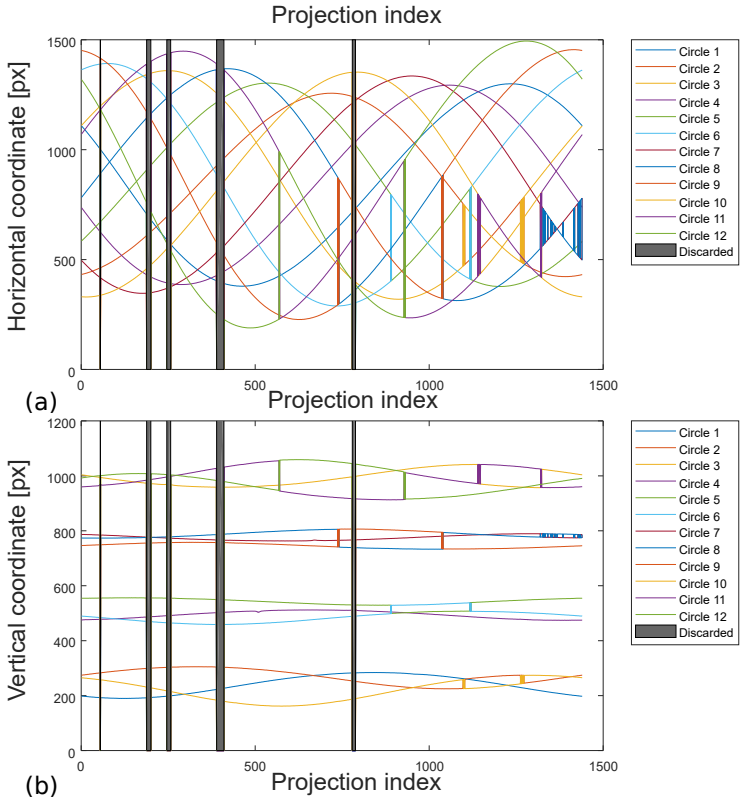

Figure 5.9: The traces are colored according to their correspondence. The radii of the circles are plotted against the projection index. Mis-correspondence occurs when two traces cross each other. The horizontal and vertical coordinates of the circles are plotted in (a) and (b).

known 3D coordinates $(x_w, y_w, z_w)^T$ of the feature in the reference frame of the object and the 2D coordinates (u, v) of their projections in the reference frame of the detector. The CT imaging system is modeled as a pin-hole system during the calibration. According to eq. (5.5), every correct correspondence will result in two linear equations.

The projection matrix is denoted as:

$$\underline{\underline{M}}_p = \underline{\underline{M}}_{int} \cdot \underline{\underline{M}}_{ext} = \begin{pmatrix} m_{11} & m_{12} & m_{13} & m_{14} \\ m_{21} & m_{22} & m_{23} & m_{24} \\ m_{31} & m_{32} & m_{33} & m_{34} \end{pmatrix}, \tag{5.4}$$

The intrinsic and extrinsic matrices are explicitly expressed in eq. (5.2) and eq. (5.3).

The correspondence between $(u_i, v_i)^T$ and (x_{wi}, y_{wi}, z_{wi}) can be expressed as eq. (5.5).

$$\begin{cases} -x_{wi}m_{11} - y_{wi}m_{12} - z_{wi}m_{13} - m_{14} + u_i x_{wi}m_{31} + u_i y_{wi}m_{32} + u_i z_{wi}m_{33} + u_i m_{34} = 0 \\ -x_{wi}m_{11} - y_{wi}m_{12} - z_{wi}m_{13} - m_{14} + v_i x_{wi}m_{21} + v_i y_{wi}m_{22} + v_i z_{wi}m_{23} + v_i m_{24} = 0. \end{cases} \tag{5.5}$$

If the elements in $\underline{\underline{M}}_p$ are rearranged into a vector $\underline{v}_p$ and put all the coefficients from all the correspondence from a single projection into a matrix $\underline{\underline{C}}$, the projection can be represented as:

$$\underline{\underline{C}} \cdot \underline{v}_p = \underline{0}. \tag{5.6}$$

With 12 correspondences in each projection, the linear equations can be

solved in a least square sense using the pseudo inverse method. However, due to the noise in the projection images, the extracted 2D coordinates (u_i, v_i) are not exact. This leads to inconsistent equations in eq. (5.6) and, as a result, the solution from the pseudo inverse contains high uncertainty. To increase the accuracy of $\underline{v}_p$, all the projection images are used at once. Without considering the drift of the focal spot, the geometry of the imaging subsystem is identical throughout the acquisition, which indicates the intrinsic part of the projective matrix from every single acquisition stays the same.

If the intrinsic parameters in eq. (5.6) is denoted as $\underline{\alpha} = u_c, v_c, f_x, f_y, s$ and the extrinsic parameters from ith projection as $\underline{\beta}_i = \beta_{i1}, \beta_{i2}, \beta_{i3}, \beta_{i4}, \beta_{i5}, \beta_{i6}$, the calibration problem can be formulated as an optimization problem:

$$\underline{\alpha} = \underset{\{\underline{\alpha}, \underline{\beta}_1, \ldots\}}{\arg\min} \sum_{i=1}^{i=n} \| (u_i, v_i) - f_{\underline{\alpha}, \underline{\beta}_i}(x_{wi}, y_{wi}, z_{wi}) \|_2^2, \tag{5.7}$$

where $f_{\underline{\alpha}, \underline{\beta}_i}$ is a symbolic operator for projection and n is the number of projections.

5.1.6 Imaging system calibration result

In this subsection, the above methods are applied to the calibration data acquired from a micro CT setup as described in subsection 5.1.3. The implementation from Bouguet [13] is used to perform the calculation. The least square problem (eq. (5.7)) is solved iteratively using the gradient descent method in this implementation. The optimization converges after about 10 iterations. The residual over iteration is plotted in fig. 5.10 The result of the calibration of the imaging subsystem is demonstrated by the following experiments.

The focal distance and the coordinate of the principle point are extracted

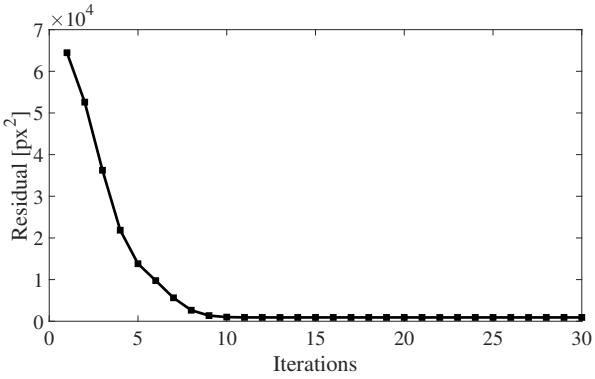

Figure 5.10: The residual after each iteration.

using the calibration procedure from different number of projections. The projections used for the calculations are always uniformly distributed in $[0, 2\pi]$. The projections that contain undetected circles due to transits are counted in the number of projections but not included in the calculation. The envelope of the confidence interval calculated from the residual is shown in fig. 5.11.

5.2 Manipulation system calibration

The extrinsic parameters extracted from the calibration system describe the transformation from the reference frames of the object and the imaging system. The change of the extrinsic parameters extracted from different projections are results of the sample manipulation. In theory, the calibration system can be calibrated from the same procedure and the trajectory used for the acquisition can be extracted. However, due to the small number of feature points available in each projection, the uncertainty of the extrinsic parameters is too large for

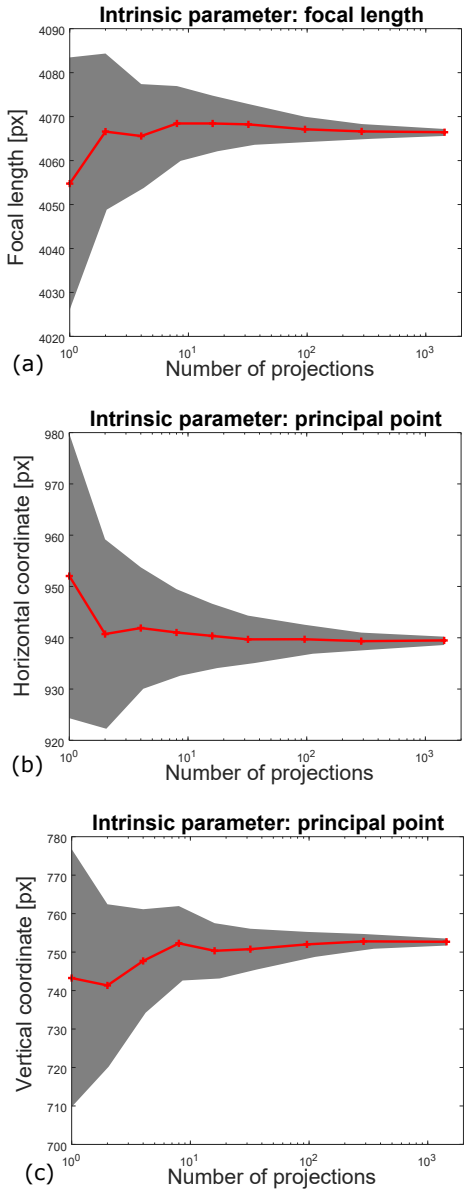

Figure 5.11: The estimated focal length and the coordinate of the principle point are plotted in (a) and (b)(c) against the number of projections used for the estimation. The gray envelope indicates the uncertainty of the estimation.

calibration.

5.2.1 Extract trajectory

As shown in eq. (5.3), the extrinsic matrix transforms any point in the reference frame of the object to a point in the reference frame of the camera system. To extract the position of the camera in the reference frame of the object, the coordinate of the origin of the camera system is calculated using the inverse extrinsic matrix.

If the extrinsic matrix is represented using homogeneous coordinates, the inverse matrix is:

$$\underline{\underline{M}}_{ext}^{-1} = \left[\begin{array}{c|c} \underline{\underline{R}}_{wc}^{-1} & \underline{\underline{R}}_{wc}^{-1}\underline{T}_{wc} \\ \hline 0 & 1 \end{array}\right]. \tag{5.8}$$

Therefore the coordinates of the camera in each projection can be calculated as

$$\underline{\underline{R}}_{wc}^{-1}\underline{T}_{wc} \tag{5.9}$$

The result is visualized in fig. 5.12.

The extracted camera positions in the reference frame of the object form a circle, which is expected as a standard circular trajectory is applied during the acquisition. The notches along the circle indicate the views that are not taken into the calculation due to the missing feature points as a result of transits (illustrated in fig. 5.6).

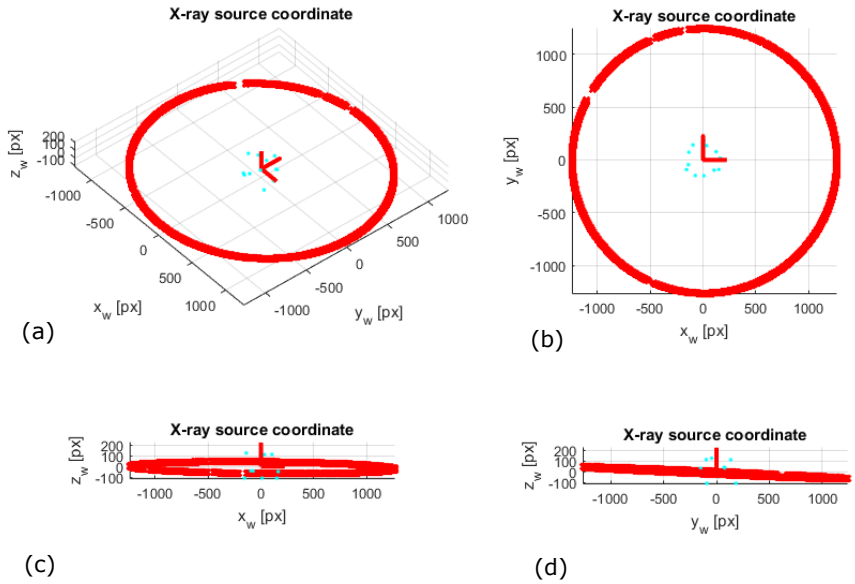

Figure 5.12: The 4 plots show a set of scattered points in isometric view (a), x-y view (b), x-z view (c) and z-y view(d). The centers of the spheres on the calibration target are plotted as blue dots near the origin of the coordinate system. The extracted camera positions (X-ray source positions) are plotted as red dots and they form a circle around the origin. The gaps on the circle indicate the discarded views.

5.2.2 Extract rotation axis

During the acquisition along a circular trajectory, the only manipulation of the sample is the rotation of the sample. Without considering the movement of the rotation axis, the camera positions in the reference frame of the object is a circle. Therefore, a circle is fitted to the extracted camera positions to extract the rotation axis.

As an approximation, the fitting is done in two steps, i.e. fitting a plane to the points and fitting a circle to the projection of the points on the plane. The plane fitting follows Algorithm 4.

Algorithm 4 Correspondence

procedure FIT A PLANE TO 3D POINTS
    Input: The coordinates of a set of points $\underline{x}_i$
    Output: The normal vector $\underline{n}$ and a point on the plane $\underline{p}_c$ of the a plane
    Calculate the centroid $\underline{p}_c$ of the points $\underline{x}_c$
    Calculate the vectors $\underline{v}_i = \underline{x}_i - \underline{x}_c$
    Calculate the covariance of the vectors $\underline{\underline{V}}^{-1}\underline{\underline{V}}$
    Calculate $\underline{n}$ as the eigenvector with the smallest eigenvalue.
end procedure

After projecting all the points to the plane, a circle is fitted to the projections following Algorithm 5

Algorithm 5 Correspondence

procedure FIT A CIRCLE TO 2D POINTS
    Input: The coordinates of a set of points $\underline{p}_i$
    Output: The radius and the center of a circle that is fitted to the points.
    Parameterize the circle as $p_x^2 + p_y^2 + a_1 p_x + a_2 p_y + a_3 = 0$
    solve the parameters in a least square manner.
    Calculate $\underline{n}$ as the eigenvector with the smallest eigenvalue.
end procedure

The extracted axis of rotation is illustrated in fig. 5.13. In fig. 5.13(a), the circle fitted to the camera positions is illustrated as well as a line along the normal direction of the circle going through the center of the circle. The line is an illustration of the rotation axis in the reference frame of the object. The projections of the rotation axis using the extrinsic parameters from each projection are plotted in fig. 5.13(b) together with the geometric center of the detector and the principal point of the imaging subsystem. A zoom-in view in fig. 5.13(c) reveals the misalignment of the imaging system and the manipulation system. The difference between the projection of the nominal rotation axis and the extracted axis at the vertical center of the detector is less than $0.2 pixels$, which validates the calibration method in this chapter. The deviation of the extracted rotation axis is an indicator of the accuracy of the result. The deviation is unlikely to be zero due to the errors from the extraction of the coordinates on the detector and other processes of the calculation.

5.3 Arbitrary trajectory

Tuy's conditions eq. (3.11) have stated that an acquisition along a circular trajectory cannot collect sufficient data to reconstruct the exact 3D object. One particular artifact associated with the insufficient data is the cone beam artifact fig. 3.2. Cho *et. al.* [23] and Zeng *et. al.* [73] have applied helical trajectory to acquire data using a cone beam setup to reduce the cone-beam artifact. However, to execute such a trajectory, the manipulation system must be able to perform rotation and translation in a coordinated manner. At the same time, to prevent artifacts from misalignment, the manipulation system must be accurate while performing rotation and translation. To lower the demand on the

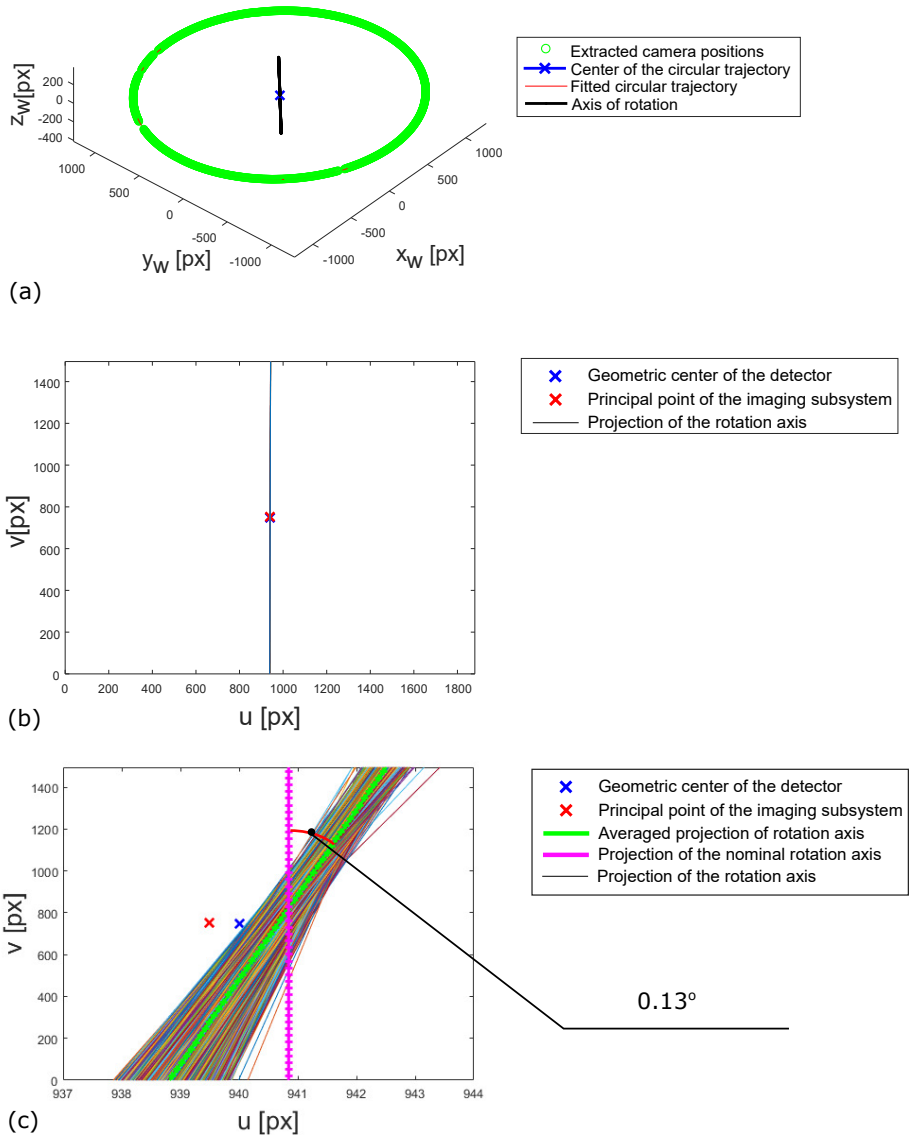

Figure 5.13: The extracted center of the circular trajectory is marked as a blue cross in (a) and the axis of rotation is marked by a back line. The projection of the extracted axis of rotation is plotted in (b) which indicated the system is well aligned. (c) shows a horizontal zoom in view. The blue cross is the geometric center of the detector and the red cross is the principle point. The nominal axis of rotation is marked by the magenta line and the green line is the extracted axis of rotation which is an average of the projections of the rotation axis from different views.

mechanical system of the sample manipulator, the circle-line-circle trajectory is used to acquire projection images.

5.3.1 Circle-line-circle trajectory

The circle-line-circle (CLC) trajectory adds a second circle and a line segment to a standard circular trajectory as illustrated in fig. 5.14. The two circles have the same radius and are parallel to each other. The line segment connecting the circles is perpendicular to the planes of the circles. The radius of the circle is the source to iso-center distance, *sid*. The scanning starts at the intersecting point of the line segment and the bottom circle. Firstly, a circular scan is executed. Following the circular scan, the acquisition continues while the image system travels *w.r.t.* the object along the line segment. Finally, a second circular scan is performed. Using the notation from eq. (2.6), the CLC trajectory can be denoted as:

$$\begin{aligned}\{&\underline{\underline{T}}(\theta,0,0),\ ...,\ \underline{\underline{T}}(\theta+k\Delta\theta,0,0),\ ...,\ \underline{\underline{T}}(\theta+2\pi-\Delta\theta,0,0),\\ &\underline{\underline{T}}(\theta+2\pi-\Delta\theta,\Delta l,\Delta l),\ ...,\ \underline{\underline{T}}(\theta+2\pi-\Delta\theta,H,H),\\ &\underline{\underline{T}}(\theta+2\pi,H,H),\ ...,\ \underline{\underline{T}}(\theta+4\pi-\Delta\theta,H,H)\},\end{aligned} \quad (5.10)$$

where Δl is the step size in vertical translation.

5.3.2 Sample preparation

The cone-beam artifact reduced the spatial resolution in the direction of the rotation axis, leading to an anisotropic spatial resolution in a 3D image. As a result, boundaries that are parallel to the circular trajectory plane are blurred as

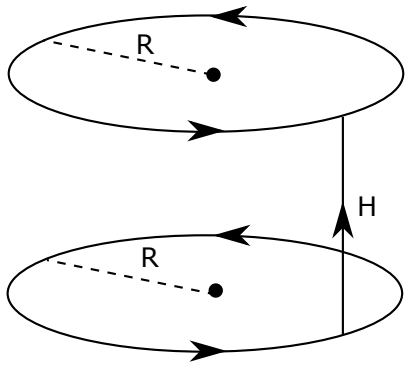

Figure 5.14: Schematic of the circle-line-circle trajectory. It is composed of two circles and a line segment.

illustrated in fig. 3.2. To study the cone-beam artifact, a cuboid-shaped sample illustrated in fig. 5.15 is fabricated.

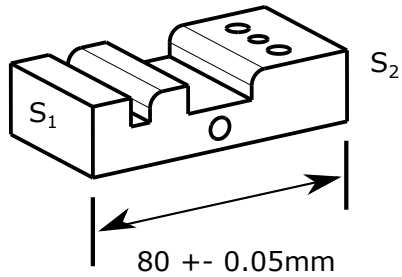

Figure 5.15: Isometric view of the test sample 1A. S_1 and S_2 are two opposing surfaces.

The two surfaces S_1 and S_2 are parallel and are approximately $80mm$ apart from each other. The cone-beam artifact is expected to occur at one surface if the other surface is in the plane of the circular trajectory.

A set of similar samples varying in length are fabricated. The particular

sample used in this study is named as sample 1A.

5.3.3 Optical surface scan

Sample 1A is scanned with a structured light 3D surface scanner from *Breuckmann*. The scanner used in this experiment is the *SmartScan 3D SM2069-HE5* which features a 5 mega pixel camera offering a resolution of 18 μm. Before the scanning, the scanner was calibrated by a calibration target following a calibration work flow provided by the equipment manufacturer. During the scan, the sample was placed on a rotation stage. Projection patterns at different spatial resolution are projected onto the surface of the sample to extract the surface features at different scales. To acquire the complete surface, the sample is rotated and measured from different directions. The result is denoted as $\mathcal{M}_{1A}$ and illustrated in fig. 5.16.

5.3.4 CT scan

The setup used to acquire the transmission projection images is composed of an industrial X-ray tube with a maximum acceleration voltage of $450kV$ and a flat-panel detector as well as a sample manipulator capable of performing rotation around one axis and translation along one axis. The specification of the detector is listed in tab. 5.5.

Scanning parameters

The distance between the two circles in the CLC trajectory (H in fig. 5.14) comes from the optical result. To minimize the cone-beam artifact, the distance is set to the span of the sample in the direction of the rotation axis. The scan along each of the circular trajectory has an angular increment of 1 degree. The

Figure 5.16: Optical scanning result of the test sample. This is the rendering of the mesh. Part of the texture is also recorded. The boundaries on the texture indicate the stitching boundaries. The visible surface of the sample is well represented. The mesh contains defects at the bottom of the trenches and the bottom of screw holes.

XRD 1621 AN14 ES	
Manufacturer	Perkin Elmer
Pixel count	2048×2048
Pixel pitch	200 mm^2
Area	409.6×409.6 mm^2
Scintillator	DRZ-Plus 208 Gd_2O_2S:Tb

Table 5.5: Specifications of the flat-panel detector.

scan along the line segment has an increment of 1 mm in translation. The resulting trajectory is parameterized and stored in a proprietary trajectory file which will be used in the control software.

Projection from CLC trajectory

The raw data acquired from the detector is stored in a stack of projection images. Several preprocessing are applied to the raw data, *i.e.* normalization *w.r.t.* the difference of the flat field image and dark field image, negative logarithmic operation and bad pixel removal. The resulting image stack is illustrated in fig. 5.17. The z direction is the projection index. The pixel values can be arranged into the projection vector, $\underline{p}_{clc}$ as defined in eq. (2.14). A slice of the stack across the projection index, marked in fig. 5.17(a), is plotted in fig. 5.17(b). The projection data from the circular scans and translational scan can be clearly distinguished from this view.

To illustrate the improvement from employing the CLC trajectory, the reconstruction from a CLC trajectory is compared to the reconstruction from a circular trajectory. The circular trajectory used is the first circle of the CLC trajectory. The projection acquired from the scan using the circular trajectory is denoted as $\underline{p}_{fc}$, which is shown in fig. 5.17(b). The specification of $\underline{p}_{clc}$ is summarized in tab. 5.6:

Parameter	Value
Dimension	$950 \times 1400 \times 792$
Pixel size	$0.2 \times 0.2\ mm$

Table 5.6: Specification of the projection images acquired from a circle-line-circle trajectory.

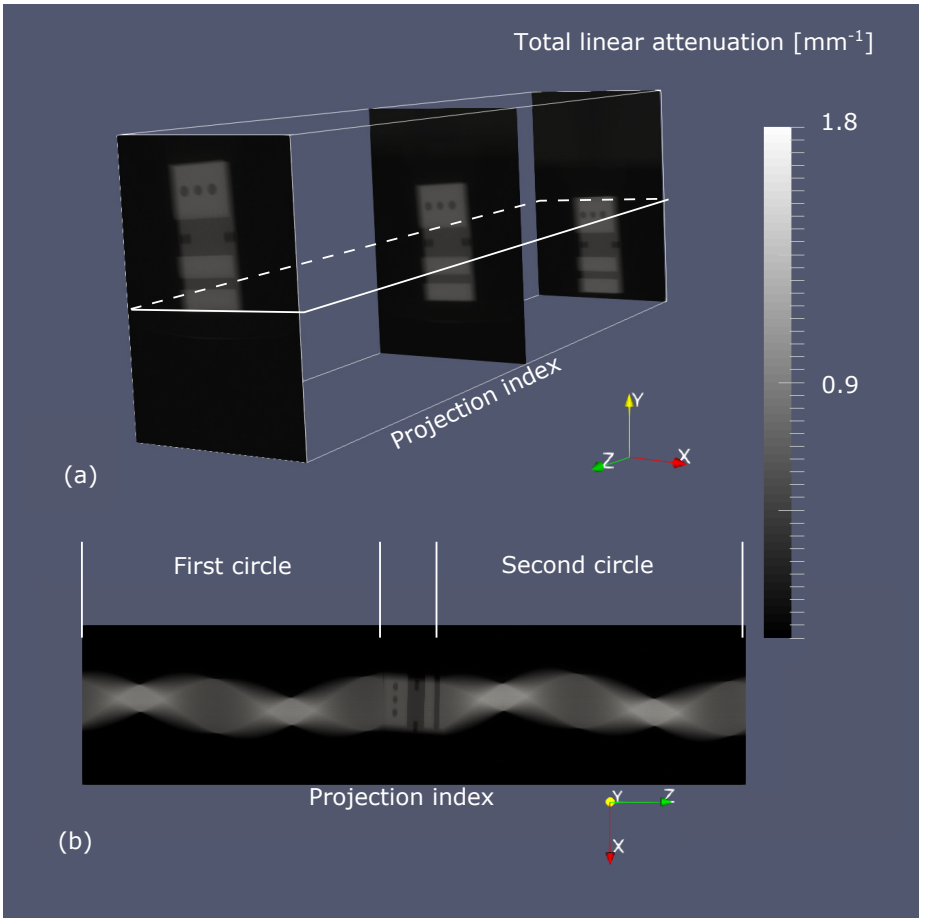

Figure 5.17: (a) illustrates the projection images acquired with a CLC trajectory. The three images shown in (a) are taken from views in the first circle, line segment and the second circle of the CLC trajectory. The area marked by white solid and dashed lines across the projection index is used to slice the projection stack. The slice is shown in (b).

5.3.5 Reconstruction

The subset $\underline{p}_{fc}$ is reconstructed using the standard FDK algorithm (eq. (3.15)). The particular implementation used to produce the result below is from the openRTK toolkit developed by Rit *et. al.* [59]. The reconstruction region is defined by a point in the reference frame of the object and the number of voxels in each direction and the voxel size as shown in tab. 5.6.

An expectation maximization algorithm is employed to reconstruct the object from the projection data acquired with the CLC trajectory . The implementation is based on the openRTK toolkit developed by Rit *et. al.* [59]. The reconstruction region is the same as the one used in the reconstruction from the subset for easy comparison.

5.3.6 Result

The reconstructed objects are illustrated in fig. 5.18. The reconstruction from the CLC dataset is shown in fig. 5.18(a)(b) and the result from the circular scan is shown in fig. 5.18(c)(d). To visualize the 3D objects, contours thresholded at $0.02mm^{-1}$ are extracted and rendered in fig. 5.18(a)(c). A 3D rendering of the contour offers an intuitive way to inspect the external geometry of the object. For detailed analysis, a slice is taken from each reconstructed volume (fig. 5.18(b)(d)). The cone-beam artifact is clearly visible at the upper boundary of the slice which is taken from the reconstruction from the circular subset $\underline{p}_{fc}$. Line profiles across the slices are plotted in fig. 5.19 to qualitatively study the cone beam. The profile is calculated from a rectangular region bing 40 pixels wide and centered at the line marked in fig. 5.18(b)(d). The profiles at the boundary between the sample and air are plotted at a finer scale in

fig. 5.19(b)(c). The horizontal lines are drawn at 80% and 20% of the maximum value in the profile respectively as references. One way to measure the response of the edge is to measure the span of the edges in the profile. The results are listed in tab. 5.7:

With only one circular trajectory, the cone-beam artifact at the boundary far from the trajectory plane is prominent, leading to a larger span of edges. The reconstruction from the dataset acquired from a CLC trajectory shows almost the same spans at both the rising edge and the falling edge. The correction of the cone-beam artifact using CLC trajectory is due to the employment of a CLC which meets the Tuy's conditions.

A region in the slice (fig. 5.18(b)) is selected as feature region to estimate the noise level inside the object. The histograms of the pixel values in the selected region are plotted in fig. 5.20. To describe the distribution of the pixel values, a Gaussian distribution is fitted to the histogram and the standard deviations are calculated as one metric for the noise performance. From the measurements, the EM algorithm reduces the noise by 60 %.

5.4 Discussion

The methodology adopted for the calibration does not require any reconstruction of the volume. This isolates the calibration problem from the reconstruction

	Rising edge	Falling edge
CLC	0.36 mm	0.37 mm
Circular	0.43 mm	1.70 mm

Table 5.7: The span of the rising and falling edges

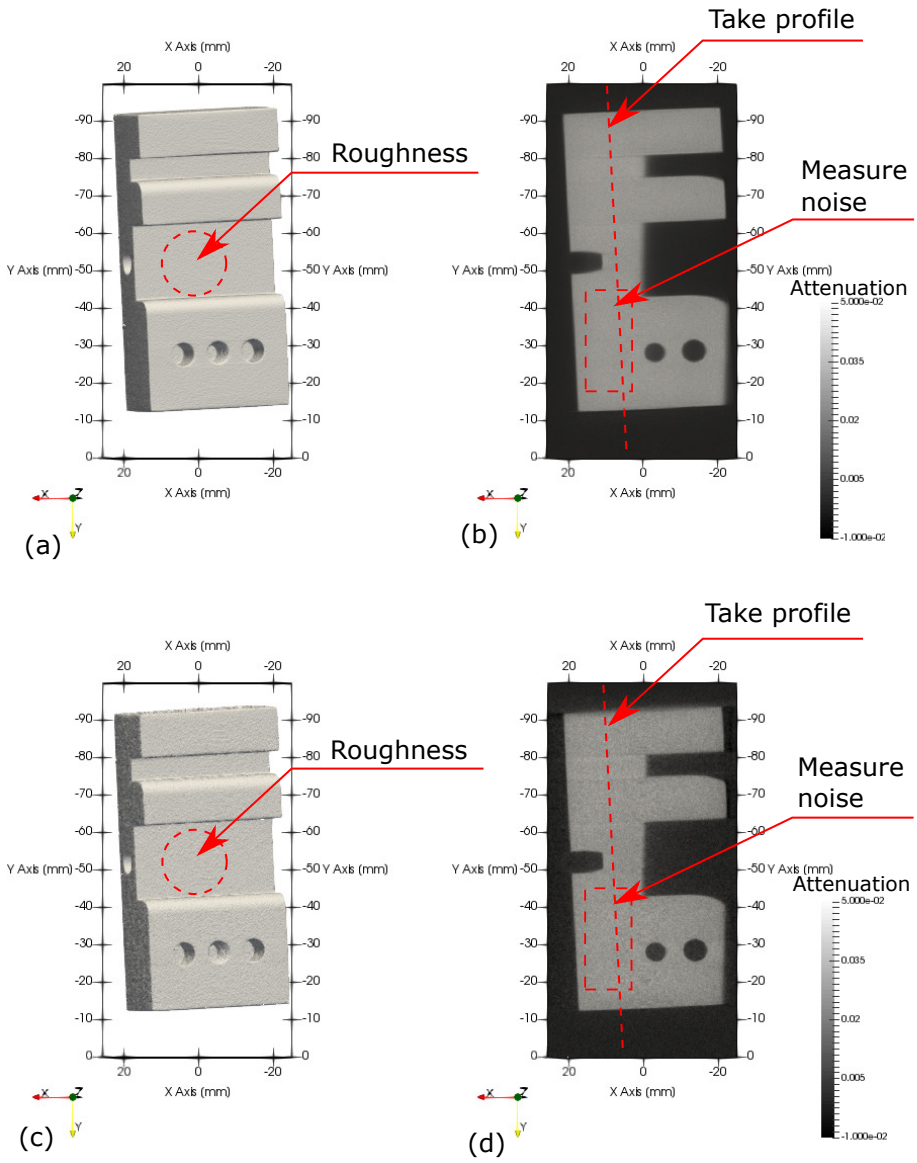

Figure 5.18: The reconstruction result from a CLC trajectory is shown in (a) and (b). The reconstruction result from a circular trajectory is shown in (c) and (d). The isosurfaces in (a) and (c) are extracted using the same parameter ($0.02mm^{-1}$).

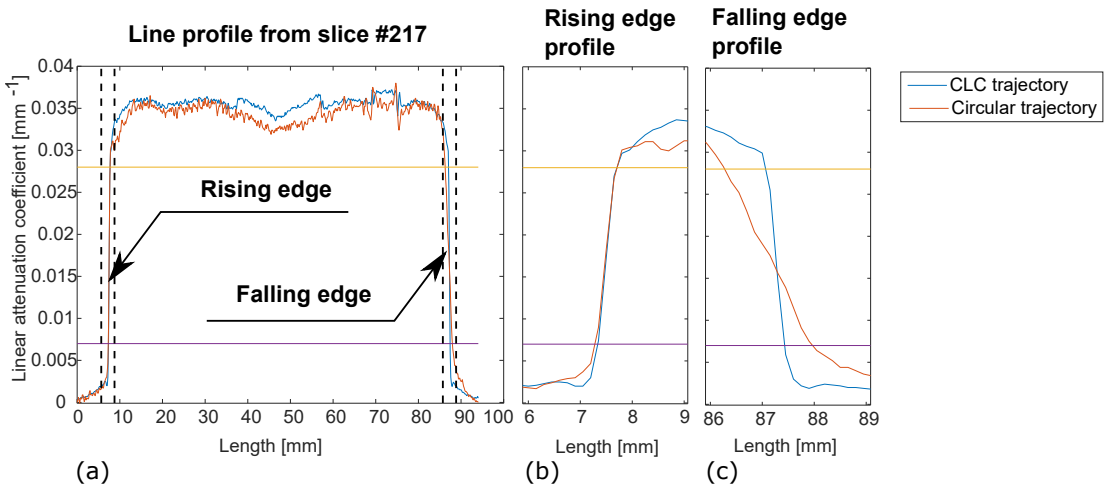

Figure 5.19: The line profile extracted along the line marked in fig. 5.18 is shown in (a). The zoomed views at the rising and falling edge are plotted in (b) and (c).

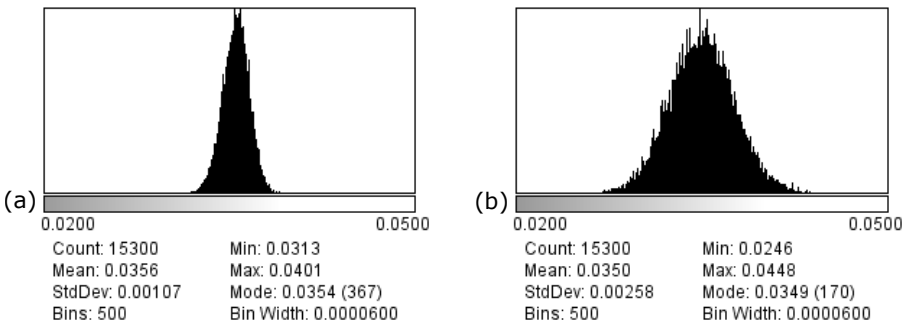

Figure 5.20: The histogram of pixel values in the area marked in fig. 5.18. The result from the EM algorithm with CLC is shown in (a) and the result from the RTK algorithm with a circular trajectory is shown in (b).

problem. Therefore, this calibration approach is less prone to reconstruction artifacts. At the same time, the result from this approach offers absolute voxel size enabling dimensional measurements. Compared to manual alignment, this approach serves as a fast solution which also requires less intervention from operators. The fabrication of the calibration target does not require any precision tool, this approach is practical to implement. On the other hand, this approach requires one additional measurement after each system modification and it requires similar calibration targets of different sizes to calibrate systems with different detector sizes. It is worth noting that the algorithm used to locate the projections of the center of the sphere can be improved. An implementation to fit ellipses to the projections would increase the accuracy, which will reduce systematic errors. This approach also has the potential to detect wobbling or to extract arbitrary trajectory.

Another geometric factor in the imaging subsystem is the focal spot size. One solution that is implemented within the frame of this dissertation is to simulate the source with multiple sources with various intensities. Preliminary results are promising and this solution will be investigated in subsequent projects.

The CLC trajectory is just one of many possible trajectories fulfilling Tuy's conditions. Considering the limitation of the manipulation system, the CLC is selected because of its simplicity. The EM algorithm presented in this chapter is able handle trajectories other than CLC without significant modifications.

Chapter 6

Data fusion

So far, the prior information has been used in the data acquisition process to suggest scanning trajectories fulfilling Tuy's conditions. In this chapter, the employment of prior information in the reconstruction process is investigated. With existing CT projection data, is it possible to improve the reconstruction by fusing optical scanning data acquired separately? More precisely, is it possible to mitigate the limited-angle artifacts by fusing optical data with CT data? To answer these questions, two key problems are investigated, (1) the alignment of the two dataset acquired in different reference frames and stored in different representations and (2) the data fusion model to merge the two data sets to achieve synergy.

6.1 Alignment

The alignment is a process to bring measurements in different coordinate systems into one common coordinate system. The reconstruction volume is defined in the coordinate system of the object. Its origin is defined as the intersecting point of the rotation axis and the trajectory plane if a circular trajectory is used for the CT acquisition. In the case of an arbitrary trajectory, the origin of the coordinate system can also be arbitrarily defined. A Cartesian coordinate system is defined with the origin and a set of basis vectors. The orientation of the basis vectors can be arbitrarily assigned, although it is a common practice to align one basis vector with the rotation axis if a circular trajectory is used. For the optical acquisition system, another Cartesian coordinate system is used, the origin and the basis vectors are defined by the equipment or the user.

The objective of the alignment is to find a transformation matrix $\underline{\underline{T}}$ to map the coordinates in one reference frame to the other one. If the relative position of the two systems is fixed, *i.e.* the optical and the CT scanners are connected rigidly, the alignment can be realized by pre-calibration. However, this solution is impractical due to the following issues:

- Radiation damage

  As most of the commercially available optical scanners are not designed to operation in the presence of X-ray radiation, there is often no shielding material to protect the sensitive components in the optical scanner. This prevents the optical scanner from being operated during the CT acquisition.

- Reconfiguration of the acquisition system

Provided the optical scanner is shielded, due to the difference in the source of contrast, the optimal scanning trajectory for a CT acquisition system and an optical acquisition system are often different. As a result, a constant reconfiguration of the setup is necessary. Performing calibration for each reconfiguration is time consuming. Thus, other approaches should be investigated.

- Project specific reason

  Within the framework of this dissertation, the optical scanning tasks are performed by collaborators from University of Heidelberg.

There are two general approaches that have been evaluated to align the datasets with completely different representations. The basic principle is to convert one representation, either the optical or CT reconstruction, to the other and calculate the transformation matrix using the same representation. Considering that complete tool chains exist to handle alignment tasks on same representations, a more straightforward implementation would be possible if the datasets are converted to the same representation. Which way to go? Converting 3d mesh from the optical scanner to volumetric representation or converting 3d volume to mesh?

The mesh is composed of vertices and edges connecting the vertices. From the working principle explained in subsection 2.2.1, a mesh represents a visible surface. In an ideal setting, the mesh forms a closed surface representing the interface between the material and air. Converting mesh data to volume data will result in a volumetric mask with the same size as the reconstruction. To align the volumes, a segmentation of the object from the supporting material is necessary. In addition, the features inside the object that are not visible to an

optical scanners need to be segmented and removed based on voxel values.

Converting volume data to mesh data and align between mesh files will result in almost the same issues as converting mesh data to volume data. One advantage is the smaller size of the mesh files. Therefore, for the alignment process, the volumetric representation is converted to mesh representation.

It has to be pointed out that the alignment task is performed by project collaborators. Only basic concepts and main procedures are briefly noted here for the purpose of completeness.

6.1.1 Extract isosurface

In this dissertation, the isosurface is represented by a polygonal mesh extracted from the volume by applying the marching cubes (MC) algorithm, described by Lorensen, *et. al.* [45]. The MC algorithm operates on cubes formed by connecting the centers of 8 neighboring voxels. The MC algorithm takes one parameter which is the threshold value used to decide boundaries. The voxel values of the 8 voxels are compared to the threshold. Depending on the result of the comparison, the cube is matched to one of the possible templates, some of which are illustrated in fig. 6.1 taken from the dissertation of Bayer [7]. The matching template inserts new vertices as part of the representation of the isosurface. After iterating over all the voxels, the vertices form watertight meshes representing the isosurfaces. There are many implementations of the MC algorithm available. In this dissertation, the implementation in Paraview [4] is utilized.

In fig. 6.2, a CT scan of a cylinder head is used to illustrate the result of isosurface extraction. One part of the dataset is represented by the isosurface with a gray texture. The other part of the dataset is rendered by coloring the

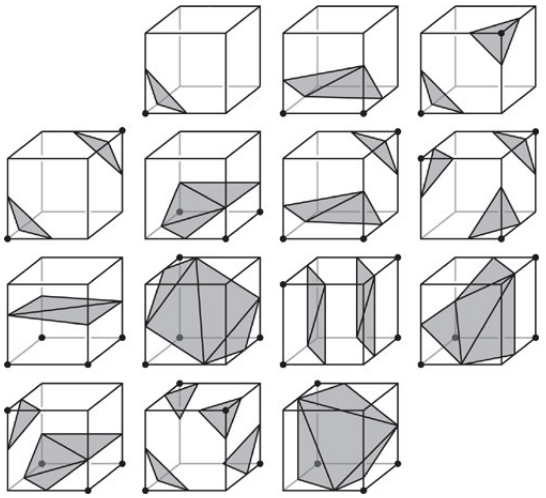

Figure 6.1: Some of the templates used in the MC algorithm.

voxels based on the voxel values according to a color map and a transparency setting. The threshold value used is marked on the color legend.

6.1.2 Reduction

The extracted isosurface contains internal structures that are not visible to an optical scanner as shown in fig. 6.2. Bayer *et. al* [9] has demonstrated that the internal features will cause bias in the following alignment process leading to a possible misalignment. A subset containing only the external vertices must be separated from the mesh extracted from the volumetric dataset. The *RanCEAF* algorithm developed by Bayer *et. al* [9] is used to extract a subset of vertices representing the visible surface of the object.

The RanCEAF algorithm selects vertices by querying the nearest neighbor

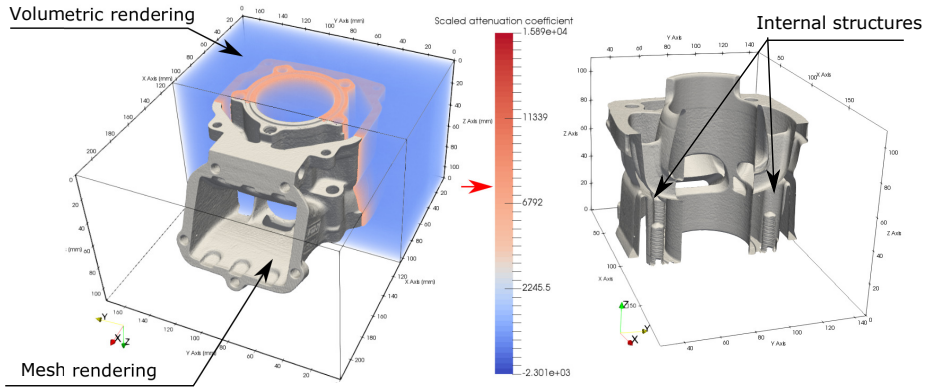

Figure 6.2: (a) shows the result of the isosurface extraction. Half of the volume is processed and the other half is rendered using volume rendering. (b) shows a clipped isosurface with internal structures marked.

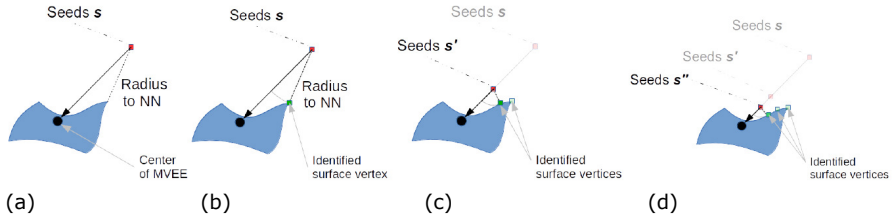

Figure 6.3: Illustration of the RanCEAF algorithm.

of shifted seed points. The seed points are initially selected from the $MVEE$ randomly. For each seed, the shifting direction is towards the center of the MVEE and the step size equals the distance from the seed to its NN. An illustration is taken from the dissertation of Bayer [7] to explain the shifting. The number of shifts is predefined. After a few shifts, the selected vertices produces a good representation of the external surface as illustrated by Bayer *et. al* [7] in fig. 6.4.

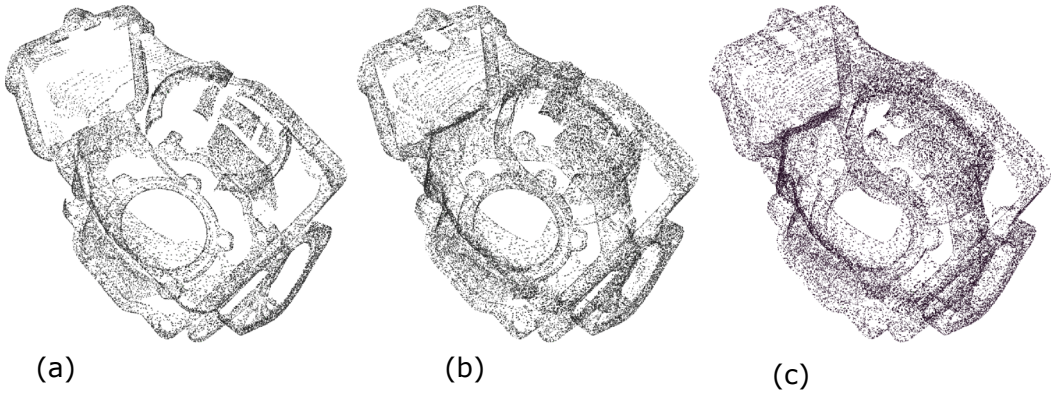

Figure 6.4: Result of the RanCEAF results with different parameters. (a) shows the result with no seed shift. (b) shows the result with 1 time seed shift. (c) shows the result with 2 times seed shift.

6.1.3 Iterative closest point algorithm

The alignment between the extracted mesh and the optical scan is accomplished by the iterative closest point (ICP) algorithm. The ICP algorithm minimize the root mean square error between two point clouds by applying a rotation and a translation operation to the points in one point cloud as described by

Besl *et. al.* [8]. However, the ICP algorithm does not guarantee the result reaches the global optimal result. Therefore, the implementation of ICP in MeshLab [24] requires a coarse manual alignment before the iteration starts. As the mesh from the optical scan often contains missing surfaces, an interesting question would be how much of the overlap between the extracted mesh and the mesh from optical scan needs to be to ensure the convergence of the alignment. Chetverikov *et. al* developed the trimmed iterative closest point algorithm [22], an extension of the ICP algorithm, to process datasets with overlaps under 50%. Thus, the mesh from the optical data should have 50% or more overlap with the surface of the object. In this dissertation, high quality optical data is acquired covering over 90% of the visible surfaces. Before running the ICP algorithm, a careful manual alignment is performed to prevent the optimization being trapped at local minimum.

6.2 Mask extraction

To fuse the optical data, the mesh representation is converted to a volumetric representation. The conversion is explained in this section. As the direct output of the optical scanner, the mesh represents the surface of the object. All the triangles formed by three vertices represent patches of the surface. Unlike the conversion from a volumetric representation to a mesh representation where watertight meshes are guaranteed, the conversion from the mesh representation has to process the defects in the mesh originating from the limitations of the optical surface scanner. The defects are referred as false negatives from the surface acquisition. Partial surface data with defects are the typical results from an optical scanner. In this section, the discussion focuses on different

approaches to handle complete surface data and partial surface data.

6.2.1 Ray clipping

The ray clipping method [7] calculates the coordinates of the intersection points when casting a ray from the X-ray source to the detector elements. As the surface orientation is one of the attributes stored in the mesh, the intersection points can be identified as entering or exiting the object when casting from the source. Thus, a segmentation of the object from the reconstruction volume is achieved by casting all possible rays in a scan. However, this approach is only applicable to complete surface data since partial surface data will lead to missing boundary points resulting in inconsistent segmentation result from different rays. In this dissertation, the volume clipping is applied.

6.2.2 Volume clipping

After the alignment using ICP, the mesh can be transformed into the coordinate system of the volume. To convert the mesh into a volumetric representation, each voxel in the reconstruction region is tested if it intersects with the mesh. According to the test result, a subset of the voxels are identified as boundary voxels $\underline{B}$.

$$B_i = [\underline{B}]_i = \begin{cases} 0, & if\ i \in \Omega_B \\ 1, & if\ i \notin \Omega_B \end{cases} \tag{6.1}$$

where Ω_B contains all the indices of voxels which intersect with a mesh $\mathcal{M}$.

In the case of complete surface data, all the voxels enclosed by the watertight mesh can be segmented from the whole volume and identified as part of the

object. A subset containing all the masked voxels is stored as $\underline{M}$.

$$M_i = [\underline{M}]_i = \begin{cases} 1, & if\ i \in \Omega_M \\ 0, & if\ i \notin \Omega_M \end{cases} \tag{6.2}$$

Where Ω_M is the set of voxel indices that are located inside of a watertight mesh $\mathcal{M}^{\mathrm{w}}$.

6.2.3 Measurements on the mask

Before the data fusion process, dimensional measures can be taken from the optical mesh and the extracted mesh. The distance between planes are taken as measures because they can be used to compare across different techniques. The measurement procedure on the mesh is described here.

The objective is to measure the distance between two planes. However, this objective is not well defined for planes that are not parallel. Considering the angle between the planes is small, the measurement is then converted to the measurement of the distance between a point in on plane to the other plane. This is achieved using by the following procedure:

- Selecting points in one plane

  Select more than 3 points that are well separated from one plane and record their coordinates as $\underline{d}_1, ..., \underline{d}_n, n > 3$

- Fit a plane to the extracted points

  The equation of a plane in $3D$ is

$$c_a d_x + c_b d_y + c_c = d_z, \tag{6.3}$$

where $\underline{d} = (d_x, d_y, d_z)^T$ and c_a, c_b and c_c are coefficients. With more than 3 points, the coefficients can be solved in a least square sense. The pseudo inverse is used to compute the coefficients.

- Select one point in the opposite plane

  Select one point from the other plane as $\underline{d}_0$. The distance D is calculated as

$$D = \frac{c_a d_{0x} + c_b d_{0y} - d_{0z} + c_c}{\sqrt{c_a^2 + c_b^2 + 1}} \tag{6.4}$$

6.3 Data fusion model

This section explains how data fusion can be achieved by reconstructing the object from the CT projection data using the optical mask as prior information. Two different models are developed to fuse either complete optical data or partial optical data with the CT scanning data. The first model assumes that complete surface data is available. The second model drops this assumption and accepts a broader range of optical data resulting in a practical model to fuse optical data.

6.3.1 Data fusion using the EM method

In eq. (4.12), the reconstruction aims to find the result which has the maximum likelihood with the given measurement without other prior information of the object. In this model, the reconstruction is formulated as an optimization problem, which takes the optical mask as prior information and to find the result with the maximum *a posteriori*. After applying the Bayesian rule:

$$P_{\underline{\mu}}(\underline{\hat{\mu}} \mid \underline{\hat{I}}) = \frac{P_{\underline{I}}(\underline{\hat{I}} \mid \underline{\hat{\mu}}) P_{\underline{\mu}}(\underline{\hat{\mu}})}{P_{\underline{I}}(\underline{\hat{I}})} \tag{6.5}$$

the objective function of the optimization becomes:

$$P_{\underline{\mu}}(\underline{\hat{\mu}} \mid \underline{\hat{I}}) = \frac{P_{\underline{\mu}}(\underline{\hat{\mu}})}{P_{\underline{I}}(\underline{\hat{I}})} \prod_{i=1}^{M} \frac{(I_{0i} e^{-[\underline{\underline{A}} \cdot \underline{\hat{\mu}}]_i})^{\hat{I}_i}}{\hat{I}_i!} e^{-I_{0i} e^{-[\underline{\underline{A}} \cdot \underline{\hat{\mu}}]_i}} \tag{6.6}$$

Assuming that the complete surface data is available and the mask eq. (6.2) generated from the optical scan segments the object and its surrounding empty space, the values of voxels outside the mask are set to zero. The values of the voxels inside the mask are unknown, therefore, an uniform distribution is applied. In the same equation, the probability $P_{\underline{I}}(\underline{\hat{I}})$ is not a function of the linear attenuation vector and it is treated as a constant. Following the same calculations as eq. (4.12) to eq. (4.15), the following iteration scheme is implemented:

$$\hat{\mu}_j^{(k+1)} = \hat{\mu}_j^{(k)} \frac{\sum_{i=1}^{M} I_{0i} e^{-[\underline{\underline{A}} \cdot \underline{\hat{\mu}}^{(k)}]_i} a_{ij}}{\sum_{i=1}^{M} \hat{I}_i a_{ij}}, j \in \underline{M}, \tag{6.7}$$

where k and $k+1$ are iteration numbers. The difference between eq. (6.7) and eq. (4.15) lies in the selection of voxels during the update. The mask extracted from the optical scan serves as labels to segment the volume into object and air. Only the voxels representing the object have a contribution to the projection; hence are updated in the reconstruction. In the implementation, the initial values are set to zero. In each iteration, $\sum_{i=1}^{M} I_{0i} e^{-[\underline{\underline{A}} \cdot \underline{\hat{\mu}}^{(k)}]_i} a_{ij}$ computes the forward projection image based on the current volume. The projection image is then divided by the projection image acquired from the experiment, $\sum_{i=1}^{M} \hat{I}_i a_{ij}$. The radio is utilized to update the current volume.

6.3.2 Data fusion model with partial surface data

The objective of this data fusion model is to fuse the features resolved by the optical scanners with the features resolved by a CT scanner. For simulation studies with numerical phantoms, the surface mesh represents the real surface of the sample without false negatives, *i.e.* holes. In this case, the surface mesh segments the volume into sample and air. The mask $\underline{M}$ is the set of all the voxels in the sample that contribute to the projection. The fusion can be implemented as an additional constraint in the reconstruction as

$$\underline{\mu} = \underset{\underline{\mu}}{argmin} \left\| \underline{\underline{A}} \cdot \underline{\underline{D}}_M \underline{\mu} - \underline{p} \right\|_2 \tag{6.8}$$

where $\underline{\underline{D}}_M = diag\{M_i\}$. The $\underline{\underline{D}}_M$ ensures that during each iteration only the voxels in the mask are updated. The aim of the multiplication with the system matrix $\underline{\underline{A}}$ is to project the current volume. The difference between the projection of the reconstructed volume and the measured projects is minimized. However, the effectiveness of this method requires the mesh to be watertight [26], *i.e.* containing no holes, and the sample to be the only object in the field of view, which, in practice, is often violated.The holes can be closed by simply analyzing the curvature of the neighboring triangles if the assumption of smooth surface mesh is true and the holes are relatively small, *i.e.* subdivision method. However, applying a patch at a hole to produce a watertight mesh is a risky operation. If there are protruding structures missing from the optical scanning, such patches will segment the image at the wrong location leaving a mask that is too tight for the object. As a result, all features outside the patch will be missing and the attenuation of the object will be overestimated. The surface mesh is a representation of the visible surface of the object which is

an interface between air and other material. For transmission measurement, such an interface indicates that the attenuation coefficients on both sides of the mesh are different. This creates a direct link between the surface mesh and the gradient image of the object. The boundary field $\underline{B}$ marks the exact locations where a non-zero gradient is expected. However, the value of the gradient is unknown because the attenuation coefficients are unknown before reconstruction. The gradient of real-world images, especially the gradient images of industrial images, are compressible as most of the elements in the gradient images are zero or close to zero. If using a gradient operator as the sparsifying operator ψ, in the compressive sensing framework, the reconstruction problem can be formulated as:

$$\underline{\mu} = \underset{\underline{\mu}}{argmin} \left\| \psi(\underline{\mu}) \right\|_1, \quad s.t. \quad \underline{\underline{A}} \cdot \underline{\mu} = \underline{p} \tag{6.9}$$

where ψ is some sparsifying operator, similar to the operator used by Chen *et. al.* [20], transforming the image to sparse representations. The $\ell 1$ norm in eq. (6.9) replaces the $\ell 0$ norm as a heuristic to encourage a sparse solution.

Since a subset of non-zero elements in these gradient images are tagged in $\underline{B}$, (eq. (6.9)) can be updated s.t. the gradients calculated at the boundaries tagged in $\underline{B}$ are preserved because they have a smaller weight in the cost function in Equation (eq. (6.9)).

$$\underline{\mu} = \underset{\underline{\mu}}{argmin} \left\| \underline{\underline{D}}_{\underline{B}} \psi(\underline{\mu}) + \alpha \overline{\underline{\underline{D}}}_{\underline{B}} \psi(\underline{\mu}) \right\|_1, \quad s.t. \quad \underline{\underline{A}} \cdot \underline{\mu} = \underline{p} \tag{6.10}$$

where $\underline{\underline{D}}_{\underline{B}} = diag\{B_i\}$ is a mask composed of all the boundary voxels extracted from the optical scan. $\overline{\underline{\underline{D}}}_{\underline{B}} = diag\{1 - B_i\}$ is the inverse mask and $\alpha \in [0, 1)$ is

a parameter to tune the strength of the mask.

6.3.3 Implementation

The constraint optimization problem in Equation (eq. (6.10)) can be transformed into an unconstrained optimization problem [58]:

$$\underline{\hat{\mu}} = \underset{\underline{\mu}}{argmin} \left\| \underline{\underline{A}} \cdot \underline{\mu} - \underline{p} \right\|_2^2 + c \left\| \underline{\underline{D}}_{\underline{B}} \psi(\underline{\mu}) + \alpha \overline{\underline{\underline{D}}}_{\underline{B}} \psi(\underline{\mu}) \right\|_1 \tag{6.11}$$

The parameter c balances the data fidelity and the regularization. To search for the minimizer $\underline{\hat{\mu}}$, the Alternating Direction Method of Multipliers ($ADMM$) [50] approach is employed. Using a similar notation, the unconstrained optimization is transformed to a constrained optimization problem with $K(\underline{\mu}, \underline{z})$ as the cost function:

$$\begin{cases} minimize\ K(\underline{\mu}, \underline{z}) = \left\| \underline{\underline{A}} \cdot \underline{\mu} - \underline{p} \right\|_2^2 + c \left\| \underline{\underline{D}}_{\underline{B}} \underline{z} + \alpha \overline{\underline{\underline{D}}}_{\underline{B}} \underline{z} \right\|_1 \\ subject\ to\ \underline{z} = \psi(\underline{x}) \end{cases} \tag{6.12}$$

This optimization is solved using the Lagrange method. The Lagrange multiplier is l, and relaxation variable is $\underline{d}$. The variables will be updated alternatively in each iteration.

$$\begin{cases} \underline{\mu}_{k+1} = \underset{\underline{\mu}}{argmin} \left\| \underline{\underline{A}} \cdot \underline{\mu} - \underline{p} \right\|_2^2 + l \left\| \psi(\underline{\mu}) - \underline{z}_k - \underline{d}_k \right\|_2^2 \\ \underline{z}_{k+1} = \underset{\underline{z}}{argmin}\ c \left\| \underline{\underline{D}}_{\underline{B}} \underline{z} + \alpha \overline{\underline{\underline{D}}}_{\underline{B}} \underline{z} \right\|_1 + l \left\| \psi(\underline{\mu}) - \underline{z} - \underline{d}_k \right\|_2^2 \\ \underline{d}_{k+1} = \underline{d}_k - (\psi(\underline{\mu}) - \underline{z}_k) \end{cases} \tag{6.13}$$

By converting the optimization into sub-problems, the computation is

simplified. A combination of efficient least-square algorithm and soft-thresholding can be applied to solve the optimization problem.

To minimize $\underline{\mu}_{k+1}$, the gradient of its cost function is set to zero and solve it with a conjugate gradient(CG) method. The minimizer $\underline{z}_{k+1}$ is achieved by applying a soft thresholding operation at level $\alpha \times \frac{c}{2l}$ (*line* 16 in *Algorithm* 6)on all the voxels which are tagged in $\underline{B}$ and at level $\frac{c}{2l}$ for all the other voxels. The initial value of $\underline{\mu}$ can be set to zero or to a masked backprojection. The use of a masked backprojection as the initial image often results in a faster convergence, but it may trap the search algorithm at a local minimum. In the following, the initial image is set to zero. The reconstruction work flow is summarized in *Algorithm* 6.

6.4 Simulation

The two models, which take complete surface data and partial surface data respectively, are tested with synthetic data to study their characteristics. The simulations focus on the application in limited-angle scans following a partial circular scan. In the simulation study of the data fusion model with EM estimation, two experiments with different angular sampling rates are performed to study the performance of the model under sparse sampling conditions. In the simulation study of the data fusion model taking partial optical data, the simulation is set to test the stability of the model.

6.4.1 Complete optical data

A virtual cone beam CT setup is used in the simulation fig. 6.5. The X-ray source has an ideal point-like focal spot and the photons generated from the

Algorithm 6 Reconstruction with boundary information

procedure RECONSTRUCTION WITH PARTIAL OPTICAL DATA
  $\underline{\mu}_0 = \underline{0}$, $\underline{d}_0 = \underline{0}$ // Initialization
  for $k = 1, ..., k_{max}$ **do**
    $\underline{\mu}_k = \underline{\mu}_{k-1}$
    //Prepare the linear system to be solved by CG
    $A_{CG} = \underline{\underline{A}}^T \underline{\underline{A}} + l\psi^T\psi$, $\underline{b} = \underline{\underline{A}}^T \underline{p} + l\psi^T(\underline{z}_k + \underline{d}_k)$
    //Calculate the residual and the normalization
    $\underline{r} = \underline{b} - \underline{\underline{A}}_{CG} \cdot \underline{\mu}_k$, $\underline{q} = \underline{r}$, $\rho = \underline{r}^T\underline{r}$
    for $i = 1, ..., n_{CG}$ **do**
      $\underline{t} = \underline{\underline{A}}_{CG}\underline{q}$
      $a = \frac{\rho}{\underline{q}^T\underline{t}}$ // Calculate conjugate vector coefficient
      $\underline{r} = \underline{r} - a\underline{t}$
      $\underline{\mu}_k = \underline{\mu}_k + a\underline{q}$ //Update
      $\rho_s = \rho$
      $\rho = \underline{r}^T\underline{r}$
      $\underline{p} = \underline{r} + \frac{\rho}{\rho_s}\underline{p}$ // Calculate next conjugate vector
    end for
    $\underline{z}_k = max(\left\|\psi\underline{\mu}_k - \underline{d}_{k-1}\right\| - \frac{c}{2l}(\underline{\underline{D}}_{\underline{B}} + \alpha\overline{\underline{\underline{D}}_{\underline{B}}})sign(\psi\underline{x}_k - \underline{d}_{k-1})$
    $\underline{d}_k = \underline{d}_{k-1} - \psi\underline{\mu}_k + \underline{z}_k$
  end for
  Return $\underline{\mu}_k$
end procedure

source are assumed to be monochromatic. A flat panel detector is used and aligned with the X-ray source, *i.e.* perfect alignment. The *sdd* is 1000 mm and the *sid* is 500 mm. In this experiment, limited-angle circular trajectory specified in eq. (6.14) is used during the acquisition to generate limited angle scan data.

$$\{\underline{\underline{T}}(-\theta_1),\ \underline{\underline{T}}(-\theta_1 + \Delta\theta),\ ...,\ \underline{\underline{T}}(\theta_2)\} \tag{6.14}$$

where $\theta_1, \theta_2 \in (0, \pi/2)$.

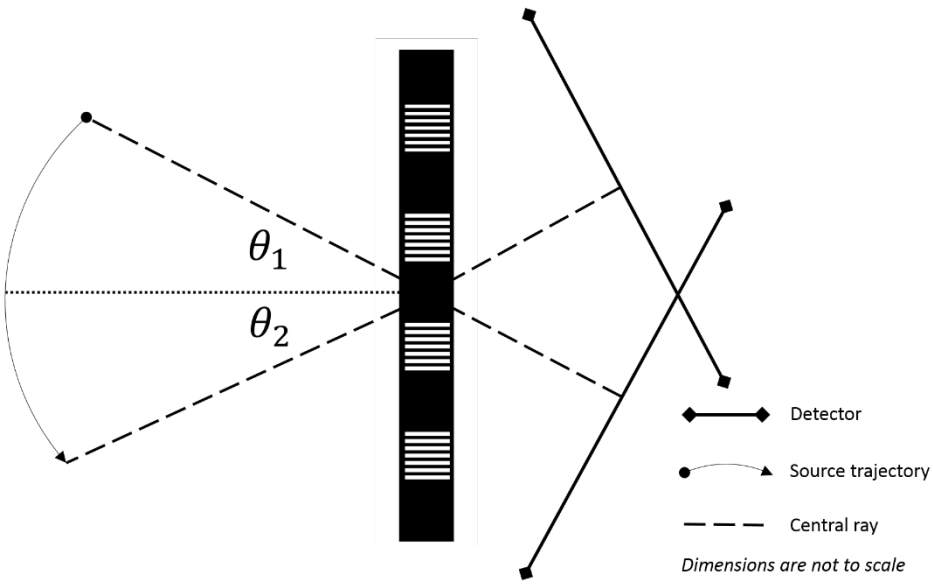

Figure 6.5: The schematic of the virtual CT setup used in the simulation. The source is aligned to the detector such that the central ray from the source is always perpendicular to the detector. The relative position of the source with respect to the detector is fixed during the scan. The object is placed between the source and detector. The relative position of the source with respect to the object forms the source trajectory. In the experiments, the angle range is always from θ_1 to θ_2.

The synthetic phantom used in this simulation study has features to test the contrast at a given spatial resolution and uniformity of the reconstruction. A cross-section of the phantom perpendicular to the rotation axis is illustrated in fig. 6.6(a). The Phantom is placed in the described CT system with its geometric center overlapping with the isocenter, *i,e,* the intersecting point of the central ray and the rotation axis. The surface data in the experiment is the outer boundary of the phantom in fig. 6.6(a).

In the first simulation, the angle range during the acquisition is limited to 60 degree with an increment of 1 degree, which is referred to a fine scan in this experiment. The acquisition result is the input of the reconstruction program. To illustrate the improvement by incorporating surface information, the reconstruction is carried out with and without surface information and for each case the reconstruction is stopped after 500 iterations. In a second simulation, the scan angle increment is set to 6 degree, which is denoted as a few-view scan. The same reconstructions are carried out for the few-view data set.

The central slice of the phantom and the central slices of the reconstruction results are illustrated in fig. 6.6. The results shown in fig. 6.6(b) and fig. 6.6(d) are calculated without surface information. The projection values are backprojected to the outside of the object leading to unrecognizable boundaries and non-uniform reconstruction of the object. To describe the uniformity of the reconstruction, the standard deviation of the pixel values in area 1 as indicated in fig. 6.6(a) is calculated for each of the reconstructed images. The results are shown in tab. 6.1. The reconstruction of the parallel structures in the phantom is also affected by the limited scan angle and the number of projections. fig. 6.6(d) shows the reconstruction of the phantom without surface data under

the constraint of limited scan angle and limited number of projections. Denote the parallel structures in the phantom as a square wave, then the square wave response of the reconstruction is not homogeneous resulting in reduced capability to differentiate materials. To assess the homogeneity, the contrast of the structures in area 2 as illustrated in fig. 6.6(a) is calculated for all the reconstructed images and the standard deviation of the contrast within area 2 for each reconstruction is selected as a measure of the homogeneity. The contrast is calculated as

$$c = \frac{v_{max}^{local} - v_{min}^{local}}{v_{max}^{global} + v_{min}^{global}} \tag{6.15}$$

Where v_{max}^{global} is the maximum pixel value in area 2, and v_{max}^{local} indicates the maximum pixel value at a local area. The same rule applies to the minimum values. The mean value of the contrasts at different locations within the area is plotted in fig. 6.7 with the standard deviation shown as error bars. The contrast values at the end of the iterations are listed in tab. 6.2.

6.4.2 Partial optical data

The performance of the model with partial optical data is demonstrated using two simulations with synthetic phantom. The phantom has protruding and

	Without surface data		With surface data		Improvement	
	MSE	*std.*	MSE	*std.*	MSE	*std.*
Fine scan	0.077	0.2772	0.056	0.2362	27.27%	14.79%
Few-view	0.0516	0.2208	0.0382	0.1955	25.97%	11.46%

Table 6.1: The analysis of pixel values in area 1 after 500 iterations. The mean square error (MSE) between the reconstructed images and the phantom is calculated. The standard deviation of the reconstructed value is also calculated to quantify the uniformity of the reconstruction.

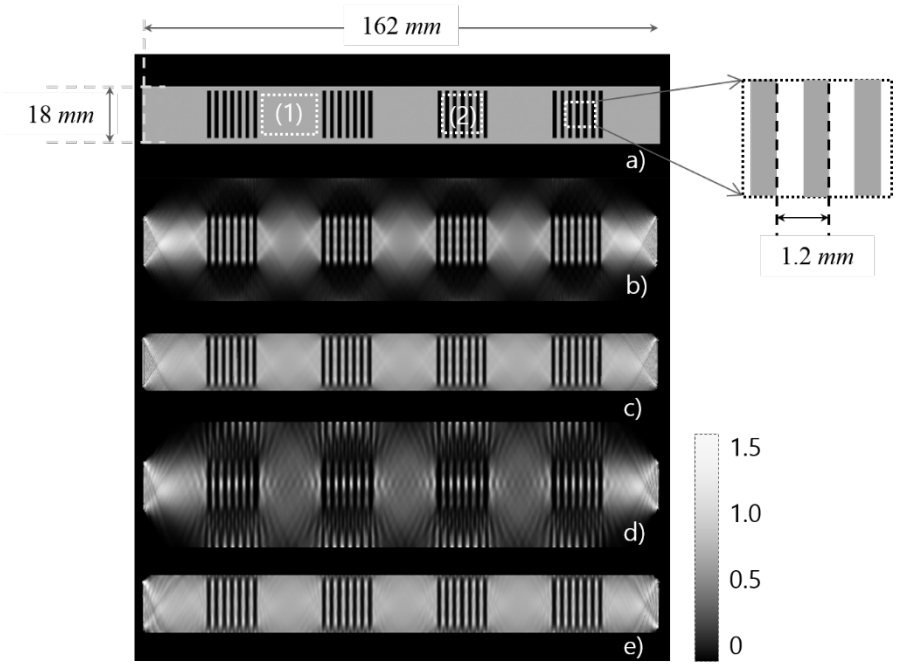

Figure 6.6: a) illustrates the central slice of the phantom used in the simulations. This slice is composed of uniform areas and areas with homogeneous parallel planes. The same structure repeats in the third dimension. Among the uniform areas and homogeneous areas, two of them, highlighted as area 1 and area 2 are selected for further quantitative analysis; b) shows the reconstruction from a fine scan without using surface data; c) shows the reconstruction from a fine scan with complementary surface information; d) shows the reconstruction from a few-view scan without using surface data; e) shows the reconstruction from a few-view scan with full surface information. The relative attenuation coefficient is indicated by the scale bar.

	Without surface data		With surface data		Improvement	
	MSE	*std.*	MSE	*std.*	MSE	*std.*
Fine scan	0.9181	0.037	0.9402	0.0189	2.41%	48.92%
Few-view	0.609	0.2193	0.8874	0.0283	45.71%	87.10%

Table 6.2: The analysis of pixel values in area 2 after 500 iterations. The mean value of the local contrast values and the standard deviation of the local contrast values are shown in this table as a measure of the homogeneousness of the square wave response.

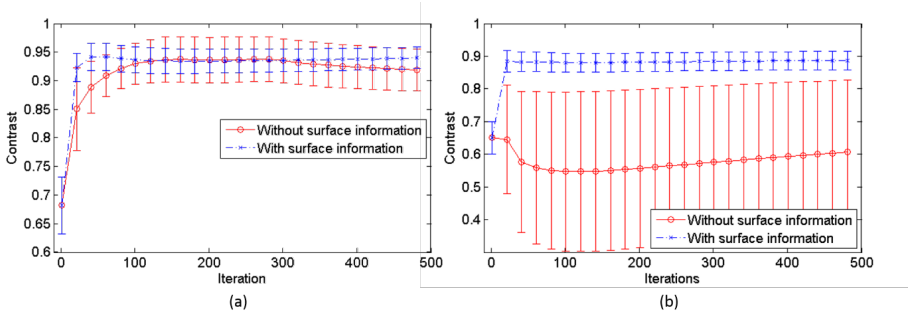

Figure 6.7: a) shows a contrast assessment of the reconstruction from fine scan data. The traces show the mean value of the local contrast values with the standard deviation of the contrast values plotted as error bars. The data points represented by circles are from reconstructions without full surface data and the points shown as crosses are from reconstructions with full surface data; the data in b) is calculated from few-view data.

concave surface structures and cascade circles as internal structures. The cross section of the sample is illustrated in fig. 6.8, the same structure repeats in the direction of the y axis, *i.e.* the rotation axis. The boundary voxels are known from the numerical phantom. The full set of boundary pixels is used as a perfect representation of the surface while a subset without all protruding and concave structures is used as a simulated boundary derived from a defective optical surface measurement (fig. 6.8(b)). The material of the sample is assumed to be aluminum and the photons are assumed to be monochromatic with an equivalent energy of 100keV. Simulated Poisson noise was added to the projection assuming a total of 1 million photons per detector element during the exposure.

To demonstrate the improvement from fusing prior information with CT projection data, the same set of limited-angle projections were reconstructed using the model presented in subsection 6.3.2 with complete or incomplete boundary as prior and with zero prior information. The model parameters are set as c=1.0 and l=10 while the number of CG iteration is set to 5. The parameters are selected empirically. At the end of each iteration, the mean square error of the projections (MSE_{proj}) is calculated and the reconstructed volume (MSE_{recon}) as the phantom is known. In addition, the structure similarity index (SSIM) [70] of the cross-section is calculated. The SSIM is a patch-based algorithm for evaluating the image quality over the whole image. For patches, $\underline{x}$ and $\underline{y}$, of the same size, the SSIM is computed as

$$\frac{(2m_{\underline{x}}m_{\underline{y}} + c_1)(2\sigma_{\underline{x}\underline{y}})}{(m_{\underline{x}}^2 + m_{\underline{y}}^2 + c_1)(\sigma_{\underline{x}}^2 + \sigma_{\underline{y}}^2 + c_2)}, \tag{6.16}$$

where $m_{\underline{x}}$ is the average of $\underline{x}$, $m_{\underline{y}}$ is the average of $\underline{y}$, $\sigma_{\underline{x}\underline{y}}$ is the covariance of $\underline{x}$ and $\underline{y}$, $\sigma_{\underline{x}}^2$ is the variance of $\underline{x}$, $\sigma_{\underline{y}}^2$ is the variance of $\underline{y}$, $c_1 = (k_1 L)^2$, $c_2 = (k_2 L)^2$,

$k_1 = 0.01$, $k_2 = 0.03$ and L is the dynamic range of the image.

The structural component of the SSIM for patches $\underline{x}$ and $\underline{y}$, is particularly important because correctly reconstructed structure is essential for segmentation tasks.

$$\frac{\sigma_{\underline{x}\underline{y}} + c_3}{\sigma_{\underline{x}}\sigma_{\underline{y}} + c_3}, \tag{6.17}$$

where $c_3 = c_2/2$.

The MSE_{recon} and the SSIM of the cross-section extracted from the reconstruction with zero prior , incomplete boundary and complete boundary are plotted in fig. 6.9, fig. 6.10 and fig. 6.11 respectively. The MSE_{proj} dropped quickly after a few iterations before it started to slightly increase due to the regularization, while the MSE_{recon} decreases with the iteration. However, the reconstructions were stopped after 1000 iterations before the sequence of the reconstructed volumes converges. As the task is to mitigate the limited-angle artifact, primarily the blurred boundaries which are not parallel to any rays during the acquisition, the structural similarity is of more interest. The structural component of the SSIM has reached its maximum at 0.9686 for zero prior, 0.9770 for incomplete boundary and 0.9891 for complete boundary after 1000 iterations which justifies the early stopping of the algorithm. The increase of SSIM is in line with the successfully reconstructed boundaries which are parallel to z axis in fig. 6.12(a, c).

While the exterior surface of the sample benefits directly from the fusion of surface data, the improvement in the reconstruction of internal features is investigated. The modulation transfer function (MTF) [11] is calculated with the help of the test structures inside of the phantom as a measure of spatial resolution. Although the MTF is non-stationary in limited-angle CT [33] and

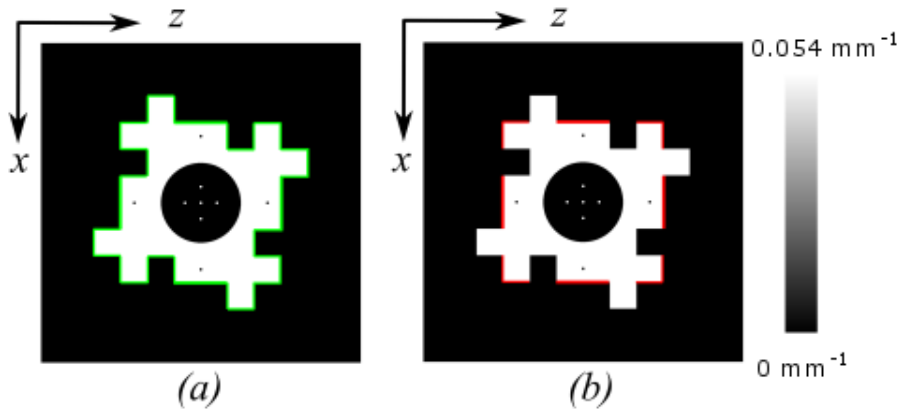

Figure 6.8: The cross section of the simulated phantom. The attenuation coefficients are linearly represented as gray levels. 0 is mapped to black and 0.054 $[mm^{-1}]$ is mapped to white, *i.e.* window = [0, 0.054].The same structure repeats in y direction. In the simulation, this cross section is aligned to the trajectory plane. In (a), all the boundaries visible to the outside are highlighted in green and will be used as perfect boundary in the simulations, while in (b) only part of the boundaries are highlighted in red and they will be employed as defective boundary to simulate real-world surface scanning results with holes.

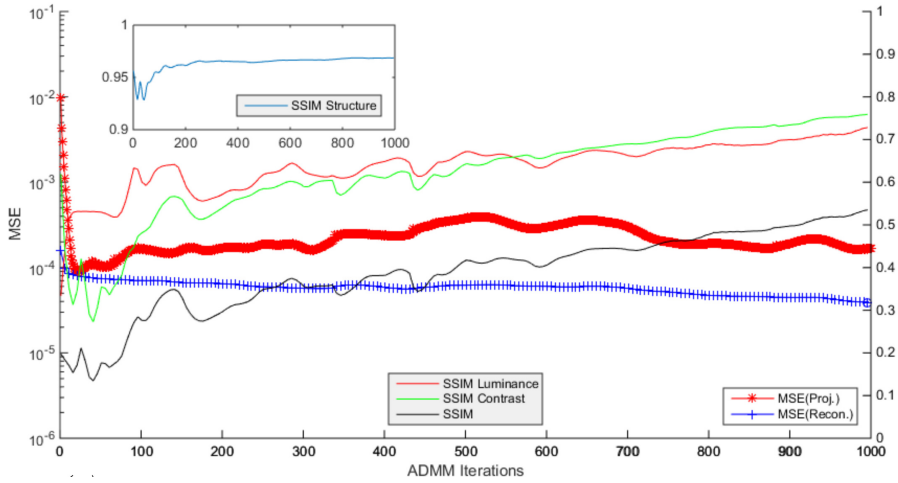

Figure 6.9: Results from the simulation with zero prior information. The MSE_{proj} and the MSE_{recon} as well as all the SSIM components from the reconstructions using proposed Algorithm 6 with zero prior information are plotted. All traces share the same horizontal axis which indicates the number of iterations, while the MSEs are plotted against the primary vertical axis on the left and the SIMM and its components apart from the structural component are plotted against the secondary vertical axis. The insets show the structural components of the SSIM.

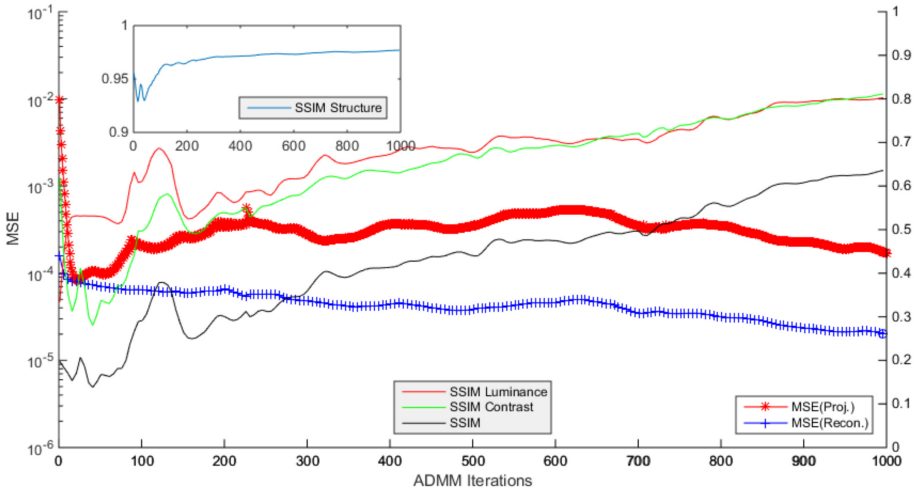

Figure 6.10: Results from the simulation with defective boundary as prior information. The MSE_{proj} and the MSE_{recon} as well as all the SSIM components from the reconstructions using proposed Algorithm 6 with defective boundary are plotted. All traces share the same horizontal axis which indicates the number of iterations, while the MSEs are plotted against the primary vertical axis on the left and the SIMM and its components apart from the structural component are plotted against the secondary vertical axis. The insets show the structural components of the SSIM.

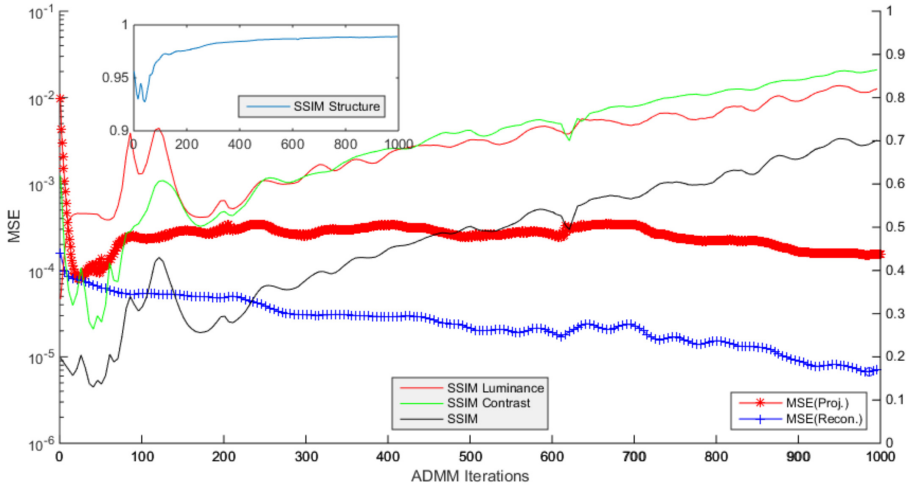

Figure 6.11: Results from the simulation with perfect boundary as prior information. The MSE_{proj} and the MSE_{recon} as well as all the SSIM components from the reconstructions using proposed Algorithm 6 with perfect boundary are plotted. All traces share the same horizontal axis which indicates the number of iterations, while the MSEs are plotted against the primary vertical axis on the left and the SIMM and its components apart from the structural component are plotted against the secondary vertical axis. The insets show the structural components of the SSIM.

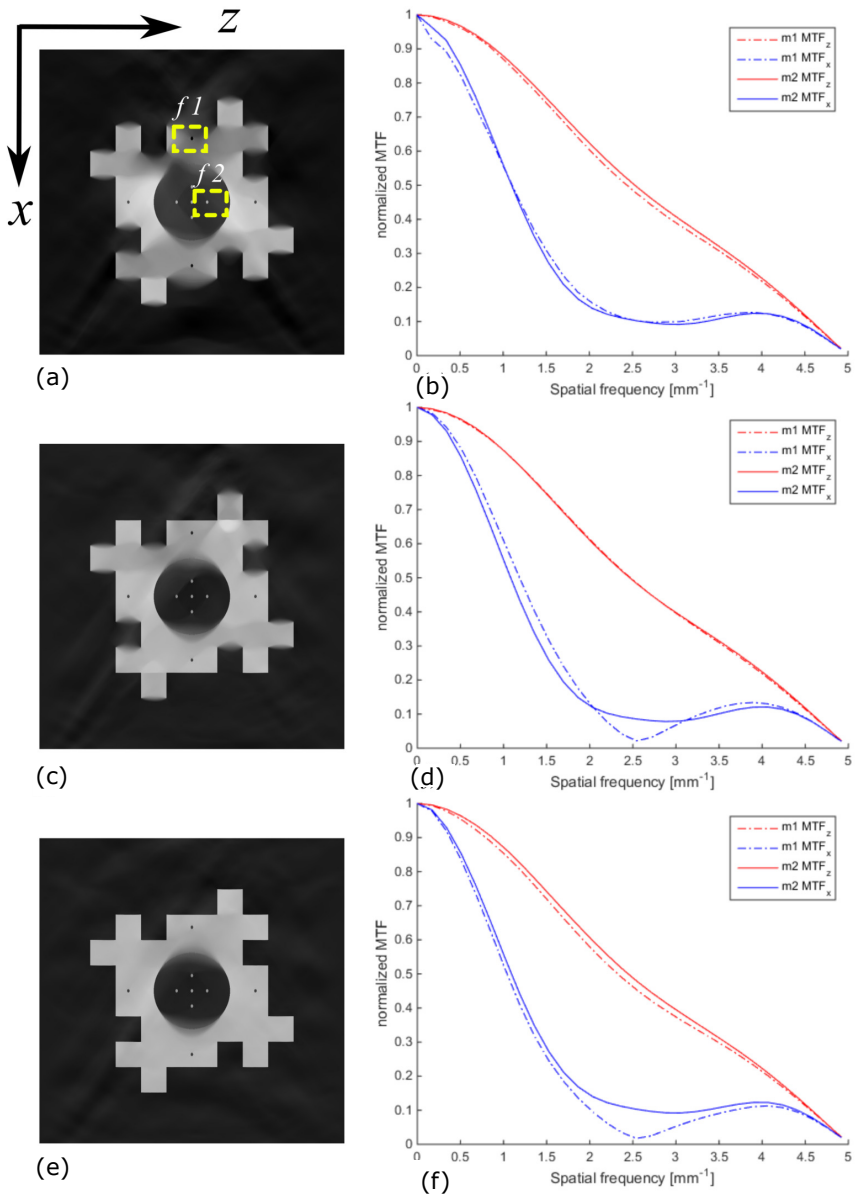

Figure 6.12: Results from the simulation study. The cross section images of the reconstructed volume taken from the trajectory plane are shown in (a,c,e). The gray level map window is [-0.01, 0.06]. The two features used for detailed analysis are indicated in (b) as $f1$ and $f2$. The MTF measured along horizontal direction and vertical direction at $f1$ and $f2$ are illustrated in (b,d,f).

even the local stationary assumption is inaccurate, the MTF is calculated in a standard and consistent procedure across the three images for comparison purposes. The edge spread function is extracted along the x and z direction at the test structures marked as $f1$ and $f2$ in fig. 6.12(a). The MTF is derived and shown in fig. 6.12(b, d, f). The measurement indicates that the spatial resolution along z direction is higher than the resolution along x direction, which is explained by the limited scanning angle. Another observation is that the local MTF inside the phantom doesn't change if boundary information is provided to the reconstruction, which is an expected result as there is no additional information regarding the internal structures provided to the reconstruction. However, other improvements on internal features are noticeable, such as the uniformity of the image and the contrast at the test structures. To describe the property, the contrast to noise ratio (CNR)

$$\frac{\|\mu_f - \mu_b\|}{\sigma_b} \tag{6.18}$$

where μ_f is the mean value of the feature, μ_b is the mean value of the background and σ_b is the standard deviation of the background, is calculated at the test structures. The results are listed in tab. 6.3. The CNR at the test structures is significantly improved because of the better estimation of the pixel values inside the object as a result of additional surface information.

In the second simulation, the phantom is a cuboid placed in the center of the CT system and is aligned to the detector such that the top and the bottom face of the cuboid are parallel to the trajectory plane. This is a typical scenario where severe cone beam artifacts arise at the top and bottom faces. The cone angle of the beam in this experiment is 20 degree and the scanning angle is 360

Feature	Zero prior	Defective mesh	Perfect mesh
f1	5.72	33.95	16.97
f2	24.52	35.51	71.47

Table 6.3: Contrast to noise ratio at $f1$ and $f2$ in fig. 6.8 after reconstruction with zero prior information, defective mesh and perfect mesh.

degree, *i.e.* a full circle trajectory, as the focus is on the cone beam artifact in this case. a Poisson noise level, which is equivalent to 1 million photons per detector element, is added to the simulated projection data. The phantom is then reconstructed with the standard FDK algorithm (fig. 6.13(a)) and the proposed algorithm incorporating surface data (fig. 6.13(b)). The formerly blurred top and bottom faces due to cone beam artifact are restored by the fusion of surface data. Although it is not justifiable to claim an increased spatial resolution in y direction, the reconstruction of the top and bottom surfaces is crucial when segmenting the object and supporting materials in experiments. Besides the reduction of cone beam artifact, the reconstruction also benefits from the iteration to gain a much more accurate and precise voxel value as illustrated in fig. 6.13(b).

6.5 Experiments

6.5.1 Experimental study

To validate the model and simulation and to prove the feasibility in practical applications, the model is applied to experimental data and solved using Algorithm 6. The sample used in the experiment is an aluminum cuboid with drilling holes and trenches on the surface. The sample was scanned with a micro

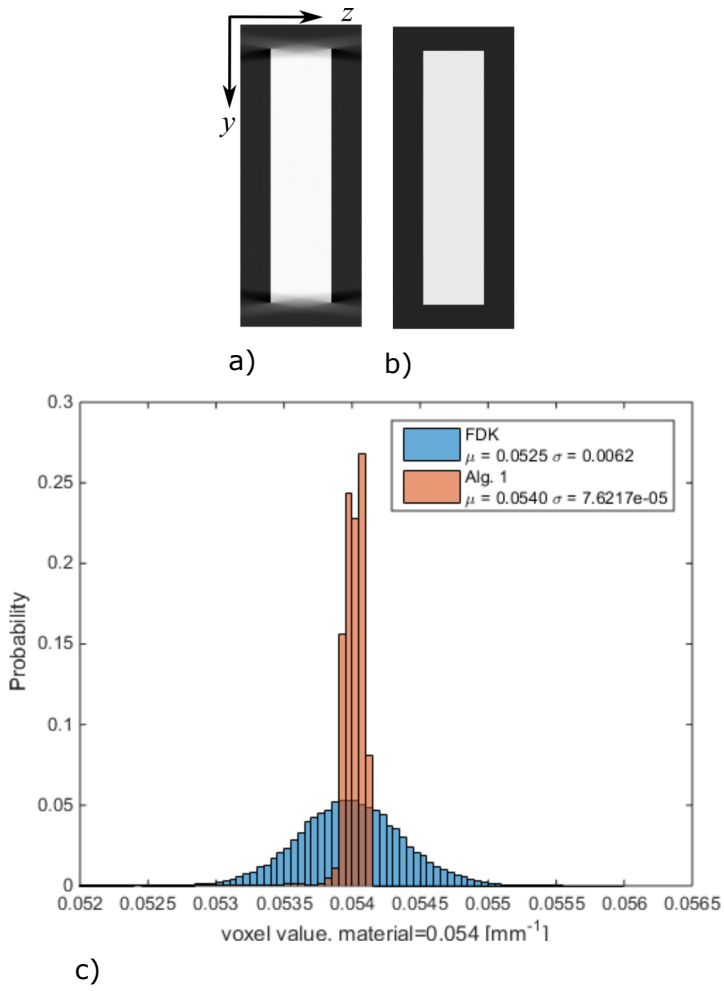

Figure 6.13: Comparison of cone beam artifact between FDK and the proposed algorithm. The cross section from the $y - z$ plane from the FDK reconstruction is shown in (a), while the same cross section from the reconstruction with surface data is shown in (b). The histogram (normalized with probability) of all the pixel in the object for both cross section images is shown in (c). The gray value distributions are fitted against Gaussian distributions and the results are indicated in the legend of (c).

CT system and a full circular trajectory. The scanning parameters are listed in tab. 6.4.

The FDK reconstruction from the full-angle projections was segmented to extract the object surface which was then used for alignment with the optical scanning result. The optical scanner generated a mesh representation $\mathcal{M}$ of the sample's surface. Due to known limitations, most of the deep trenches and holes cannot be acquired, as shown in fig. 6.14(d). The aligned mesh was rasterized to generate the boundary voxel map $\underline{B}$ for the reconstruction. A subset of the projection data, containing only projections taken in a 60 degree interval with a fixed angular increment, was extracted as an input to a limited-angle reconstruction. Two reconstructions were carried out using Algorithm 6 with and without surface data. Both reconstructions used the zero image as initial image and executed 500 iterations. The results are shown in fig. 6.14. The cross-sectional images of the reconstructed volumes along different directions are plotted into three groups for comparison. fig. 6.14(a) and (b) show the cross section with normal direction along the central beam. The most noticeable improvement is the reduction of cone beam artifact at the top and bottom of the image, which is important in order to separate the object from the supporting stage. Limited-angle artifact is not prominent in fig. 6.14(a, b). On contrary, the cross sections along the other two directions fig. 6.14(c, e) are distorted by the limited-angle artifact. As a result, all surfaces with normal direction along the beam direction are blurred. Due to the lack of boundary information, the reconstruction algorithm cannot stop the smearing of the voxel value across the object boundary, which is an empirical explanation of the blurring. It is shown that, after fusing the optical data and CT projection using Algorithm 6, the information acquired by both techniques is combined successfully. Features

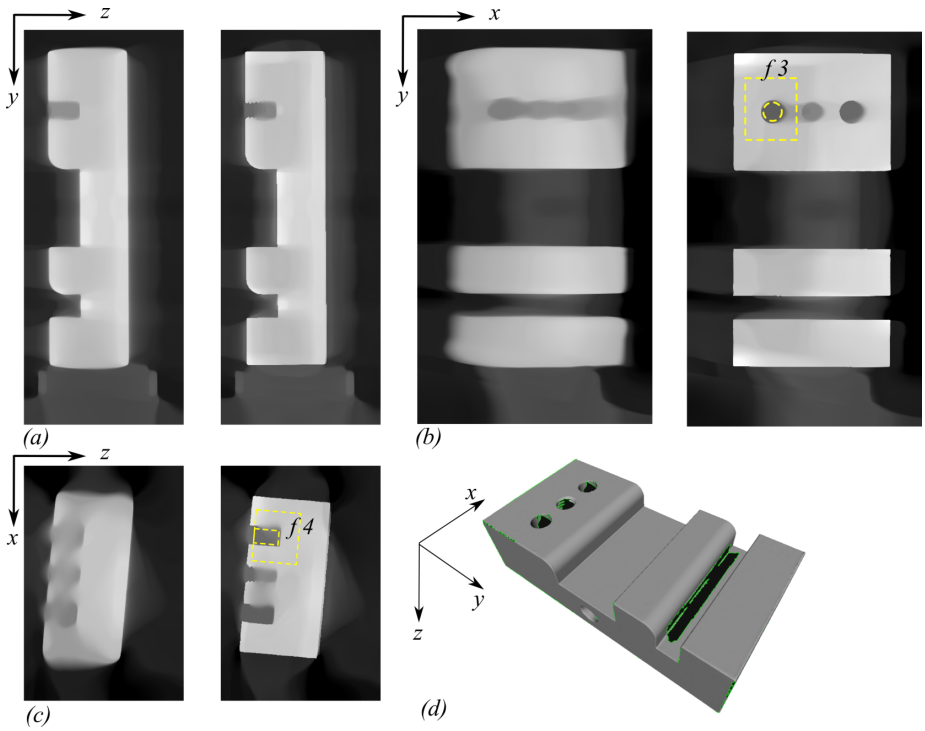

Figure 6.14: The cross sections from $y-z$, $x-y$ and $x-z$ planes are shown in pairs in (a)(b)(c). The reconstruction without optical scan, *i.e.* zero prior, is always placed on the left while the reconstruction with optical data, *i.e.* defective boundary, on the right. The features ($f3$ and $f4$) are highlighted in (b) and (c). The gray level window is [-0.01, 0.09]. The mesh from the optical scan is rendered in (d). Due to the limitations of optical scanning, the structures in the holes and part of the trench are not resolved and shown as holes in (d).

that were previously only available in one dataset are linked allowing more metrological tasks of the object. Unlike the simulation studies, a distortion-free and noise-free phantom is not available, rendering the full-reference metrics, such as SSIM and MSE, impossible to calculate. The CNR in the cross-section images is used as quantitative measure of the image quality. The feature selected in this study is a drilling hole in the object of fig. 6.14(b), where optical data and CT data are partially available. The results are in line with the visual inspection and listed in tab. 6.5.

Parameter	Value
Source detector distance	1020.2 [mm]
Source object distance	235.8 [mm]
Source voltage	160.0 [kV]
Source current	60.0 [μA]
Source target material	Tungsten(W)
Scintillation material	CsI
Exposure time	1.0 [s]
Averaging	3 (frames)
Binning factor	2x
Angular step	1.0 [deg]
Reconstruction volume dimension	$340 \times 840 \times 500$ (voxels)
Voxel pitch size	$0.12 \times 0.12 \times 0.12$ [mm]

Table 6.4: Experiment parameters

Feature	Zero prior	Optical scan
f3	2.42	25.07
f4	4.03	46.27

Table 6.5: Contrast to noise ratio at $f3$ and $f4$ in fig. 6.12(a) after reconstruction with zero prior, defective mesh from an optical scan.

6.6 Results and analysis

Two data fusion models are presented to cooperate optical scanning data with transmission X-ray data to mitigate artifacts in CT scans.

The first model requires the availability of the complete surface data. A mask segmenting the object is extracted from the optical data to limited the spatial support of the object. An MLEM algorithm is developed to incorporate the mask with the CT data. From the simulation study with a synthetic phantom, the limited-angle reconstruction with surface data leads to a better reconstruction of uniform areas and better resolved parallel structures. Quantitatively, the reconstruction of the uniform area with surface data achieved at least a 20% decrease in MSE and a 10% improvement in uniformity while the homogeneity for parallel structures is improved by 80% in the few-view configuration.

In contrast to the first model, the second model drops the assumption of complete surface data and accepts defective meshes from real-world optical scans, allowing day-to-day practical use in production. The fusion of surface information gives an increase of image quality of the reconstruction, namely the contrast to noise ratio shown in tab. 6.5 which is important for non-destructive testing, and mitigates the cone beam and limited-angle artifacts. The fused volume combines features resolved by both imaging techniques allowing various geometric measurements which are not possible with individual modalities. At the same time, it has to be pointed out that the additional surface information will not lead to extra resolving capability of internal features.

To quantitatively study the possibility to use the fusion result for geometric measurements, an image processing procedure simulating the CMM

measurements is implemented. The simulated CMM procedures are applied to extract thicknesses of the test sample at selected locations. In the procedures, instead of applying a global threshold to segment the material from air, local segmentation methods are applied at preselected points to extract local surface points and surface normal vectors. A plane is then fit to the extracted local surface points. To represent the surface extracted locally, the normal vector is calculated. The range of the distance from the fitting points to the surface along the normal vector is defined as the flatness of the surface. A small value in flatness indicates a flat surface.

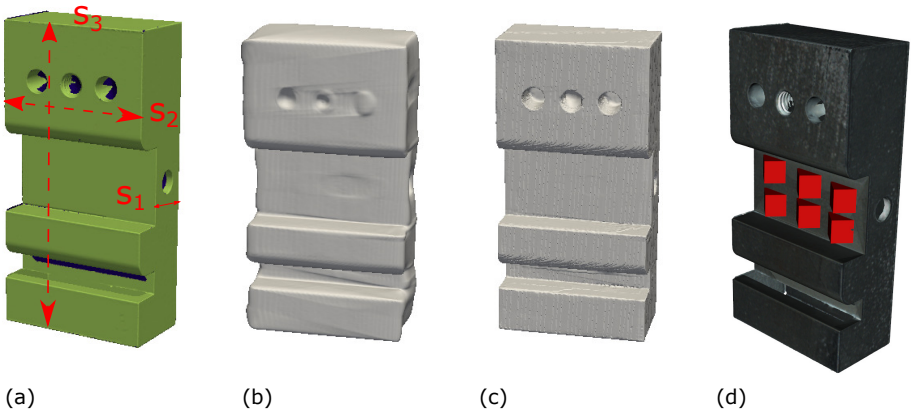

Figure 6.15: (a) mesh representation of the surface of the sample acquired by an optical scanner. The surface at the bottom of the drilling holes and trenches is missing due to the limitation of the optical scanner. The surfaces used in further analysis are labeled as S_1, S_2, S_3; (b) surface extracted from a limited-angle CT scan; (c) surface extracted from the fusion of CT and optical data; (d) optical scan with texture. The red cubes indicate the subset chosen for local surface extraction during the simulation of the CMM procedure.

The simulated CMM is applied to the result from the experimental study detailed in this chapter. The optical surface without texture, the CT

reconstruction without fusing optical data and the data fusion results are illustrated in fig. 6.15(a)(b)(c) respectively. Due to limited accessibility, the surfaces at the bottom of the holes and trenches are missing and are represented as black in fig. 6.15(a). The three surfaces denoted as S_1, S_2, S_3 are marked in fig. 6.15(a). The distances defined by the surfaces on both ends of the sample are marked by dashed lines with arrow ends. The reconstruction results are represented as iso-surfaces after applying global thresholding on the volumetric data. In fig. 6.15(b), the distortion of the surface S_2, as defined in fig. 6.15(a) is caused by the limited scanning angle and the distortion of surface S_3 results from the cone-beam artifact.

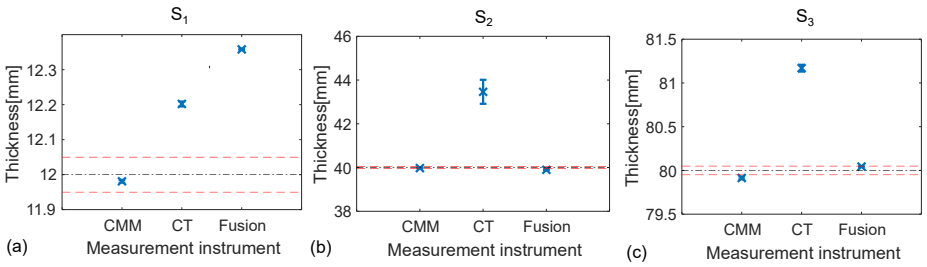

Figure 6.16: The measurement results of S_1, S_2, S_3 are plotted in (a)(b)(c) respectively. In each plot, the center horizontal dash-dot line indicates the design value and the other two horizontal dot lines indicate the upper and lower limit of the manufacturing tolerance. The thickness measured by the instruments are plotted as data points. The surface flatness extracted from the measurements are plotted as error bars.

6 subsets are selected for the measurements of each surface. fig. 6.15(d) illustrates the subsets selected to extract the surface properties of S_1 as an example. The thickness between surfaces S_1, S_2, S_3 and their opposite surfaces are estimated and compared between the reconstructed datasets with and without fusing prior optical data. The results from the simulated CMM are

summarized and plotted in fig. 6.16. The horizontal line indicates the design parameter and the manufacturing tolerance ($\pm 0.05mm$ for all thicknesses) and the measurement results from different instruments are plotted as data points. Given that the CMM results indicate that the surfaces are nearly parallel to their opposite surfaces and the flatness value is very small, the flatness extracted from the simulated CMM are results from measurement uncertainties and artifacts. The flatness values from CMM and simulated CMM results on both datasets are plotted as error bars in fig. 6.16. Compared to CMM, the results extracted from the limited-angle CT shows large variations and anisotropy of uncertainty. The measurement at S_2 has the largest error and uncertainty, because the data acquired with the limited-angle trajectory is insufficient to uniquely calculate the S_2 surface. The CT measurement at S_3 also shows inconsistency to the CMM result. This is due to the cone-beam artifact, because the S_3 surface is nearly parallel and far from the trajectory plane. The results from the fusion of CT and optical data show high precision at all measurements, eliminating most of the volumetric artifacts causing the blurring of image boundaries. However, the fusion result at measuring S_1 under-performs the other two measurement instruments in terms of accuracy due to the limited accuracy of the optical scanner.

The measurement uncertainty in computed tomography is an open research topic. Image scaling, image artifacts, reconstruction algorithm, segmentation algorithm as well as evaluation strategy all affect the final measurements. The accuracy and the measurement uncertainty are not homogeneous in the reconstructed volume, which adds another layer of complexity to the problem. Müller *et. al.* [52] explore the different measurement strategies and Nardelli *et. al.* [53] attempts to assess the results employing features extracted

from the reconstructed volume. The uncertainty in this experiment can be calculated according the standard [1], similar to [36], as:

$$U = k_U \sqrt{u_{cal}^2 + u_p^2 + u_w^2 + u_b^2}, \tag{6.19}$$

where u_{cal} is the calibration uncertainty from the CMM.

$$u_p = \sqrt{\frac{1}{n-1} \sum_{i=1}^{n} (y_i - \bar{y})^2} \tag{6.20}$$

is the uncertainty from the repeated measurements, where $n = 6$ is the number of measurements and $\bar{y}$ is the average. The u_w is the uncertainty from the manufacturing and it is neglected in the following calculations. k_U is the coverage factor and is set to 2. The standard uncertainty of the systematic deviation between the CT measurement and the reference method u_b is calculated as:

$$u_b = \frac{1}{\sqrt{n}} \sqrt{\frac{1}{n-1} \sum_{i=1}^{n} (y_i - y_{cal})^2}, \tag{6.21}$$

where y_{cal} is the measurement using the reference method.

The uncertainty values have been calculated and listed in tab. 6.6 and tab. 6.7.

The uncertainty originating from the systematic deviation has dropped in the measurements on the data fusion result at S_2 and S_3, illustrated in fig. 6.15. This is achieved by mitigating the limited-angle artifact and cone-beam artifact respectively. At the same time, the increase in uncertainty at S_1 on the data fusion result compared to the CT result is due to the systematic deviation of

	u_p	u_b	u_{cal}	U
s1	0.007	0.099	0.004	0.198
s2	0.549	1.559	0.011	3.306
s3	0.039	0.561	0.016	1.126

Table 6.6: The uncertainty of the measurements on CT result. All results are measured in $[mm]$.

	u_p	u_b	u_{cal}	U
s1	0.002	0.169	0.004	0.337
s2	0.014	0.036	0.011	0.081
s3	0.001	0.058	0.016	0.121

Table 6.7: The uncertainty of the measurements on data fusion result. All results are measured in $[mm]$.

the optical scan.

6.7 Discussion

It has been shown that the data fusion can successfully mitigate the cone-beam artifact and the limited-angle artifact. The restored top and bottom surfaces segment the object from the supporting material, which greatly simplifies the post processing steps, although the cone-beam artifact is not completely removed. The major improvement comes from the fusion of features extracted by CT and the optical scan. The impact is clearly visible from the fusion result, as the external boundaries of the object are reconstructed. On the other hand, the proposed model and computation algorithm have several drawbacks. First, the model has multiple parameters, to which the minimizer is sensitive. Second, the optimization process needs to be accelerated to achieve a high-quality reconstruction within a short time.

The amount of available optical data has a substantial influence on the data fusion result. This impact comes from two aspects. More available optical data containing sufficient features on the surface of the object helps with the alignment of the optical and CT data. A complete optical scan also simplifies the data fusion as the optical scan can be treated as a segmentation separating the object from the volume. However, if both optical system and CT system are located in one coordinate system, *i.e.* no alignment is needed after the scans, the data fusion developed in this chapter can take advantage of any amount of optical data. Compared to the amount, the spatial distribution of the optical data has a larger impact on the final result. One observation from fig. 6.14 is that not all the cross-sections gain the same amount of improvement. If the optical data and CT data are redundant, the improvement is minimal as the CT data is sufficient in resolving the object. When the optical data complements the CT data, the optical data offers information that is missing from the CT data resulting in restored boundaries as shown in fig. 6.14(b,c). Since Tuy's conditions (eq. (3.12)) have described the subset of the image that can be reconstruction using only the CT data, if the optical data contains features that are missing in the subset, an improvement in the final result can be achieved by fusing optical data with CT data.

Although this chapter has only demonstrated the performance on mitigating cone-beam artifact and limited-angle artifact, the fusion of the optical data can be used to improve reconstruction with scattering artifact as well. More advanced alignment methods need to be implemented to enable alignment based on selected features rather than using the complete external surfaces from isosurface and optical scans.

Chapter 7

Conclusions and Outlook

The need for new reconstruction algorithms stems from the ever increasing demand from industry and research. As the variation of samples is vast and the information about any given sample is from different modalities, future reconstruction algorithm will become more flexible and will be able to integrate information known prior to the CT measurement. The contribution of this dissertation lies in the demonstration of utilizing a particular type of prior information, namely 3D optical scan, to improve the CT result and the discussion of the required changes in the entire work flow of a CT investigation. Fusing two datasets is advantageous as more information about one particular sample becomes available, but only with correct handling and careful interpretation can the result benefit from it.

7.1 Scientific contributions

7.1.1 Fulfillment of research objectives

The objective of this dissertation is to utilize the optical data as prior information and to develop a numerical framework to enable the data fusion of volumetric and surface 3D models in order to mitigate CT artifacts. Aiming at developing a flexible work flow to integrate optical data, the mesh representation acquired by the optical scanner is defined in a reference frame other than the reference frame of the CT reconstruction. Therefore, as the first step in the data fusion framework, the optical data is aligned with the CT data using the RanCEAF and the ICP algorithms. After converting the aligned optical mesh to a mask, the optical data is fused with the CT data using the models (eq. (6.7) and eq. (6.10)) developed in this dissertation. The stability of the models against noise is tested by simulated Poisson noise and validated by real-world experiment data. Finally, both cone-beam artifact and limited-angle artifact are greatly reduced. The features resolved by the optical scanner and CT are integrated into one 3D representation. The contrast to noise ratio at selected features gained an over 10 times improvement in a real-world experiment.

7.1.2 Closing the research gap

As a result of this dissertation, the research gap has been narrowed leading to a more reachable solution to routinely integrating prior optical data into a CT investigation.

Besides utilizing the optical data in the reconstruction, the optical data is also used to improve the scanning trajectory in a preliminary study. Instead of acquiring data along a conventional circular trajectory, a circle-line-circle

trajectory is applied to the acquisition, where the distance between the two circles in the CLC trajectory is set to be the distance between the top and bottom surfaces of the sample. The result from applying a CLC trajectory has shown a significant reduction of cone-beam artifact.

The work in this dissertation has enabled the fusion of optical data containing defects with CT data. The model developed in this work represents the reconstruction in a compressive sensing framework and adds the optical result as constraints to the objective function. The advantage of using partial optical data comes in two folds. First, artificially closing the holes on the mesh is no longer needed. The risk of losing features due to hole-closing algorithm is eliminated. Second, using partial optical data allows objects other than the sample of interest to exist in the field of view.

7.2 Outlook

With little modification of the CT hardware, significant improvement in reconstruction has been accomplished in this dissertation. It has been demonstrated that the integration of optical data can mitigate artifacts in the reconstruction. This project has laid foundation for many interesting research topics and further engineering challenges.

In this dissertation, the acquisition, reconstruction and the analysis, as illustrated in fig. 4.1, are three discrete procedures. Improvements can be achieved in each procedure when employing prior information. If the manipulation system allows more degrees of freedom, the design of the scanning trajectory can be more flexible and better utilize the prior information. As the accuracy of the manipulation system may suffer when performing sophisticated

trajectories, the approach in this dissertation to calibrate the geometry can be applied to alleviate the problem. The reconstruction procedure can be improved in at least two ways. On one hand, the alignment and the reconstruction can be performed iteratively allowing the alignment to readjust. On the other, the conversion between mesh and volume representation can be avoided by intersecting the mesh with the reconstruction volume. As for the analysis procedure, the prior information can help in rejecting measurements corrupted by artifacts.

Although it is a repetition of the idea from Gang *et. al.* [32], a CT investigation should be considered as an end-to-end work flow. As after each projection taken, one more piece of information of the sample is obtained, the next projection should be selected based on the measurement task. So far, the implementation of Gang *et. al.* still limits the number of degrees of freedoms of the manipulation system due to the characteristic of medical C-arm systems. With less constraints, the parameter space of an industrial CT is much larger. A potential contribution would be the integration of the optical data to add constraints to the search of the next projection. At the same time, the amount of computation needed for such problems is large. As the resolution of the detector increases in industrial CT setups and a broader search space, the computation problem itself becomes a research topic. The development of X-ray source and detector technology, better physical modeling and faster computation will continue to be active research areas.

Bibliography

[1] ISO 15530-3 Geometrical product specifications - Coordinate measuring machines: Technique for determining the uncertainty of measurement. Technical report, 2011.

[2] Y. I Abdel-Aziz, H. M. Karara, and Michael Hauck. Direct Linear Transformation from Comparator Coordinates into Object Space Coordinates in Close-Range Photogrammetry*. *Photogrammetric Engineering & Remote Sensing*, 81(2):103–107, February 2015.

[3] A H Andersen and A C Kak. Simultaneous algebraic reconstruction technique (SART): a superior implementation of the art algorithm. *Ultrasonic imaging*, 6(1):81–94, January 1984.

[4] Utkarsh Ayachit. *The ParaView Guide: A Parallel Visualization Application*. Kitware, Inc., USA, 2015.

[5] Hussein BANJAK, Marius COSTIN, Caroline VIENNE, and Valerie KAFTANDJIAN. X-ray Computed Tomography Reconstruction on NonStandard Trajectories for Robotized Inspection. In *19th World Conference on Non-Destructive Testing 2016*, Munich, July 2016.

[6] K. Joost Batenburg, Willem Jan Palenstijn, Peter Balazs, and Jan Sijbers. Dynamic angle selection in binary tomography. *Computer Vision and Image Understanding*, 117(4):306–318, April 2013.

[7] Andrea Bayer. *Data Fusion of Surface Meshes and Volumetric Representations*. PhD thesis, Heidelberg university, Heidelberg, July 2016.

[8] P. J. Besl and N. D. McKay. A method for registration of 3-D shapes. *IEEE Transactions on Pattern Analysis and Machine Intelligence*, 14(2):239–256, February 1992.

[9] Andreas Beyer, Yu Liu, Hubert Mara, and Susanne Kroemker. Mesh Reduction to Exterior Surface Parts via Random Convex-Edge Affine Features. In Ilias S. Kotsireas, Siegfried M. Rump, and Chee K. Yap, editors, *Mathematical Aspects of Computer and Information Sciences*, number 9582 in Lecture Notes in Computer Science, pages 63–77. Springer International Publishing, November 2015. DOI: 10.1007/978-3-319-32859-1_5.

[10] Gianfranco Bianco, Alessandro Gallo, Fabio Bruno, and Maurizio Muzzupappa. A Comparative Analysis between Active and Passive Techniques for Underwater 3d Reconstruction of Close-Range Objects. *Sensors*, 13(8):11007–11031, August 2013.

[11] Glenn D Boreman. *Modulation transfer function in optical and electro-optical systems*, volume 21. SPIE press Bellingham, WA, 2001.

[12] E Borg and HG Grondahl. On the dynamic range of different X-ray photon detectors in intra-oral radiography. A comparison of image quality in film, charge-coupled device and storage phosphor systems. *Dentomaxillofacial Radiology*, 25(2):82–88, 1996.

[13] Jean-yves Bouguet. Camera Calibration Toolbox. Technical report, 2008.

[14] A. Buades, B. Coll, and J. Morel. A Review of Image Denoising Algorithms, with a New One. *Multiscale Modeling & Simulation*, 4(2):490–530, January 2005.

[15] A. Buades, B. Coll, and J.-M. Morel. A non-local algorithm for image denoising. In *IEEE Computer Society Conference on Computer Vision and Pattern Recognition, 2005. CVPR 2005*, volume 2, pages 60–65 vol. 2, June 2005.

[16] Thorsten M. Buzug. *Computed tomography from photon statistics to modern cone-beam CT*. Springer, Berlin, 2008.

[17] Y. Censor. Finite series-expansion reconstruction methods. *Proceedings of the IEEE*, 71(3):409–419, March 1983.

[18] Guillermo Avendano Cervantes. *Technical Fundamentals of Radiology and CT*. IOP Publishing, 2016. DOI: 10.1088/978-0-7503-1212-7.

[19] Volkan Cevher. Learning with Compressible Priors. In Y. Bengio, D. Schuurmans, J. D. Lafferty, C. K. I. Williams, and A. Culotta, editors,

Advances in Neural Information Processing Systems 22, pages 261–269. Curran Associates, Inc., 2009.

[20] Guang-Hong Chen, Jie Tang, and Shuai Leng. Prior image constrained compressed sensing (PICCS): A method to accurately reconstruct dynamic CT images from highly undersampled projection data sets. *Medical physics*, 35(2):660–663, February 2008.

[21] Zhiqiang Chen, Xin Jin, Liang Li, and Ge Wang. A limited-angle CT reconstruction method based on anisotropic TV minimization. *Physics in Medicine and Biology*, 58(7):2119–2141, April 2013.

[22] D. Chetverikov, D. Svirko, D. Stepanov, and P. Krsek. The Trimmed Iterative Closest Point algorithm. In *Object recognition supported by user interaction for service robots*, volume 3, pages 545–548 vol.3, 2002.

[23] Seungryong Cho, Dan Xia, Charles A. Pellizzari, and Xiaochuan Pan. A BPF-FBP tandem algorithm for image reconstruction in reverse helical cone-beam CT. *Medical Physics*, 37(1):32–39, January 2010.

[24] Paolo Cignoni, Marco Callieri, Massimiliano Corsini, Matteo Dellepiane, Fabio Ganovelli, and Guido Ranzuglia. MeshLab: an Open-Source Mesh Processing Tool. In Vittorio Scarano, Rosario De Chiara, and Ugo Erra, editors, *Eurographics Italian Chapter Conference*. The Eurographics Association, 2008.

[25] Andrei Dabravolski, Kees Joost Batenburg, and Jan Sijbers. Adaptive zooming in X-ray computed tomography. *Journal of X-Ray Science and Technology*, 22(1):77–89, January 2014.

[26] James Davis, Stephen R Marschner, Matt Garr, and Marc Levoy. Filling holes in complex surfaces using volumetric diffusion. In *3D Data Processing Visualization and Transmission, 2002. Proceedings. First International Symposium on*, pages 428–441. IEEE, 2002.

[27] Michel Defrise, Frederic Noo, Rolf Clackdoyle, and Hiroyuki Kudo. Truncated Hilbert transform and image reconstruction from limited tomographic data. *Inverse Problems*, 22(3):1037, 2006.

[28] Arnold Dresden. The fourteenth western meeting of the American Mathematical Society. *Bulletin of the American Mathematical Society*, 26(9):385–396, 1920.

[29] Eypor Runar Eiriksson, Jakob Wilm, David Bue Pedersen, and H. Aanas, Henrik. PRECISION AND ACCURACY PARAMETERS IN STRUCTURED LIGHT 3-D SCANNING. In *ISPRS - International Archives of the Photogrammetry, Remote Sensing and Spatial Information Sciences*, volume XL-5-W8, pages 7–15. Copernicus GmbH, April 2016.

[30] L. A. Feldkamp, L. C. Davis, and J. W. Kress. Practical cone-beam algorithm. *Journal of the Optical Society of America A*, 1(6):612–619, June 1984.

[31] Juergen Frikel. Sparse regularization in limited angle tomography. *Applied and Computational Harmonic Analysis*, 34(1):117–141, January 2013.

[32] Grace J. Gang, Junghoon Lee, J. Webster Stayman, Daniel J. Tward, W. Zbijewski, Jerry L. Prince, and Jeffrey H. Siewerdsen. Analysis of Fourier-domain task-based detectability index in tomosynthesis and cone-beam CT in relation to human observer performance. *Medical Physics*, 38(4):1754–1768, April 2011.

[33] S.J. Glick, M.A. King, K. Knesaurek, and K. Burbank. An investigation of the stationarity of the 3d modulation transfer function of SPECT. *IEEE Transactions on Nuclear Science*, 36(1):973–977, February 1989.

[34] P. Grangeat. Analysis of a 3d imaging device by reconstruction from cone beam X ray radiographs. Technical report, France, 1987. FRCEA-TH–42.

[35] A. Gruen and Thomas S. Huang, editors. *Calibration and Orientation of Cameras in Computer Vision*. Springer-Verlag New York, Inc., Secaucus, NJ, USA, 2001.

[36] Jochen Hiller and Peter Hornberger. Measurement accuracy in X-ray computed tomography metrology: Toward a systematic analysis of interference effects in tomographic imaging. *Precision Engineering*, 45(Supplement C):18–32, July 2016.

[37] Stefan Hoppe, F. Dennerlein, GUnter Lauritsch, J. Hornegger, and F. Noo. Cone-beam Tomography from Short-Scan Circle-plus-Arc Data Measured on a C-arm System. In *IEEE Nuclear Science Symposium Conference Record, 2006*, volume 5, pages 2873–2877, October 2006.

[38] Z. Huang, M. Borland, P. Emma, J. Wu, C. Limborg, G. Stupakov, and J. Welch. Suppression of microbunching instability in the linac coherent

light source. *Physical Review Special Topics - Accelerators and Beams*, 7(7):074401, July 2004.

[39] Xun Jia, Bin Dong, Yifei Lou, and Steve B. Jiang. GPU-based iterative cone-beam CT reconstruction using tight frame regularization. *Physics in Medicine and Biology*, 56(13):3787–3807, July 2011.

[40] Ming Jiang and Ge Wang. Convergence of the simultaneous algebraic reconstruction technique (SART). *IEEE Transactions on Image Processing*, 12(8):957–961, August 2003.

[41] S. Kaczmarz. Angenherte auflsung von systemen linearer gleschungen. B Int Acad Pol Sci Lettres Classe des Sciences Mathematiques et Naturels. Serie A. Sciences Mathematiques, Cracovie. *Imprimerie de l Universite*, pages 355–357, 1937.

[42] Avinash C Kak and Malcolm Slaney. *Principles of computerized tomographic imaging*. SIAM, 2001.

[43] Hiroyuki Kudo, Matias Courdurier, Frederic Noo, and Michel Defrise. Tiny a priori knowledge solves the interior problem in computed tomography. *Physics in Medicine and Biology*, 53(9):2207–2231, May 2008.

[44] Ming Li, Cheng Zhang, Chengtao Peng, Yihui Guan, Pin Xu, Mingshan Sun, and Jian Zheng. Smoothed Norm Regularization for Sparse-View X-Ray CT Reconstruction. *BioMed Research International*, 2016:e2180457, September 2016.

[45] William E. Lorensen and Harvey E. Cline. Marching Cubes: A High Resolution 3d Surface Construction Algorithm. In *Proceedings of the 14th Annual Conference on Computer Graphics and Interactive Techniques*, SIGGRAPH '87, pages 163–169, New York, NY, USA, 1987. ACM.

[46] Armando Manduca, Joshua D. Trzasko, and Zhoubo Li. Compressive sensing of images with a priori known spatial support. 2010.

[47] MATLAB. *version 9.20.0 (R2017a)*. The MathWorks Inc., Natick, Massachusetts, 2017.

[48] C. E. Metz and K. Doi. Transfer function analysis of radiographic imaging systems. *Physics in Medicine and Biology*, 24(6):1079, 1979.

[49] Shinichiro Mori, Masahiro Endo, Kanae Nishizawa, Mari Ohno, Hiroaki Miyazaki, Kazuhiko Tsujita, and Yasuo Saito. Prototype heel effect compensation filter for cone-beam CT. *Physics in Medicine and Biology*, 50(22):N359, 2005.

[50] Cyril Mory, Bo Zhang, Vincent Auvray, Michael Grass, D. Schafer, Francoise Peyrin, Simon Rit, Philippe Douek, and Loic Boussel. ECG-gated C-arm computed tomography using L1 regularization. In *Signal Processing Conference (EUSIPCO), 2012 Proceedings of the 20th European*, pages 2728–2732. IEEE, 2012.

[51] J. Muders and J. Hesser. Stable and Robust Geometric Self-Calibration for Cone-Beam CT Using Mutual Information. *IEEE Transactions on Nuclear Science*, 61(1):202–217, February 2014.

[52] P. Müller, J. Hiller, A. Cantatore, and L. De Chiffre. A study on evaluation strategies in dimensional X-ray computed tomography by estimation of measurement uncertainties. *International Journal of Metrology and Quality Engineering*, 3(2):107–115.

[53] Vitor C. Nardelli, Francisco A. Arenhart, Gustavo D. Donatelli, Mauricio C. Porath, Christian Niggemann, and Robert Schmitt. Feature-based analysis for quality assessment of x-ray computed tomography measurements. *Measurement Science and Technology*, 23(10):105006, 2012.

[54] M. Oehler and T. M. Buzug. Statistical Image Reconstruction for Inconsistent CT Projection Data. *Methods of Information in Medicine*, 46(3):261–269, 2007.

[55] Xiaochuan Pan, Emil Y Sidky, and Michael Vannier. Why do commercial CT scanners still employ traditional, filtered back-projection for image reconstruction? *Inverse problems*, 25(12):1230009, January 2009.

[56] Xiaochuan Pan, Yu Zou, and M. A. Anastasio. Data redundancy and reduced-scan reconstruction in reflectivity tomography. *IEEE Transactions on Image Processing*, 12(7):784–795, July 2003.

[57] Dennis L. Parker. Optimal short scan convolution reconstruction for fan beam CT. *Medical Physics*, 9(2):254–257, March 1982.

[58] John C Platt and Alan H Barr. Constraints methods for flexible models. *ACM SIGGRAPH Computer Graphics*, 22(4):279–288, 1988.

[59] S. Rit, M. Vila Oliva, S. Brousmiche, R. Labarbe, D. Sarrut, and G. C. Sharp. The Reconstruction Toolkit (RTK), an open-source cone-beam CT reconstruction toolkit based on the Insight Toolkit (ITK). *Journal of Physics: Conference Series*, 489(1):012079, 2014.

[60] Mohamed Rizon, Yazid Haniza, Saad Puteh, Ali Yeon, Md Shakaff, Saad Abdul Rahman, Masanori Sugisaka, Yaacob Sazali, Mamat M Rozailan, and M Karthigayan. Object detection using circular Hough transform. 2005.

[61] Christian Schorr and Michael Maisl. Exploitation of geometric a priori knowledge for limited data reconstruction in nondestructive testing. In *Fully Three-Dimensional Image Reconstruction in Radiology and Nuclear Medicine. Proceedings*, pages 114–117, 2013.

[62] Michael SCHRAPP, Andreas FISCHER, and Karsten SCHOERNER. CT Reconstruction with Object Specific Non-Standard Trajectories. In *Digital Industrial Radiology and Computed Tomography (DIR 2015)*, June 2015.

[63] Y Shim and Z Cho. SVD pseudoinversion image reconstruction. *IEEE Transactions on Acoustics, Speech, and Signal Processing*, 29(4):904–909, 1981.

[64] Emil Y. Sidky, Chien-Min Kao, and Xiaochuan Pan. Accurate image reconstruction from few-views and limited-angle data in divergent-beam CT. *Journal of X-Ray Science and Technology*, 14(2):119–139, January 2006.

[65] Donald L. Snyder, Richard L. White, and Abed M. Hammoud. Image recovery from data acquired with a charge-coupled-device camera. *JOSA A*, 10(5):1014–1023, May 1993.

[66] Marco Stampanoni, Gunther Borchert, Peter Wyss, Rafael Abela, Bruce Patterson, Steven Hunt, Detlef Vermeulen, and Peter Rüegsegger. High resolution X-ray detector for synchrotron-based microtomography. *Nuclear Instruments and Methods in Physics Research Section A: Accelerators, Spectrometers, Detectors and Associated Equipment*, 491(1):291–301, September 2002.

[67] Richard Szeliski. *Computer vision: algorithms and applications*. Springer Science & Business Media, 2010.

[68] Heang Tuy. Reconstruction of a three-dimensional object from a limited range of views. *Journal of Mathematical Analysis and Applications*, 80(2):598–616, April 1981.

[69] Daniel J. Tward and Jeffrey H. Siewerdsen. Cascaded systems analysis of the 3d noise transfer characteristics of flat-panel cone-beam CT. *Medical Physics*, 35(12):5510–5529, December 2008.

[70] Zhou Wang, A.C. Bovik, H.R. Sheikh, and E.P. Simoncelli. Image quality assessment: from error visibility to structural similarity. *IEEE Transactions on Image Processing*, 13(4):600–612, April 2004.

[71] Zhye Yin, Bruno De Man, Jed Pack, Zhye Yin, Bruno De Man, and Jed Pack. 3d Analytic Cone-Beam Reconstruction for Multiaxial CT Acquisitions, 3d Analytic Cone-Beam Reconstruction for Multiaxial CT Acquisitions. *International Journal of Biomedical Imaging, International Journal of Biomedical Imaging*, 2009, 2009:e538389, August 2009.

[72] G. L. Zeng and G. T. Gullberg. A study of reconstruction artifacts in cone beam tomography using filtered backprojection and iterative EM algorithms. *IEEE Transactions on Nuclear Science*, 37(2):759–767, April 1990.

[73] G. L. Zeng, G. T. Gullberg, P. E. Christian, and D. Gagnon. Cone-beam iterative reconstruction of a segment of a long object. *IEEE Transactions on Nuclear Science*, 49(1):37–41, February 2002.

[74] Qilong Zhang and R. Pless. Extrinsic calibration of a camera and laser range finder (improves camera calibration). In *2004 IEEE/RSJ International Conference on Intelligent Robots and Systems (IROS) (IEEE Cat. No.04CH37566)*, volume 3, pages 2301–2306 vol.3, September 2004.

[75] Yu Zou and Xiaochuan Pan. Exact image reconstruction on PI-lines from minimum data in helical cone-beam CT. *Physics in Medicine and Biology*, 49(6):941, 2004.

Publications

- Yu Liu, Philipp Schuetz, Alexander Flisch, Urs Sennhauser (2014), Exploring the limits of limited-angle computed tomography complemented with surface data, *11th European Conference on Non-Destructive Testing*, Prague, Czech Republic
- Andreas Beyer, Yu Liu, Hubert Mara, Susanne Kromker (2016), Mesh Reduction to Exterior Surface Parts via Random Convex-Edge Affine Features, in Proceeding of *Sixth International Conference on Mathematical Aspects of Computer and Information Sciences*
- Yu Liu, Andreas Beyer, Juergen Hoffmann, Alexander Flisch, Urs Sennhauser (2016), Reducing volumetric artifact in computed tomography by cooperative data fusion, *the International Conference on Processes in Combined Digital Optical and Imaging Methods applied to Mechanical Engineering*, Ascona, Switzerland
- Yu Liu, Andreas Beyer, Philipp Schuetz, Juergen Hofmann, Alexander Flisch, Urs Sennhauser (2016), Cooperative data fusion of transmission and surface scan for improving limited-angle computed tomography reconstruction, in *NDT&E international*, 83, 24-31
- Andreas Beyer, Yu Liu, Susanne Kromker (2016), OctaCoG Alignment: A Fast and Reliable Alternative to Iterative Alignment Schemes, in Proceeding of *FUSION 2016*